MODELING AND SIMULATION OF THE DYNAMIC PROCESS IN HIGH ENERGY BALL MILLING OF METAL POWDERS

A thesis submitted in fulfillment of the
requirements for the degree of

Doctor of Philosophy

in Materials and Process Engineering
by

WEI WANG

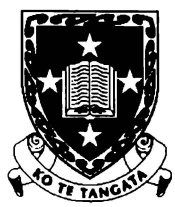

The
University
of Waikato
Te Whare Wānanga
o Waikato

April 2000

To

my fiancé, Xuezhen, my aunts and uncles

for their love and support

and to

my cousin Meny's wedding (April 2, 2000)

Abstract

Mechanical alloying/mechanical grounding by using high-energy ball milling has been considered as a promising materials processing technique to synthesize materials. In this study, modeling simulation has been carried out to investigate the impacts, which are basic events in milling, as well as the milling dynamics in order to control and optimize this process.

A 3-dimensional model has been developed to simulate the head-on impact process between two balls or between a ball and the vial wall with powder in between by considering the elastic deformation of impact objects, and the visco-plastic flow and elastic deformation of the powder compact. The comparison between the experimental results published in literature and the simulation outcome demonstrates that this model is the best to simulate the head-on impact process, which involves powder. Application of the model in high-energy ball milling shows that the ball-ball and ball-wall impacts do have some difference. It was also observed that the ball size, impact velocity and powder thickness all affect the impact pressure, and that the deformation of balls is substantial comparing to the powder thickness involved in an impact.

3-dimensional models have also been developed to simulate the movement of balls considering the effects of powder, ball spinning and oblique impact of balls. The multi-ball impacts, which have been proved to occupy a substantial fraction among impacts, were also considered. Having realised the importance of knowing the volume of the powder involved in each impact, a model was also developed to estimate this volume. The prediction of the weight of powder involved in each impact made based on this model was in good agreement with the observation reported.

A 3-dimensional global model has been developed for the SPEX-8000 Mixer/Mill based on the mechanics of the machine. By using this model, the motion of the vial

was numerically determined. Then the global model was coupled with the models for the impacts in order to predict the dynamics of milling process. The simulation results revealed that the movement of balls after milling starts can be separated into two stages. The first stage is the unstable stage, which lasts for less than 0.3 second and involves mostly rolling and slipping of balls on the vial wall. The second stage is the stable stage, when the impact frequency, the mean impact velocity and mean spinning velocity of balls do not change significantly over time. Numerical experiments indicate that the frequency of impacts between balls and the vial wall is linearly proportional to the number of balls and the frequency of impacts between balls is nearly proportional to the square of the number of balls and the square of radius of balls. It is also shown that the majority of the impacts occur at low velocities of less than 4 m/s and with impact angles in the range of 15~75°. The prediction of the impact frequency and impact angle distribution made from the simulation agrees well with the probability analysis.

An effective model has been developed for the first time to calculate the time needed for mechanical milling based on probability analysis. This model can be used once the effective impact frequency and the fraction of powder effectively mechanically milled powder are known. The latter can be achieved through modeling. The milling efficiency corresponding to various ball numbers and sizes have been evaluated. The results show that there is an optimum number for the best milling efficiency for a given size of balls.

Global models for the milling process in a planetary mill and an attritor mill have also been developed. Preliminary simulation experiments have been conducted.

Acknowledgments

Special thanks to my supervisors, Dr. Deliang Zhang and Assoc. Prof. Alan Langdon, for their support and guidance, and to Assoc. Prof. Wei Gao and Dr. Zhenyu Liu from the Department of Chemical and Materials Engineering, the University of Auckland, for their recommendation and help.

Thanks to my best friend Dr Xiaoguang Sun for his support and to my former supervisors Prof. Guodong Wang, Prof. Xianghua Liu and Prof. Qiang Zhang, from Northeastern University, China, for their guidance in mechanical modeling.

Thanks to Alf Harris and Dave Wild for their assistance in operation of the SEM, Basil Fenton For his guidance in operation of SEM, Yuanji Zhang for his help in XRD Robert Torrens and Dr. Geoffrey Tompsett for proofreading of my manuscript, all the Department of Materials and Process Engineering staff, my colleagues: Georgees Adam, Jennifer Richmond, Paul Dixon, Pieter Smilde, Mike Brown, Matthew Henderson, Yanhai Du, Justin Hyde, Conrad Lendrum, Zailu Yang, John Davidson, Zhihong Cai and everyone else I have neglected to mention above.

Table of Contents

Abstract *iii*

Acknowledgments *v*

Table of Contents *vi*

List of Figures *xi*

List of Tables *xviii*

List of Symbols *xix*

Chapter One Introduction: **1**

Reference 5

Chapter Two Literature Review **6**

2.1 Introduction 6

2.2 History of Mechanical Alloying 6

2.3 Equipment Used to Achieve Mechanical Alloying 10

2.3.1 Conventional Horizontal Ball Mill 10

2.3.2 Attritor Mill 12

2.3.3 Vibratory Mill 13

2.3.4 Planetary Ball Mill 14

2.4 Materials Produced by Mechanical Alloying 15

2.4.1 ODS Alloys 15

2.4.2 Amorphous Materials 16

2.4.3 Extended Solid Solutions 16

2.4.4 Intermetallics 17

2.4.5 Nanostructured Materials 18
2.4.6 Composite Materials 19
2.4.7 Quasicrystals 19
2.5 Understandings of Mechanical Alloying Process 19
2.5.1 Particle Morphology and Microstructural Evolution 20
2.5.1.1 Ductile/Ductile Systems 21
2.5.1.2 Ductile/Brittle Systems 24
2.5.1.3 Brittle/Brittle Systems 25
2.5.2 Influencing Factors 25
2.5.2.1 Factors Influencing Powder Contamination 25
2.5.2.2 Milling Intensity 26
2.5.3 Mechanism of Phase Formation during MA 27
2.6 Modeling/Simulation of the Dynamics of Milling Media 30
2.6.1 Overview 30
2.6.2 Deformation during Impact 33
2.6.3 Cold Welding and Fracturing 39
2.6.4 Volume of Material per Collision 40
2.6.5 Temperature Increase 42
2.6.6 Milling Time 42
2.6.7 Global Modeling of Vibratory Mills 43
2.6.8 Global Modeling of Attritor mills 46
2.6.9 Global Modeling of Planetary Mills and Horizontal Mills 49
2.7 Summary and Objectives 50
2.8 References 50

Chapter Three Model for Single Head-on Impact 64
3.1 Introduction 64
3.2 Description of an Impact Process 64
3.3 Assumptions 65
3.4 The Deformation of Tools 66

3.5 Powder Flow 67
3.6 Impact Force and Pressure 76
3.7 Elastic Strain ε_z^e 78
3.8 Impact Dynamics 80
3.9 Determination of the Flow shear Stress in Powder Compact, τ_s 82
3.10 Determination of the Elastic Coefficient, k_e 85
3.11 Applying the Model 85
3.12 Validation 87
3.13 Application of the Head-on Impact Model to High-Energy Ball Milling 91
3.14 Summary 97
3.15 References 97

Chapter Four Models for Other Forms of Impact and Powder Volume Trapped at Collision Point 98

4.1 Introduction 98
4.2 Model for Oblique Impact 99
4.3 Model for Multi-Ball Impact 103
4.4 Volume of Powder Trapped at Collision Point 104
4.5 Reference 110

Chapter Five Global Model of SPEX 8000-Mixer/Mill 111

5.1 Introduction 111
5.2 The Model for the Motion of Vial 111
5.3 Dynamics of Balls Inside the Vial 115
5.3.1 The Initial Positions and Velocities of Balls 115
5.3.2 Free Movement of Balls 116
5.3.3 Impact between Balls 117
5.3.4 Impact between a Ball and the Cylindrical Wall 118

5.3.5 Impact between a Ball and the Ends of the Vial 119
5.4 Methodology of Computation 120

Chapter Six Results and Discussion on Modeling of SPEX 8000 Mixer/Mill 122
6.1 Introduction 122
6.2 Motion of the Vial 123
6.3 One Ball in the Vial 127
6.4 Multi Balls in the Vial 134
6.4.1 The Motion of Balls 134
6.4.2 Distribution of Impact Angles 138
6.4.3 Frequency of Impacts 140
6.4.4 The Distribution of Impact Velocity 143
6.4.5 Milling Time 148
6.5 Discussion 150
6.6 Summary 152
6.7 References 152

Chapter Seven Global Models for Planetary and Attritor Mills 154
7.1 Introduction 154
7.2 Planetary Mills 154
7.2.1 The Model for the Motion of Vial 154
7.2.2 Dynamics of Balls Inside the Vial 158
7.2.2.1 Impacts between Balls 158
7.2.2.2 Impacts between Balls and Wall 158
7.2.2.3 Free Movement of Balls 160
7.2.2.4 The Initial Positions and Velocities of Balls 160
7.3 Attritor Mills 161
7.3.1 The Model for the Motion of the Impellers of the Container 162
7.3.1.1 Impacts between Balls 163

7.3.1.3 Free Movement of Balls 168
7.3.1.4 The Initial Positions and Velocities of Balls 168
7.4 Methodology of Computation 168
7.5 Preliminary Results on Modeling of Planetary Mill 168
7.5.1 One Ball in the Vial 168
7.5.2 Five Balls in the Vial 170
7.6 Preliminary Results on Modeling of Attritor Mill 171
7.7 Summary 171

Chapter Eight Conclusions and Recommendations 172
8.1 Conclusions 172
8.2 Recommendations for Future Work 174

Appendix I Equation (3-21) 175
Appendix II Equation (4-16) 177
Reference 177
Appendix III Geometrical Analysis on Impact Angle Probability 178
Appendix IV Experimental Results of the Impact Number and Velocity Distribution 180
8 gram balls 180
7 gram balls 182
6 gram balls 184
5 gram balls 186
4 gram balls 188
3 gram balls 190
2 gram balls 192
Appendix V The Model for Milling Time 194

List of Figures

Figure 1-1. Schematic diagram showing the logical development of this work 3

Figure 2-1. Chronological evolution of MA process modified from Murty and Ranganatha's review 8

Figure 2-2. Number of publications per year before 1993 9

Figure 2-3. Conventional horizontal ball mill 11

Figure 2-4. Uniball mill 11

Figure 2-5. Vertical and horizontal attritors 12

Figure 2-6. SPEX-8000 Mixer/Mill 13

Figure 2-7. The schematic diagram of the shake ball mill 14

Figure 2-8. Planetary ball mill 14

Figure 2-9. The five stages of MA as described by Benjamin and Volin 21

Figure 2-10. Schematic diagram of the microstructural evolution that occurs during MA of ductile/brittle systems 24

Figure 2-11. Particle with an A/B boundary (nearly horizontal). Dislocation in A and B (nearly vertical lines) intersect the A/B boundary. Figure (a), (b) and (c) denote successive times in the MA process. For clarity, the shape of the particle has been assumed constant. 29

Figure 2-12. Schematic of the distribution of stress over the contact area during a collision between composite balls as described by Maurice and Courtney (a) Early in the collision, the balls deform elastically. (b) The powder begins to deform plastically when the stress attains the powder hardness. (c) During this stage, the center of the contact area is characterized by plastic deformation of both powder and ball, and outside

this annulus there is no deformation of either (not to scale). 34

Figure 2-13. Kelvin model 35

Figure 2-14. Dallimore & McCormick's modified Kelvin model 36

Figure 2-15. Comparison of different models and measured data 37

Figure 2-16. Rheological models 38

Figure 2-17. Inoue and Okaya's model 39

Figure 2-18. Fracture mode used by Maurice and Courtney 39

Figure 2-19. The modified 'swept' model 41

Figure 2-20. The volume of powder participated in the impact 42

Figure 2-21. Energy Loss Distribution 43

Figure 2-22. Frequency distribution of Impact Angles in a SPEX mill. The triangles represent simulation from Davis et al's work. Results are for (a) a distribution of random, (b) a distribution of biased toward glancing angles and (c) an expected distribution with small number of balls. 44

Figure 2-23. Fluid model to determine the media velocity in an attritor 46

Figure 2-24. Rotational velocities (a) at the mill top for operating at 50 rpm and (b) at the mill bottom for operating at 250 rpm. 48

Figure 2-25. Vertical velocity gradients along the mill side for operating at (a) 50 rpm and (b) at 250 rpm 48

Figure 3-1. Schematic diagram showing an impact process of balls on a mini powder compact 65

Figure 3-2. Deformation during impact of tools 65

Figure 3-3. Powder Restitution. 65

Figure 3-4. The concentrated force acted on a flat surface 66

Figure 3-5. Schematic diagram of the contacting area 66

Figure 3-6. Cylindrical co-ordinate system to express powder flow when two balls of same size impact with a powder compact in between 68

Figure 3-7. The process to get the equivalent radius R_e 75

Figure 3-8. Two components of impact pressure 76

Figure 3-9. Powder flow caused by deformation 79

Figure 3-10. A compression experiment, where powder is free to flow to its around 82

Figure 3-11. Schematic geometry of the powder compact and τ_z distribution along thickness direction 83

Figure 3-12. One cycle compression experiment 85

Figure 3-13. The computational logic for head-on impact model 86

Figure 3-14. The method to determine c_1 and k' 87

Figure 3-15. Impact forces as a function of time during impact under different conditions. V is relative velocity of tools, R is the radius of ball and H is the initial thickness of powder compact. a~d: different ball diameters, a, e and f: different powder thickness, and a, g and h: different impact velocities 89

Figure 3-16. Impact force, maximum pressure and ball velocity as functions of time during a typical ball-wall impact. Ball initial velocity: 10 m/s; radius of ball: 6.25 mm; ball material: stainless steel; and initial thickness of powder compact: 0.5mm 92

Figure 3-17. Impact force, maximum pressure and ball velocity as functions of time during a typical ball-ball impact. Ball initial velocity: 10 m/s; radius of ball: 6.25 mm; ball material: stainless steel; and initial thickness of powder compact: 0.5mm 93

Figure 3-18. Maximum Pressure as functions of impact velocity, ball diameter, ball density and powder thickness respectively 95

Figure 3-19. Ball deformation and its function of the impact velocities 96

Figure 4-1. Schematic diagrams showing different forms of impacts 99

Figure 4-2. Coordinate system for impacting balls 99

Figure 4-3. Schematic diagrams showing different modes of sliding of balls 101

Figure 4-4. When powder is poured onto the surface of a plate, it forms a pile of a cone. The angle between the cone surface and the surface of the plate, θ_p, can be measured by an experiment for different powders. 105

Figure 4-5. A ball surface can be viewed as a complex body, which is combined by many small tilted "flat surfaces" 105

Figure 4-6. The shape of powder pile coated on the surface of a ball is assumed to be a cone 106

Figure 4-7. The shape of powder pile coated on the surface of a ball is assumed to be a cone 107

Figure 4-8. Powder thickness coated on the impacting ball as a function of ball size 108

Figure 4-9. Coating weight involved in an impact as functions of the radius of ball 109

Figure 5-1. Schematic working diagram of a SPEX-8000 Mixer/Mill 112

Figure 5-2. Diagram of the abstract model for a SPEX-8000 Mixer/Mill 112

Figure 5-3. Free body diagram of shaft-arm motion balanced by Spring 4 113

Figure 5-4. Free body diagram of the fulcrum's motion balanced by Springs 1, 2 and 3 114

Figure 5-5. Ball original positions 116

Figure 6-1. ϕ and Y_m as functions of time 124

Figure 6-2. The predicted positions of the end of the shaft arm as functions of time 124

Figure 6-3. The predicted vial motion in X, Y, Z directions as functions of time for the right end of the vial 125

Figure 6-4. The effect of 'loosened' spring 4, whose elastic coefficient is 150 kN/m comparing with a regular spring 4, whose elastic coefficient is 260 kN/m 126

Figure 6-5. Examples of simulated result showing the ball position inside the vial at different times for a mill with one ball 127

Figure 6-6. The trajectory of the ball in 1 second for SPEX 8000 Mixer/Mill with one ball in the vial, projected to (a) plane $x'o'y'$, (b) plane $x'o'y'$ and (c) plane $y'o'z'$ 128

Figure 6-7. (a) Ball position in r direction in the vial as a function of time, (b) the trajectory of the ball projected to plane $y'o'z'$ as a function of time during 0~0.2 second and (c) the trajectory of the ball projected to plane $y'o'z'$ as a function of time during 0.8~1 second 130

Figure 6-8. The spinning speed of the ball as a function of time 131

Figure 6-9. Velocity of the ball in reference with to the vial in different directions as functions of time 132

Figure 6-10. The impact velocity of each of the impacts occurred during 1 second 133

Figure 6-11. Example images showing the positions of the vial and balls at different times after milling starts for five ball mill. 134

Figure 6-12. Typical position of a selected ball in r direction as a function of time for the condition of using 5, 10 and 14 balls respectively 136

Figure 6-13. The impact velocity of each of the impacts, which occur during milling using 2, 5 and 10 balls respectively 137

Figure 6-14. Definition of impact angle 138

Figure 6-15. The fraction of the impact frequency as a function of impact angle for different number of balls with 3.94 mm in radius 139

Figure 6-16. The fraction of the impact frequency as a function of impact angle for different number of balls with 4.96 mm in radius 139

Figure 6-17. The frequency of impacts of ball-wall as functions of ball number for different size of balls 140

Figure 6-18. The frequency of impacts of ball-ball as functions of ball number for different size of balls 141

Figure 6-19. Multi-ball impact frequency for different ball numbers for balls with 3.94 mm in radius 142

Figure 6-20. The mean impact velocity in $o'-x'y'z'$ system as a function of ball number for 2-gram balls 143

Figure 6-21. Fraction of impacts as a function of impact velocity for different numbers and size of balls 144

Figure 6-22. Impact force and maximum elastic pressure for impact at a velocity of 1.5 m/s between two balls with a radius of 33.48 mm 146

Figure 6-23. The calculated critical impact velocity for different size of balls between ball and ball and between ball and wall. 146

Figure 6-24. Powder volume mechanically milled (%) per second for different number and size of balls 148

Figure 6-25. The number and size of milling balls that could reach the best milling efficiency 149

Figure 7-1. Schematic Representation of Planetary Mill Motion 155

Figure 7-2. The geometry of the planetary vial 155

Figure 7-3. The location of a ball in the vial 158

Figure 7-4. Ball original positions in planetary mill 160

Figure 7-5. Schematic representation of an Attritor mill 161

Figure 7-6. Calculated trajectory of 2-gram ball corresponding to different rotation speed of the vial (rpm) for a cylindrical vial 169

Figure 7-7. Example images showing the positions of the vial and balls at different times after milling starts for five balls in the planetary mill 170

Figure 7-8. Example images showing the positions of the impeller and balls at different times after milling starts for twelve balls in the Attritor mill 171

Figure AI-1. Two different size balls compressed together with a thickness of powder in between 175

Figure A3-1. Schematic diagram showing the probable positions of balls during impact 178

Figure A3-2. The probable positions of balls A and B during impact when one ball is too close to the cylindrical wall 179

List of Tables

Table 3-1. Parameter's in Huang et al's experiment 88

Table 3-2. Errors comparing between simulation results and Huang et al.'s experiment 90

Table 3-3. Momentum and Momentum Changes in Huang et al's experiment 90

Table 6-1. Size of balls used in simulation 122

Table 6-2. Measured Parameters 123

Table 6-3. Impact frequency in different periods during milling using 5 balls 135

Table 6-4. Effective impact frequency/impact frequency for different conditions 147

Table 6-5. Powder volume per second could be mechanically milled (%) 147

Table 6-6. Time needed for MA 95% of the powder (min) 149

Table 7-1. Parameters for the planetary mill 170

List of Symbols

α	the angle the arm of the planetary mill rotated
β	the angle the vial of the planetary mill rotated
Δ	the instantaneous elastic deformation of tools at distance r away from contact center
Δ^*	the instantaneous elastic deformation of tools at the brink of contact area
Δt	time step
δ_z^e	the instantaneous elastic deformation at distance r away from contact center
δ_z^{e0}	the instantaneous elastic deformation at distance r away from contact center at previous calculation step
δ_r	the deformation of powder compact at distance r away from contact center
$\dot{\varepsilon}$	normal strain rate
$\dot{\varepsilon}_e$	equivalent strain rate
$\dot{\varepsilon}_\theta$	normal strain rate in θ direction
$\dot{\varepsilon}_r$	normal strain rate in r direction
$\dot{\varepsilon}_z$	normal strain rate in z direction
$\dot{\varepsilon}_{xy}$	shear strain rate in x direction acting in the plane perpendicular to y direction
ε_r^e	the elastic strain at the point distance r away from contact center
ϕ	the angle between shaft arm and line OY
ϕ	angle
μ	the viscosity of powder compact
ρ	the radius of contact area
σ_r	the normal stress at the point in r direction

σ_s	the flow stress of powder compact
σ_z	the normal stress at the point in z direction
σ_z^b	the compress stress in z direction at the surface of the compressing hammer
τ_s	the flow shear stress of powder compact
τ_{ϖ}	the shear stress due to friction force caused by ball spinning
τ_{xy}	the shear stress in x direction in the plane perpendicular to y direction
τ_v	the shear stress due to friction force caused by relative movement of tools in direction r
$\tau^{ij}{}_{\omega y}$	the shear stresses on ball i from ball j due to the friction force caused by the spinning of balls in y direction
$\tau^{ij}{}_{\omega z}$	the shear stresses on ball i from ball j due to the friction force caused by the spinning of balls in z direction
$\tau^{ij}{}_{vy}$	the shear stresses on ball i from ball j due to the friction force caused by the relative movement of the balls in y direction
$\tau^{ij}{}_{vz}$	the shear stresses on ball i from ball j due to the friction force caused by the relative movement of the balls in z direction
ν	Poisson's rati
θ	the co-ordinate values of the point in θ direction
θ_0	the starting angle between shaft arm and axis y when milling starts
θ_b	the friction angle of powder on ball surface
θ_p	the friction angle between powder particles
ϖ	the angular velocity of impacting tools
ϖ'	the angular velocity of impacting tools at time $t+\Delta t$
ω	the angular velocity of crankshaft rotation
ω_p	the angular velocity of planetary arm
ω_v	the angular velocity of the vial of planetary
ψ	impact angle

ψ_{pb}	the angle formed by the cone resting on ball surface
ζ	the sinkage at a point caused by a pressing force at distance L away from this point
ξ	constant
a_L	the acceleration of vial in the direction perpendicular to shaft arm in plane yoz
A	the contact area during compression
$A(r)$	a function of r
b	coefficient
c_1	constant
d	the length of shaft arm
d	the distance between two impellers for attritor mill
d_0	the distance from the first impeller to the bottom of the container for attritor mill
d_{ij}	the distance between ball i and ball j
d_{ic}	the distance beween ball i and cylindrical wall
d_{ieL}	the distance between ball i and the left end of the vail
d_{ieR}	the distance between ball i and the right end of the vail
$d\delta_z$	the instant approach between tools at distance r away from contact center
$d\delta_z'$	the instant approach between tools at distance r away from contact center when powder flow from inner layer is considered
$d\delta_z^e$	the instant elastic deformation increase at distance r away from contact center
dV_{r-dr}	powder flows from from layer $r-dr$ to layer r
E	Young's modulus of elasticity
F	resistant force
$f(r,\theta)$	a function of r and θ
$\vec{F}^{ij}$	the vector of the resistant force acting on ball i by ball j
F_x	the resistant force caused by friction in x direction

F_y	the resistant force caused by friction in y direction
F_z	the resistant force in z direction
g	gravity acceleration
G	gravity force
h	the thickness of powder compact at distance, r, away from contact center
h_0	the maximum thickness of powder compact
h_{max}	the maximum thickness of powder coating because of friction interlock between powder particles and between powder particles and the surface of ball
h_{min}	the minimum thickness of powder coating
h_p	the maximum thickness of powder coating accumulated on ball surface considering ball traveling inside the container
h_r^*	the thickness of powder compact if elastic deformation is fully recovered at r distance away from contact center
H	tools' instant distance
H_0	tools' distance when impact starts and the same as powder's original thickness in value
H_v	the height of the vial for planetary mill
J	rotational inertia
k	the effective elastic coefficient of springs 1, 2 and 3
k'	coefficient
k_4	the elastic coefficient of spring 4
k_e	the elastic coefficient of powder
l_0	the initial length of spring 4
l_1	the length of spring 4 when $\phi = 0$
L	the length of force arm acted by vial on shaft arm
L	the distance between two points
L_4	the force arm of spring 4 on the crankshaft
L_{eL}	the distance from the left end of the vial to o' in Figure 6-1

L_{eR}	the distance from the right end of the vial to o' in Figure 6-1
L_v	the length of vial
m	the mass of a ball
m_v	the mass of vial
M	the mass of whole mill
n	number
P	pressing force
p	the contact pressure at distance r away from central axis
p^e	the resistant pressure components caused by elastic deformation of powder compact
p^{vp}	the resistant pressure components caused by visco-plastic flow of powder compact
$p(\psi)$	the probability of that an impact happens at an angle ψ with another ball in the same size
r	the co-ordinate value of the point in r direction
r	radius
r_b	the radius of ball
r_b	the distance between point B to the contact center
r_e	the coefficient of restitution
R	the radius of tool surface
R	the radius of the curvature of the internal surface of the vial for planetary mill
R_b	the radius of ball
R_c	the radius of crankshaft
R_d	the radius of the central axis of the attritor mill
R_e	the equivalent radius of tool's surface
r_i	the radius of impeller
R_i	the length of impeller
R_{di}	the radius of the center shaft of the attritor mill

R_m	the radius of the container of the attritor mill
R_p	the length of the arm for the planetary mill
R_v	the radius of vial
S	the position of impacting tools
S'	the position of impacting tools at time $t + \Delta t$
t	time
t_{max}	the time for the impact force to reach its maximum value
T	the toque caused by friction force
$\vec{T}^{ij}{}_z$	the vector of the torque acting on ball i caused by the friction force acted from ball j
T_y	the toque caused by friction force in y direction
T_z	the toque caused by friction force in z direction
v	the approaching velocity of impacting tools or the rate of powder flow
v'	the approaching velocity of impacting tools at time $t + \Delta t$
v_L	ball velocity along the vial length direction
v_r	flow rate in r direction within powder compact
v_z	flow rate in z direction within powder compact
V_b	the volume of ball
$V_{Container}$	the volume of container
V_{balls}	the total volume of balls
V_{imp}	powder volume in every impact
$V_{\max}$	the maximum powder volume in every impact
$V_{\min}$	the minimum powder volume in every impact
V_p	total powder volume
$\dot{W}_v$	virtual work rate
X	the co-ordinate value of the point in X direction
x	the co-ordinate value of the point in x direction

Y	the co-ordinate value of the point in Y direction
y	the co-ordinate value of the point in y direction
Y_M	the displacement of fulcrums
Z	the co-ordinate value of the point in Z direction
z	the co-ordinate value of the point in z direction

Chapter One

Introduction

High energy ball milling has been widely used in laboratories and industry to process powder materials. One of the applications of high energy ball milling process is to enable mechanical alloying of two or more metals. To achieve mechanical alloying, the milling must be performed under inert or controlled atmosphere.

High energy ball milling of solid powders involves repeated impacts between balls and between balls and the vial wall. These impacts cause plastic deformation, fracture and cold welding of powder particles trapped at the collision points, and thus lead to formation of composite particles (if two or more solid phases are involved). This composite structure becomes increasingly finer with continued milling. In some systems, once the composite structure becomes sufficiently fine, solid state reactions between the starting phases are activated during milling, leading to mechanical alloying [1,2]. This is true mechanical alloying. In other systems, true mechanical alloying cannot be achieved, but it has been demonstrated that this composite structure plays a vital role in determining the reaction kinetics during subsequent heat treatment of milled powder [3].

It has been well recognized that there are many factors, which influence the high energy ball milling process. These factors include ball number and size, density of ball material, powder properties and characteristics, ball/powder weight and volume ratio. With so many influencing factors, it becomes very difficult (if not impossible) to quantify the relationships between the controlling factors and the outcome and efficiency of the process through experimental studies. Therefore, developing

comprehensive mathematical models and conducting simulations based on the models become essential in order to quantify the relationships between the process conditions and powder microstructure and other characteristics of the processed powders.

As shown in Figure 1-1, the ultimate aim of the study on milling process is to build up the relationships between the process parameters and process outcomes and to simulate the microstructure change during milling so that it is possible to design and optimise the milling conditions to achieve a particular purpose of high energy ball milling efficiently. To achieve this aim, models to simulate (a) the microstructure change during an impact and (b) impact velocity distribution and impact pressure distribution as functions of time during milling need to be built. The present work was carried out in an attempt to develop a set of comprehensive models to achieve (b), while (a) is left to the future work.

Similar to the definition made by Maurice and Courtney [4] on the functions of the models, the models for ball milling are separated into two main parts: local models and global models. The local models consider many factors involved in the impact process during high energy ball milling. These factors include the deformation of tools, the elastic and plastic deformation and viscous flow of powder trapped in the impact; the different forms of impacts, such as head-on impact, oblique impact between spinning balls and multi-ball impact, and the volume of powder trapped in the collisions. The global models depend on the types of mills (attritor mill, vibratory ball mill or planetary ball mill), since each type of mills have unique operating mechanics. They are used to simulate the mechanics of different mills, the positions and velocities of balls and to determine the impacts during milling.

The local and global models are mutually dependent. With the combination of the two types of the models, it is possible to simulate the dynamics of high energy ball milling. The local models predict maximum pressure at each impact, while the

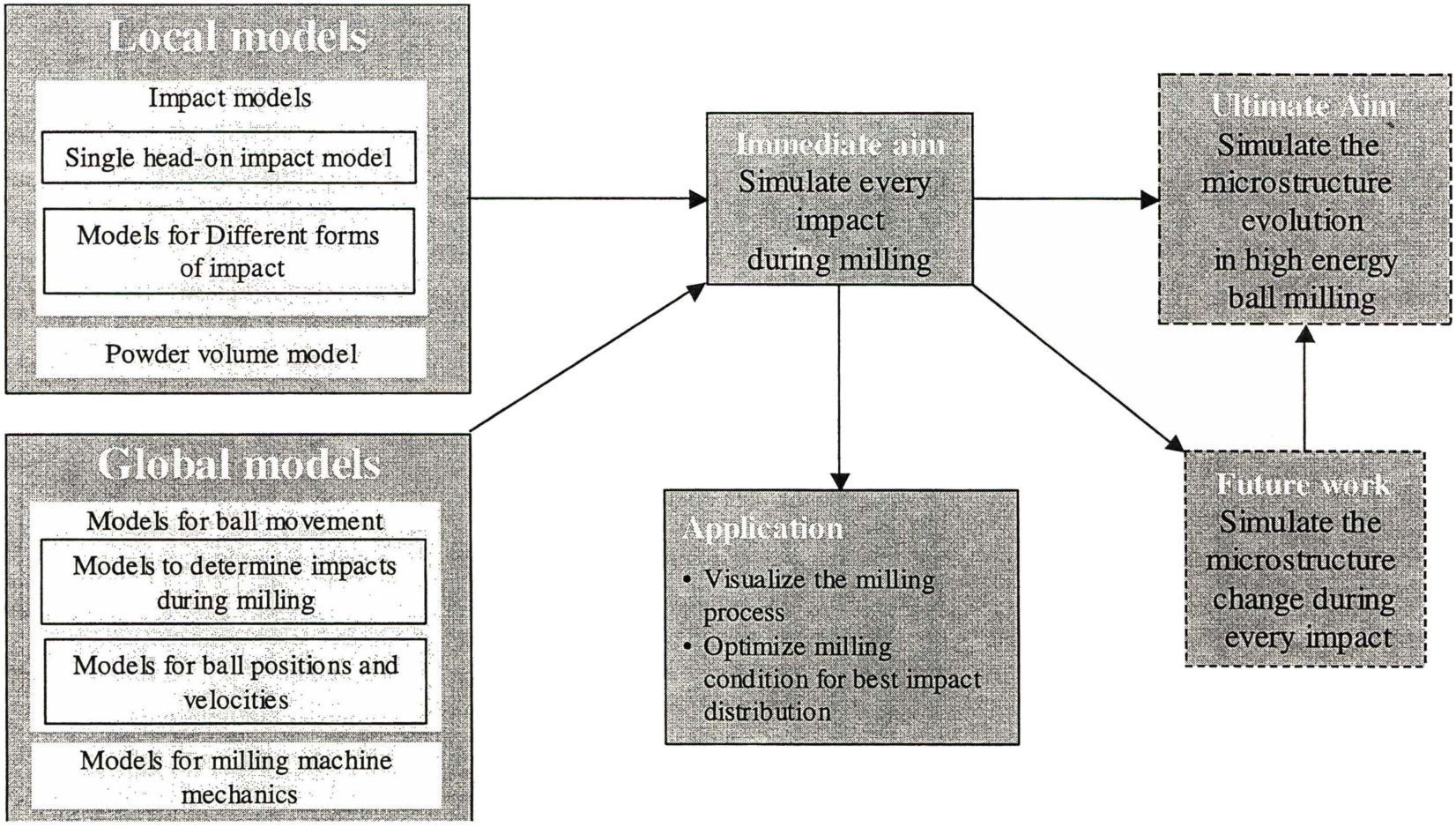

Figure 1-1. Schematic diagram showing the logical development of this work

global models predict trajectory of balls and impact frequency distribution. In the combined model, the global models are to feed the local model with the velocity; and the local models are to feed the global model with the ball velocity and position after impact.

This thesis consists of 8 chapters. Chapter 1 is an introduction. Chapter 2 introduces the background of this work by presenting a literature review on high energy ball milling process and mechanical alloying. Emphasis is placed on the mechanisms of high energy ball milling and the work aimed at modeling the high energy ball milling process.

Chapter 3 and Chapter 4 introduce the local models to simulate the impact process with a powder compact trapped in between. Chapter 3 presents and validates the basic model of head-on impact process considering the elastic deformation of balls, and the elastic and plastic deformation and viscous flow of powder compact. The aim of this chapter is to determine the change of impact pressure during an impact. Chapter 4 introduces the models to simulate the other forms of impact including oblique impact between spinning balls and multi-ball impact and to calculate the thickness and volume of the powder coating at the time of an impact.

Chapter 5 presents a three-dimensional model to simulate the global behaviour of a SPEX-8000 Mixer/Mill. The vial motion is numerically described based on the mechanics of the machine. The dynamics of balls are described based on the impact mechanics introduced in the second part. Chapter 6 presents the results of the simulations based on the models for the SPEX-8000 Mixer/Mill. They include the visualization of the vial and balls with different ball number and size, and the distributions of impact velocities and impact angles.

Chapter 7 introduces the models for planetary mill and attritor mill and also some preliminary simulation results. These models are parallel to the model introduced in

Chapter 5 in function. Chapter 8 presents the conclusions of the present work and recommendations for future work.

Reference:

[1] Koch, C.C., Calvin, O.B., McKamey C.G., Scarbrough, J., "Preparation of amorphous $Ni_{60}Nb_{40}$ by mechanical alloying", *Journal of Applied Physics Letters*, **43**, 1983, 1017.

[2] Weeber, A.W., Bakker. H., "Amorphization by ball milling: a review", *Physica*, **B153**, 1988, 93.

[3] Zhang, D.L. and Ying, D.Y., "Solid state reactions in nanometer scaled diffusion couples prepared using high energy ball milling", *Materials Science and Engineering*, in press.

[4] Maurice, D, Courtney, T. H., "Modelling of mechanical alloying: part I. deformation, coalescence and fragmentation mechanisms", *Metallurgical Transactions A*, **25A**, 1994, 147.

Chapter Two

Literature Review

2.1 Introduction

This chapter contains a review of literature on mechanical alloying (MA), equipment used and materials produced by MA. Emphasis is placed on the mechanisms of MA. The work aimed at modeling the MA process is also reviewed. The aims and objectives of this thesis are presented in the final section.

2.2 History of Mechanical Alloying

MA is a solid state reaction process, in which a mixture of powder(s) is converted into an alloy by facilitating a series of high-energy collisions in a controlled (usually inert) atmosphere. In MA, powder particles are repeatedly deformed, fractured and cold welded [1,2]. This is in contrast to conventional ball milling, in which powder particles are simply mixed while particle size, shape and density change little.

In 1930, a process similar to MA was reported [3]. The process was used to coat WC with Co. MA was developed by Benjamin and co-workers around 1968 at INCO's Paul D. Merica Research laboratory [4]. It was a by-product of research which aimed to overcome the disadvantages of powder blending without encountering the difficulties associated with ultra-fine powders [1,5]. The driving force behind the research was the desire for increased performance of gas turbine components [1,4,6].

Milling was conducted using a conventional ball mill in an attempt to inject nickel coated refractory oxide particles into nickel based superalloys. The intent was to produce an alloy combining the benefits of oxide dispersion strengthening with gamma prime precipitation hardening for high temperature applications. It was found that when certain combinations of metals were milled together in the absence of a lubricant, they tended to form metal composites. These metal composites are difficult to produce by normal means. The process was extremely long, produced hazardous and fine powders, and was generally unsuccessful. Nevertheless, a number of key ideas [5] were developed, which led to the development of MA as a powder processing technique.

The initial experiments in MA were on the production of nickel and Ni-Cr-Al-Ti alloy with thoria dispersions. The success of these experiments led to the first patent on this process. Thus MA was invented as a new alloying process, which "offered promise as a means of developing alloys with high strengths at elevated temperatures for applications such as jet engine components" [7].

Figure 2-1 shows the chronological evolution of the MA process. It should be noted that MA was firstly patented by INCO [8] in 1969 and commercialized by INCO's rolling mills in 1972 [9], these points are not shown in Figure 2-1. Figure 2-2 shows the approximate number of publications per year related to MA from 1971-1993. Most of the work prior to the 1980s focused on the production of oxide dispersion strengthened (ODS) superalloys (Ni- and Fe-base) and Al alloys, and the number of publications each year was small. The first successful amorphization by MA [10] created a great deal of interests in the MA process. Now MA has become a worldwide field of research. A number of conferences are held periodically on this scientifically interesting and technologically important topic. The journal *The International Journal of Mechanochemistry and Mechanical Alloying* has been published since 1994. The number of publications every year in this field has increased rapidly and has now reached over 700 articles per year. MA has been widely used to produce a number of materials, such as ODS alloys, amorphous

phases, quasicrystals, intermetallic compounds, nanocrystals. There have been a number of general reviews [11, 12, 13, 14, 15] plus two comprehensive reviews [16, 19], one literature bibliography [17] and one review-like book [18] in this field.

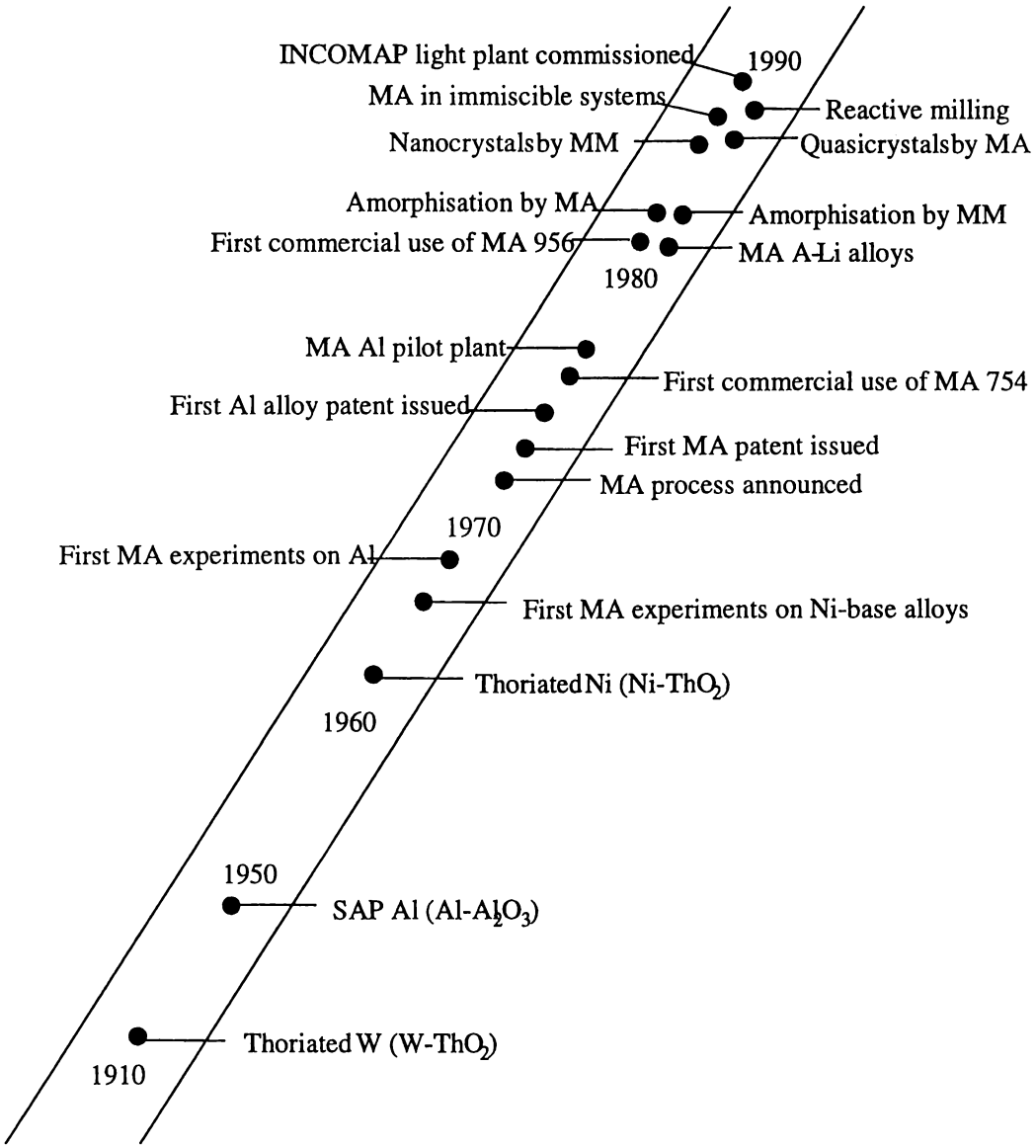

Figure 2-1. Chronological evolution of MA process modified from Murty and Ranganatha's review [19]

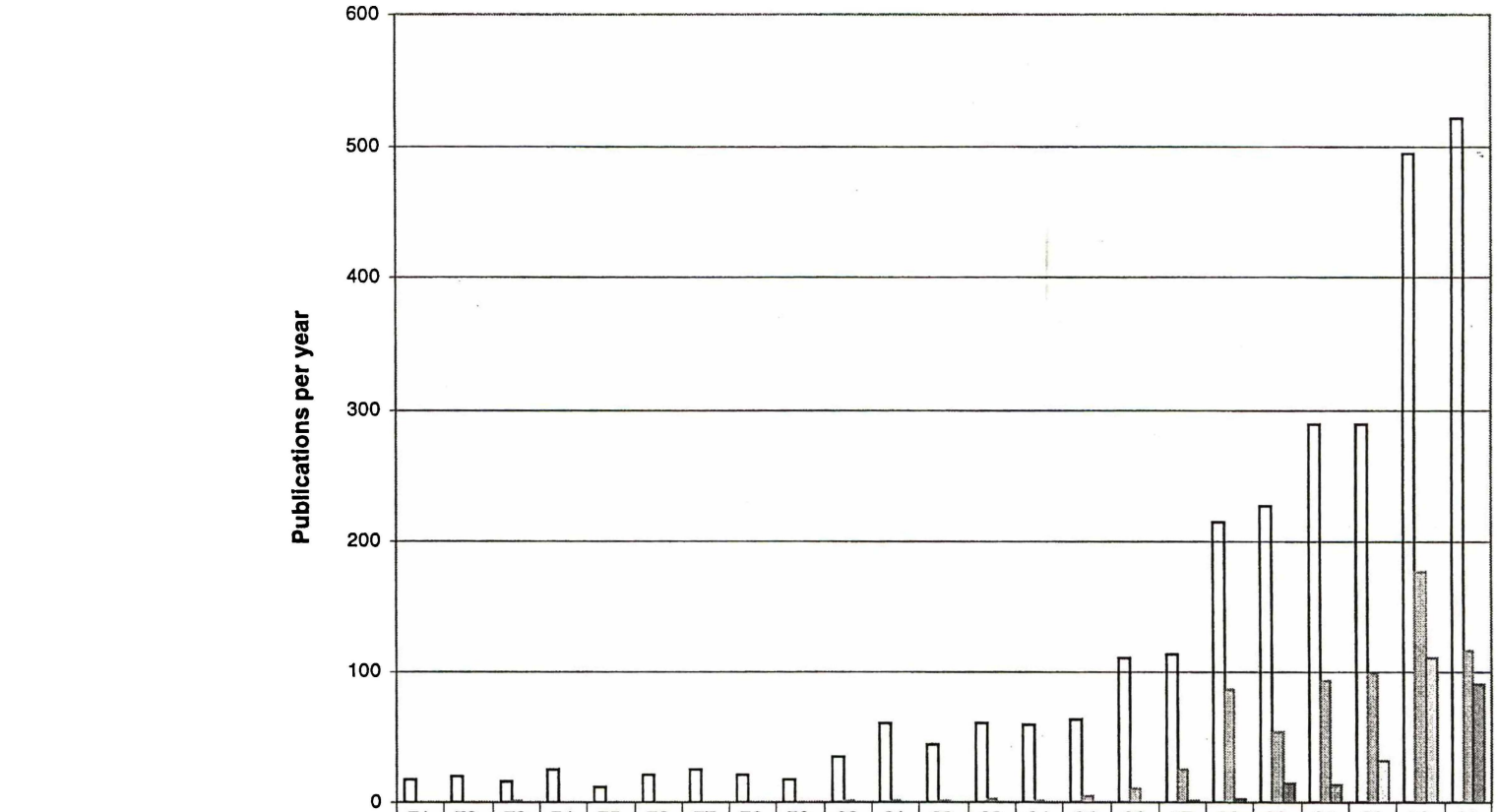

	71	72	73	74	75	76	77	78	79	80	81	82	83	84	85	86	87	88	89	90	91	92	93
Publications on MA	17	20	16	26	12	21	26	21	18	35	61	44	61	59	64	111	113	214	226	288	288	495	522
Publications on Amorphization from MA			1							1	2	1	3	2	6	11	26	86	54	93	98	176	116
Publications on Nanostructure from MA																	1	3	15	13	33	110	90

Figure 2-2. Number of publications per year before 1993

2.3 Equipment Used to Achieve Mechanical Alloying

In MA, a powder charge is placed in a container, known as a bowl, vial or jar along with a suitable grinding media under inert or other controlled atmosphere. Typical grinding media used include hardened steel balls, stainless steel balls or ceramic balls. The container containing the powder mixture and milling media is then placed in a ball-milling machine to start the MA process.

There are four types of milling machines which are most widely used for MA: attritor mill, conventional horizontal ball mill, vibratory ball mill and planetary ball mill. There are also other types of mills such as rod mill [20], modified rod mill [21] and discus mill.

2.3.1 Conventional Horizontal Ball Mill

Conventional horizontal ball mills, or tumbling ball mills, as shown in Figure 2-3, rotate around a central horizontal axis. In such mills, the powder and balls are placed in a drum of diameter greater than 1 m. The rotating speed of the drum must be just below the critical speed that would pin the balls to the internal wall of the mill, thus the impact frequency is generally low. Due to the large drum diameter that is required to generate enough impact energy, this type of ball mill is not suitable for laboratory scale research. It finds its use in industry where large quantities of powder particles can be mechanically alloyed in a single batch. Processing times are typically in the order of days [4,11,18,22,23]. Compared to others, this kind of mill is fairly economical.

A modified version of the horizontal mill named "uniball mill" (Figure 2-4) was invented by Calka and Radlinski [24]. This mill uses a stainless steel horizontal cell with hardened steel balls. The movement of balls is controlled by an adjustable external magnetic field. This innovation enables the balls to be able to run independently and to produce impacts of different energy level.

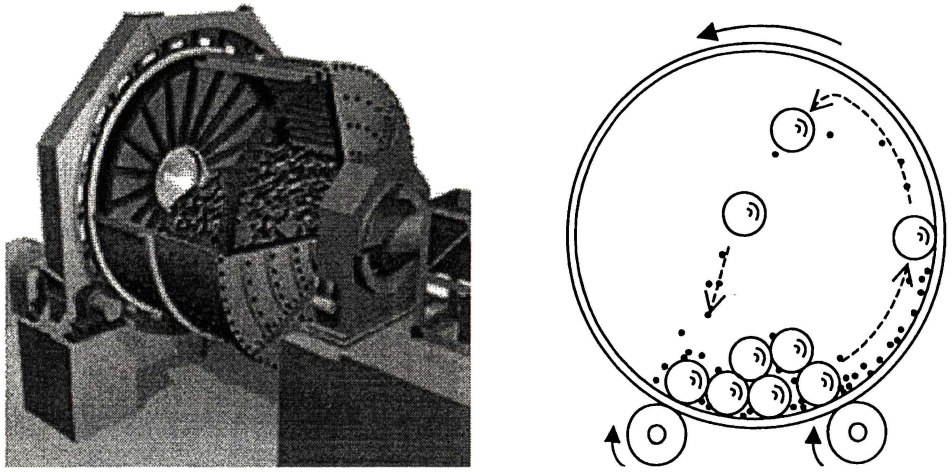

a. Mill [25]

b. Schematic diagram showing a conventional horizontal mill [18]

Figure 2-3. Conventional horizontal ball mill

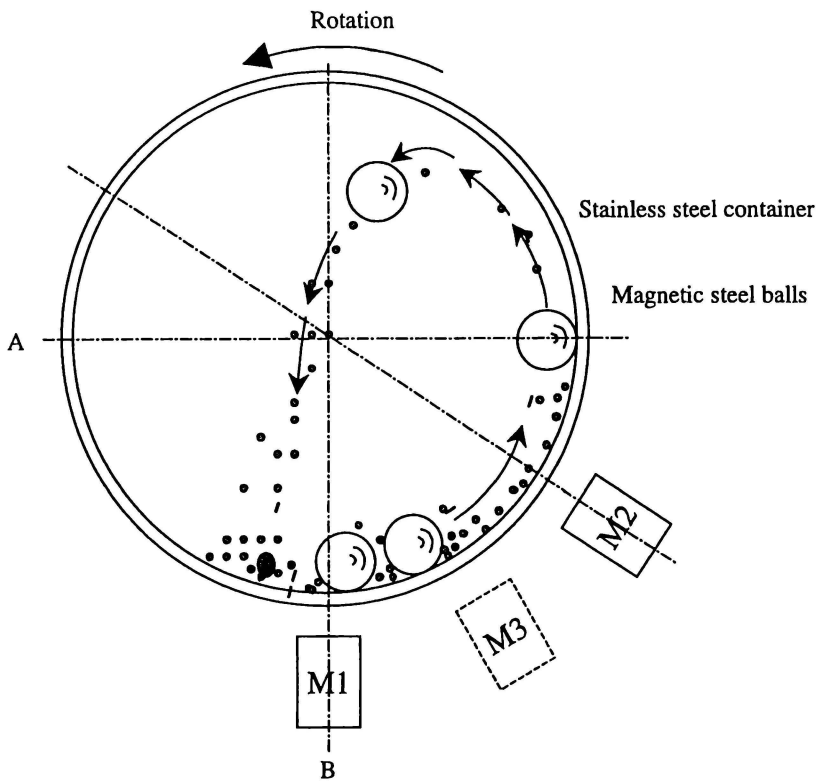

Figure 2-4. Uniball mill [24]

2.3.2 Attritor Mill

An attritor mill was the first high-energy ball mill used for MA by Benjamin [4]. Usually this type of mill is vertical as shown in Figure 2-5a. Its central shaft, along with the impellers, rotates at a speed of up to 250 rpm in the stationary container [22]. The balls inside are agitated, generating high-energy collisions between the steel balls and the powder charge. Due to the high-speed rotation of the shaft, the

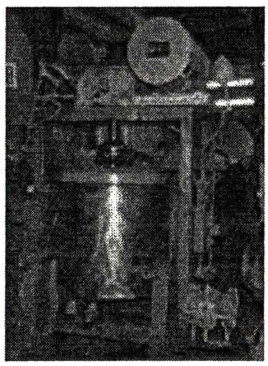

Mill [26]

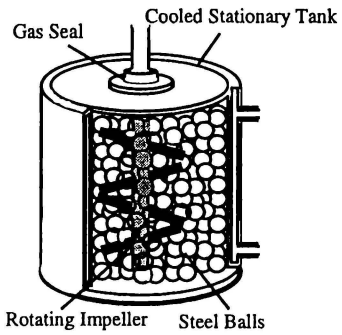

Schematic diagram showing a vertical attritor [22]

a. Vertical attritor

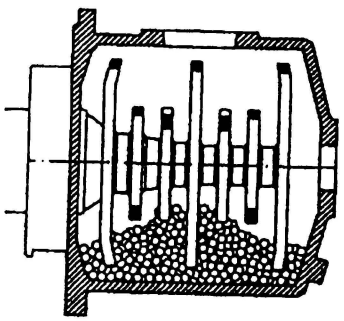

b. Horizontal attritor or Simoloyer [28]

Figure 2-5. Vertical and horizontal attritors

capacity is somewhat limited. It can be used to process a moderate volume of materials ranging from $3.8x10^{-3}m^3$ to $3.8x10^{-1}m^3$ in milling times typically in the order of hours [4,11,18,22,23]. The relatively high frictional motion between the central shaft and the steel balls, and between the container and the steel balls can easily cause contamination of the powder. To reduce this contamination, milling tools employed can be coated with the same material as the material to be milled. Since the container is stationary, it can be easily cooled by water. However, gravity causes dead zones in vertical attritor mills [22].

Another type of attritor mill is horizontal, and is known as Simoloyer (Figure 2-5b), which is developed by Zoz in Germany [27,28,29,30]. It is a rotary ball mill combining advantages of both the horizontal mill and attritor mill. In this mill, a horizontal borne rotor rotates at a high speed and the balls are set in motion by this rotor. It is suitable for both laboratory and industry with a powder production from 50 gram up to half a ton [28].

2.3.3 Vibratory Mill

The vibratory mill such as the SPEX-8000 shaker mill is shown in Figure 2-6. The SPEX-8000 mill operates by agitating a small grinding vial at high frequency in complex cycles, which involve motion in three dimensions. This type of mill, which is highly energetic compared to attritor mills, was originally developed to pulverize spectrographic samples. The vial has a capacity of up to 55×10^{-6} m^3, making this type of mills ideal for research purposes as they

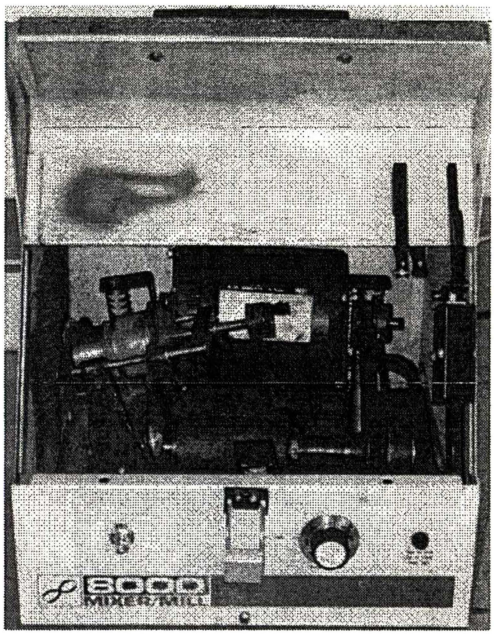

Figure 2-6. SPEX-8000 Mixer/Mill

produce small quantities of powder (less than 15 g) in relatively short times [4,11,18,22,23].

Another kind of vibratory mill is the shake ball mill (Figure 2-7) [31]. It only has a single ball in it and has been used both as a device for MA and as a tool to investigate the effect of system dynamics on the milling process [11].

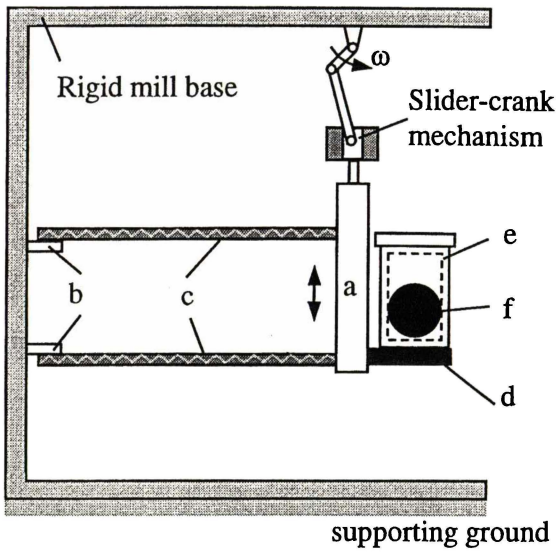

Figure 2-7. The schematic diagram of the shake ball mill [31]

2.3.4 Planetary Ball Mill

A planetary ball mill is frequently used for MA. The machine is suitable for research purposes in laboratories as it produces a small amount of powder, as small as a few grams. A typical planetary ball mill is shown in Figure 2-8. The motion of a planetary mill involves rotation of the bowl about two separate parallel vertical axes, analogous to the rotation of the earth about the central axis of itself and about the sun. It consists of one sun disc and two or four planetary bowls. The sun disc rotates in one direction about its center while the bowls rotate in the opposite direction about their own axes. The centrifugal forces created by the rotations of the bowl around its own axis and of the rotating disc are applied onto the balls and the powder mixture in the bowl. The

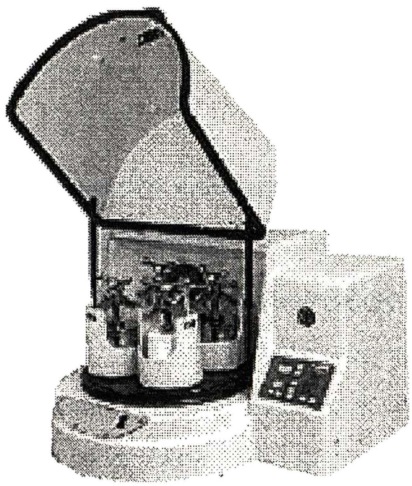

Figure 2-8. Planetary ball mill

impact is intensified when the balls collide with one another. The impact energy of the milling balls can be changed by altering the rotational speed of the sun disc. The advantage of this type of ball mill is not only that high impact energy can be obtained but also high impact frequency, which shortens the duration of the MA process [18].

2.4 Materials Produced by Mechanical Alloying

Mechanically alloyed materials generally show excellent mechanical properties, for instances, MA6000 combines the high strength of the cast alloy at lower temperature of about 1,033K and creep resistant at high temperatures of up to 1,373K [32]. The value of MA becomes apparent when attempting to make an alloy that cannot be fabricated in any other way. MA can be used to synthesize a large variety of materials including ceramics, intermetallics and composites. It can circumvent many of the limitations of conventional alloying techniques, such as alloying two metals with widely different melting points [1]. It is also an alternative to other non-equilibrium processing methods, such as rapid solidification and physical vapor deposition [33]. Although there are a few exceptions where it cannot be used to synthesis some alloys [34-39], MA provides a useful alternative for materials designers.

2.4.1 ODS Alloys

Early applications of the MA technique were mainly confined to produce ODS alloys [22], typically of superalloys [40,41] and aluminum alloys [42]. The repeated cold welding and fracturing of the powder particles in an inert atmosphere leads to formation of oxide layers on the surfaces of the powder particles, as well as of layered structures. With extended milling process, even the thin oxide layers are continuously broken into small pieces, which are incorporated into the microstructure of powder particles and therefore lead to formation of oxide dispersion strengthened alloys [4].

2.4.2 Amorphous Materials

In 1979, White [43] used a SPEX shaker mill to alloy elemental powders of Ni and Sn. Although his aim was to prepare A15 superconducting precursor powders, he noticed that an amorphous phase might have been synthesized as a by-product. The first detailed study of amorphization was carried out by Koch et al. [10] in the glass-forming alloy system Ni-Nb, using a SPEX-8000 Mixer/Mill. The milling was carried out in air or in helium. It was reported that during the milling the apparent "crystallite size" decreases rapidly to the value that corresponds to that of the eventually obtained amorphous alloy. Amorphization by MA was proved by comparing the X-ray diffraction pattern and the recrystallization temperature of the powder produced by MA to that of the rapidly solidified alloy.

Since then, amorphization using MA has generated wide research interests [44,45, etc]. It has been shown that amorphous alloys might be produced from either elemental powders or intermediate alloys. Kim and Koch [46] have observed the formation of Nb_3Sn as an intermediate product of amorphization of Nb-Sn in a SPEX vibratory mill. Similar results have been reported in the Nb-Ge [47], Nb-Si [48], Fe-Sn [49] and Zr-Al [50] systems. In the Ni-Zr system a new type of amorphization reaction has been found [51,52], in which crystalline intermetallic compounds form as intermediate products when a planetary mill is used for MA. It has also been found that MA in a vibratory ball mill results in the direct formation of an amorphous phase without any intermediate stage. Amorphization by MA of ternary alloy systems has also been reported [53-55]. Amorphization by MA has many advantages over other methods, such as a wide glass formation composition range, simplicity and ease of production.

2.4.3 Extended Solid Solutions

In general, binary systems in which the atom sizes differ by more than 15% show very limited mutual solubilities [56]. However, these solubility limits can be greatly

extended by MA [13]. Metals with positive heats of mixing, such as copper with iron, niobium, vanadium, or tantalum, which are very difficult to be alloyed by using conventional methods, can be mechanically alloyed, forming extended solid solutions or amorphous phases [57]. This outcome is the same as that achieved by rapidly quenching a melt of the same composition [16], although it has also been agreed that adiabatic melting processes do not occur during MA [34,39].

2.4.4 Intermetallics

Intermetallics have many novel attributes, including high strength at elevated temperatures and thermal stability, good high corrosion/oxidation resistance, unique electrical and magnetic properties. However, they are difficult to produce by conventional ingot metallurgy methods because of high melting points and high tendency of segregation. The ability of MA to overcome these difficulties has attracted interests of many material scientists. Intermediate phases and intermetallic compounds have been synthesised from elemental powders by MA in several alloy systems. Jang et al. [58] studied the dispersion of Al_2O_3, Y_2O_3, and ThO_2 in Ni_3Al powders by MA. The dispersoids were found to decrease the grain size of the intermetallic and hence increase its yield strength, however the room temperature ductility was reduced. Koch and Kim [59] have synthesised the intermetallic compounds Nb_3Ge, Nb_5Ge_2 and $NbGe_2$ by MA pure Nb and Ge, and similarly producing Nb_3Sn and Nb_6Sn_5 by MA of pure Nb and Sn. In the cases of Nb_3Sn and Nb_3Ge, continued milling eventually resulted in the formation of an amorphous phase.

A number of intermetallic compounds have been produced with MA as the first step in the synthesis procedure. Some applications for mechanically alloyed intermetallics include permanent magnets [35] and hydrogen storage materials [60]. Benn et al. [61] reviewed the work on several intermetallic compound systems where an intimate mixture of the elemental components was attained by MA, as well as partial

compound formation in some cases. Koch [62], Koch and Whittenberger [63] have recently reviewed the work on synthesis of intermetallics using MA.

2.4.5 Nanostructured Materials

The formation of nanocrystalline structures by high-energy ball milling has widened the scope of MA. The first systematic study of the synthesis of nanocrystalline elemental metals by MA was reported by Fecht et al. [64]. In the process of studying the mechanism for amorphization of intermetallic compounds, they observed microstructural changes as well as a build-up of stored energy with increasing milling time in a series of bcc (Fe, Cr, Nb, W) and hcp (Zr, Hf, Co, Ru) metals. It was found that as milling progressed, a dislocation cell structure developed, sharpened and transformed into a nanocrystalline grain structure consisting of high angle grain boundaries and fine grains in sizes of 9 to 13 nm.

Nanocrystalline structures were obtained by high-energy ball milling of a number of elemental powders such as Cr, Nb, W, Hf, Zr, and Co [64], Fe [65, 66], Ag [67] and C [68]. Nanocrystalline solutions have been synthesized in a number systems by MA such as Ti-Si [69], Ti-Ni, Ti-Cu [15] and Cu-Zn [70].

In recent years, there have been considerable efforts to produce in situ nanocomposites by MA. Provenzano and Holtz [71] have shown the formation of Ag-Ni and Cu-Nb nanocomposites by MA. Zhu et al. [72] have synthesized Pb-Al and Fe-Cu nanocomposites. Du et al. [73] have produced Al-BN composites by high-energy ball milling. In an interesting report, Naser et al. [74] have shown that no grain growth occurs in the matrix close to its melting point when Cu and Mg are reinforced with nanocrystalline Al_2O_3 by MA.

2.4.6 Composite Materials

One key advantage of MA is that it can easily achieve composition and microstructure homogeneity. MA provides a good method to produce metal-ceramic composite powders [6,18]. Reinforcements in metal matrix composites include carbides, nitrides, oxides and other elemental phases. MA overcomes the problem of agglomeration of reinforcement particles caused by size differences, which is often encountered in conventional powder metallurgy process. The composite materials produced using MA include Ni-based [1,4,6,18] and Al-based composites [18,75].

2.4.7 Quasicrystals

There have been several reports on the formation of quasicrystals [76,77]. It has been shown that different metastable phases were produced at different milling intensities, and that quasicrystals might serve as an intermediate phase [77].

2.5 Understandings of Mechanical Alloying Process

Since its invention people have been trying to understand the mechanisms of MA in the hope of being able to optimize and control the milling process. The issues include:

- the dynamics of milling media;
- how the morphology and microstructure of powder particles evolve during milling;
- what factors affect the milling process and final outcome; and
- how to explain the phase formation, such as crystalline to amorphous materials or intermetallics to nanocrystallines in this special process.

The first issue is fundamental to understanding the milling process. Enough information on the dynamics of milling media will result in an in-depth understanding of the milling process. It will be delineated later in Section 2.6. The remaining three issues are built upon understanding of the dynamics. They are discussed in the following section.

2.5.1 Particle Morphology and Microstructural Evolution

Observations on the morphology and microstructural evolution involved have been made since MA came into use. Mostly, the milling would be interrupted and a small amount of the powder would be sampled at different times. SEM, optical microscopes and XRD have been used to follow the milling process. By now the morphological and microstructural evolution during MA is qualitatively understood, especially for ductile/ductile and ductile/brittle systems. It has been accepted that both cold welding and fracture, which distinguish MA from conventional ball milling, happen during the process. Every time steel balls collide or a steel ball collides with the internal wall of the mill, powder particles are trapped. The force of the impact deforms the particles and creates new atomically clean surfaces [1,6,78]. Thus cold welding can occur between two such surfaces when they are compressed into contact during subsequent collisions. Solid state reactions can then occur across these new, internal interfaces, allowing the chemical composition of the particles to change progressively during milling.

The powder morphology and microstructural evolution that occurs during MA is critically dependent on the ductility of the powders. There are three possible systems: ductile/ductile, ductile/brittle, and brittle/brittle systems [6, 11].

2.5.1.1 Ductile/Ductile Systems

The most complete description on the ductile/ductile systems was given by Benjamin and Volin [1,2], based on the observation of the morphology and microstructural evolution during MA of Fe-Cr. They divided the process into five time intervals, as schematically described in Figure 2-9.

- **Initial Period**

The first stage involves mixing, deformation, fracturing and welding of powder particles. This stage is exemplified by the development of both coarser and finer particles from those in the initial powder charge. Powder particles within the coarser fraction initially are of plates formed by flattening of equiaxed particles and have the same volume as the starting powder particles. Toward the end of this period, an increasing number of composite particles with the different ingredients arranged in parallel layers also appear in the coarser size fractions. The finer powder particles are predominantly equiaxed and represent fragments from the particles within the starting mixture. The powder size distribution does not change drastically during this time period and both powder particles and welded layers remain relatively ductile. Due to

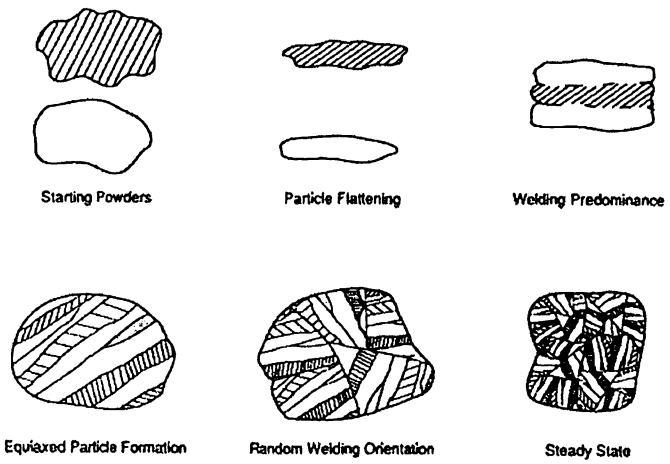

Figure 2-9. The five stages of MA as described by Benjamin and Volin [2]

the statistical nature of the process, the hardness of the particles is widely scattered and there is significant variation in the morphology of the particles.

- **Period of Welding Predominance**

During this period, there is a substantial increase in the relative amount of the coarser fractions while the amount of the finer particles remains largely unchanged. The particles in the coarser fractions display a multi-layered composite structure with lamellae running parallel to the longitudinal axis. The fine particles remain elemental but are now predominantly flake-shaped. These fine powder particles are probably pieces fractured from the edges of the coarser composite particles that were not cold-welded to other lamellae.

The hardness of the particles shows a substantial increase over that of the starting powders as virtually all material has been severely deformed.

- **Period of Equiaxed Particle Formation**

A sharp decrease in the amount of large flake-shaped particles is observed with a trend toward more equiaxed particle formation. This is probably the result of a significant decrease in ductility of the composite powder particles. The change in the structure of the finer powder particles, however, is much more startling. It is marked by the virtual disappearance of elemental powder fragments and the appearance of composite particles consisting of parallel lamellae of a structure similar to those of the coarser powders. These powder particles have originated from the fracturing of similarly structured particles within the coarser fractions. At the same time, the smaller elemental particles have mostly been captured by welding to other particles.

- **Start of Random Welding Orientation**

Within this time period, the lamella spacing decrease, and lamellae become

convoluted or marbled rather than being linear. There is a similar tendency toward convolution of the lamellae in the finer powder fraction. The appearance of this convoluted structure is due to welding together of equiaxed powder particles without any preference to the orientation with which they weld. During this stage of processing, there is a continuing increase in particle hardness and concurrent decrease in ductility, which leads to an increased tendency for particle fracture.

- **Steady-State Processing**

Steady-state processing is characterized by increasing internal microstructural homogeneity and refinement of all particle size fractions to a degree that can no longer be followed optically. There is a reasonable balance between the frequencies of particle fracturing and welding and thus, the average particle size does not change much during this stage nor does the distribution in particle sizes. However, the internal microstructure of powder particles becomes finer and finer. The hardness of the free powder approaches saturation.

Kuschke et al. [79] also investigated the powder milling process of the ductile/ductile system. Their results from studying Ni_3Al and $Fe_{60}Al_{40}$ allow a significant extension of the earlier approaches. It was concluded from their studies that the milling process could be subdivided into three periods:

Period 1 : Only plastic deformation occurs, followed by fracture of deformed particles.
Period 2 : Welding events start to occur, while fracture and plastic deformation continue, but with decreasing dominance.
Period 3 : An equilibrium between fracture and welding of highly strain-hardened powder particles is established. Plastic deformation plays a negligible role.

When comparing the three periods of Kuschke et al. [79] with the five periods postulated by Benjamin and Volin [2], it can be seen that period one in the Kuschke

model corresponds to the initial period of Benjamin and Volin. A period of welding predominance was not found, nor was there a distinct period of equiaxed particle formation observed. However the period of random welding orientation and perhaps the period of equiaxed particle formation can both be included in Period 2. Benjamin and Volin's period of steady state processing can be compared with period three postulated by Kuschke et al..

2.5.1.2 Ductile/Brittle Systems

The early work of Benjamin and coworkers on the ODS alloys is a typical example of a ductile/brittle system evolved during the MA of ODS alloys [4,6,11,80]. In these systems, the hard brittle powders are fragmented during milling and the fragments are trapped at the boundaries between the ductile particles which are flattened by plastic deformation. This event is summarized in Figure 2-10.

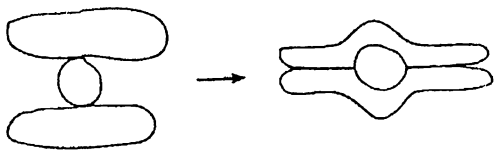

Figure 2-10. Schematic diagram of the microstructural evolution that occurs during MA of ductile/brittle systems [23]

At first, the welds are far apart and the concentration of the brittle particles at each weld is rather sparse. With further processing, the spacing between the welds decreases, and the spacing of the brittle particles along each weld increases. The distance between the brittle particles is roughly equal to the spacing of the welds. Finally, when the powder has been processed to the point where the welds cannot be detected with a light microscope, a fine dispersion of brittle particles results. Further processing cannot enhance this nearly random dispersion of brittle particles in the metal matrix [11].

2.5.1.3 Brittle/Brittle Systems

In the initial stages of development of the MA technique, it was thought that the milling of brittle/brittle components would result only in the fragmentation of the individual components to the limit of comminution without any alloying [6]. However it has been shown that the MA of certain nominally brittle components can lead to homogeneous alloys. For example, this technique has been utilized to form diamond-cubic solid solutions in the Si-Ge [81] system, intermetallic compounds in the Mn-Bi [81, 82] system, and amorphous phases from $NiZr_2$-$Ni_{11}Zr_9$ [83] intermetallics. Although the mechanism for MA of brittle components is not well understood, it is observed that the microstructural evolution during milling differs markedly from that described previously for ductile systems. Davis and Koch [81] made an interesting observation while characterizing particle morphology of brittle components during MA. In these systems, namely Si-Ge, Mn-Bi, and alpha quartz, numerous cases of interparticle necking were observed. They also found that the mechanically alloyed powders did not appear consistency of elemental particles, rather they appeared to be composed of smaller composite particles formed by cold-welding together.

2.5.2 Influencing Factors

2.5.2.1 Factors Influencing Powder Contamination

Milling media, including balls and container, may intercalate a substantial amount of Fe into the milled powder. It has been reported that stainless steel media causes heavier Fe contamination than hard steel balls [84]. While, contamination can be avoided by milling the powders with a milling media made up of the same material as that of the powders being milled [16], this is difficult to put into practice. Contamination also depends on the type of milling machine and milling speed. The use of less energetic mills has been suggested in order to reduce contamination [16,85] The recently designed Symoloyer is another alternative to minimize the contamination [28].

Milling atmosphere is also a potential source of contamination during MA. Oxygen contamination is most severe for reactive metals such as Al [86] and Ti [85]. To prevent this, inert gas, typically argon or helium is widely used to serve as the milling atmosphere. Using vacuum [87] is another alternative.

Another type of contamination might come from the process control agents, which are used to modify the surface of the deforming particles. Addition of a suitable processing control agent impedes the clean metal-to-metal contact necessary for cold welding [22] thus reducing cold welding and promoting fracture. It has been shown that process control agents such as Nopcowax-22DSP, get incorporated into aluminum powder within 25 min resulting in contamination of the powder [88], although they are usually added in very small quantities (<1%).

Ironically, some processes may take advantage of contamination. The introduction of disorder catalysts, such as the contamination of Fe, has been suggested to improve ductility in some brittle materials, such as aluminides and Cu-Ni [15]. Oxygen contamination has been reported to lead to crystallization of amorphous phases in the Ni-Ti system [89]; hydrogen contamination can act as a catalyst for the amorphization reaction in the Ti-rich compositions in the Cu-Ti system [90].

2.5.2.2 Milling Intensity

As the powder particles are subjected to high-energy collisions, the final products are influenced by the milling intensity [91]. The higher the milling intensity, the more energy dissipated in the form of heat, which leads to faster diffusion processes [18]. Any factors, which influence the milling intensity, might affect the milling results. These factors include ball to powder weight ratio [18,92,93], speed of media [94], and even the shape of the container [95].

Niu [92] studied the influence of ball/powder weight ratio on Al-Fe system using a planetary ball mill under a constant milling condition. He found that the micro-

hardness of the powder increased continuously with the increase in weight ratio due to an enhanced and accelerated plastic deformation of the powder particles, although the rate of hardening decreased. The mean particle size on the other hand, exhibited a different trend. It was observed that the average particle size decreased dramatically initially to a minimum value when the weight ratio was increased from 2:1 until 5:1. Then the mean particle size started to increase to a maximum value at a ball/powder weight ratio of 11:1, thereafter, a steady decrease was observed. The ball/powder weight ratio used is generally in the range between 10:1 and 20:1 [12,93]. Normally horizontal ball mills tend to use high ball/powder weight ratios and in some extreme cases, as high as 500:1 [18]. Weight ratios of about 5:1 or less are often employed when vibratory ball mills are used [18].

Eckert [94] studied the influence of milling intensity on $Al_{65}Cu_{20}Mn_{15}$ mixture with a planetary mill. The intensities investigated corresponded to the maximum ball kinetic energy of 14, 29, 49 or 76 mJ respectively. X-ray diffraction study showed that at an intensity of 29 mJ, the formation of amorphous phase started after 30,600 minutes of milling. However, milling for the same time but at a lower intensity resulted no solid state reaction. An icosahedral phase was formed for milling at an intensity of 49 mJ. The highest intensity output a nanocrystalline material with CsCl-type structure, and this remained unchanged during further milling. It was estimated that the resulting maximum temperatures at collision points are 403, 520, 680 and 863 K respectively.

Harringa et al. [95] studied the effect of different shape of vial by mechanically alloying heavily doped $Si_{80}Ge_{20}$ in a flat-ended vial and in a round-ended vial. It was found that the powder milled in a flat-ended vial alloyed at a considerably faster rate than in the round-ended vial.

2.5.3 Mechanism of Phase Formation during MA

Unlike thermal reaction in melting or sintering at high temperature, MA is normally a

low-temperature reaction process, as described previously. It has been used to prepare a variety of alloy powders, including powders of extended crystalline solid solution, amorphous phases and intermetallics.

In an effort to explain the phase formation of new materials during MA, a number of mechanisms have been proposed from different points of view. These include atomistic models [96, 97], thermodynamic models [98,99,100] and kinetic models [101,102,103]. All of these models can explain some of the following phenomena during MA, but are not capable of explaining all of them.

- Formation of extended solid solution in binary systems having both positive or negative heats of mixing.
- Formation of amorphous alloy phases in binary systems having negative heat of mixing.
- Lack of solute partitioning: as Ma and Atzmon [104] showed, when mechanically alloying mixtures of aluminum and zirconium powders, the milled product had a composition nearly equal to that of the starting powder mixture and that the alloy product did not partition during MA.
- Difficulty in mechanically alloying mixtures of metal and metalloid powders [34,35].

While a recently proposed pump diffusion model proposed by Schwarz [105], which combines the ideas of atomistic reaction, thermodynamic and kinetic mechanism, according to Schwarz, is capable of explaining all of the above unusual effects observed during MA. Thus the mechanism of phase formation is qualitatively understood.

This idealized model is schematically shown in Figure 2-11 [105]. Fracturing and cold welding of particles during MA of ductile elemental powders A and B and creates a large number of dislocations and other lattice defects. Based on dislocation kinetics and the diffusion of solutes along the dislocation cores, dislocations interact with

solutes through various locking mechanisms: chemical, elastic, electrostatic, and stress-induced order-locking, which may operate concurrently. As described by Schwarz [105], the interaction is strongest when the atomic volumes of the solvent and solute are largely different, which is also the case leading to restricted mutual solubility. Thus solutes larger or smaller than the matrix atoms are attracted to the expanded or compressed lattice regions near the cores of edge dislocations. In Figure 2-11, the solute atoms (A) should easily penetrate the core of edge dislocation in crystal B even if crystals A and B have a positive heat of mixing, provided this heat of mixing is smaller than the dislocation-solute interaction energy. The dislocations also affect the solute diffusivity. Because the core of edge dislocations has a highly dilated region below the extra atomic plane, the solutes that segregate to the dislocation cores can diffuse along the cores with an activation energy which is about half that needed for bulk diffusion.

During the MA process, the powder particles are moving freely inside the mill for most of the time. During this time the dislocations are arrested with respect to the A/B interfaces and A and/or B atoms are able to diffuse along the cores of dislocations in B and/or A, respectively, as indicated by thick lines in Figure 2-11b. As the solutes have an attractive interaction with the dislocations, the solute

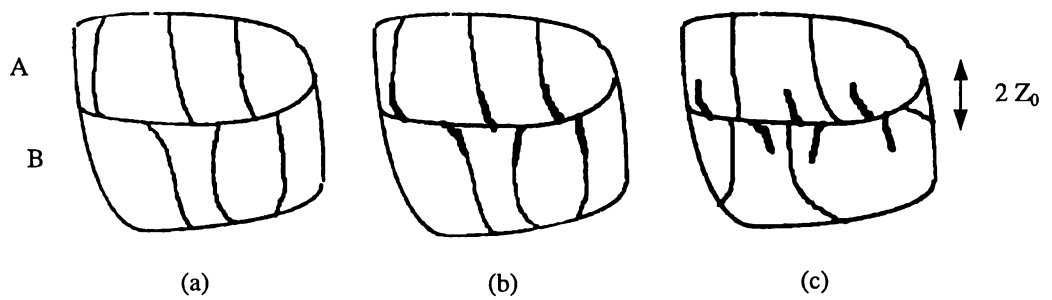

Figure 2-11. Particle with an A/B boundary (nearly horizontal). Dislocation in A and B (nearly vertical lines) intersect the A/B boundary. Figure (a), (b) and (c) denote successive times in the MA process. For clarity, the shape of the particle has been assumed constant [105].

concentrations in the cores will attain values largely in excess of the equilibrium solubility of A in B, or B in A.

Subsequently the particles, trapped between colliding balls, will experience an applied stress pulse exceeding the flow stress of either A or B, even in their work-hardened condition. As a result, some or all of the dislocations in the powder particle will be forced to glide and leave their previous positions. However, the solutes, which had diffused along the dislocation cores, will not be able to follow the fast moving dislocations and thus will be left behind, inside crystals A and B, as linear chains of solutes, in states of high supersaturation. In this mechanism, the dislocations act as agents for the intermixing, allowing for a one-way, up-hill (energetically) motion of the solutes into the opposite matrix. Thus, after repeating many times, effective alloy intermixing will occur along a narrow fringe of width $2Z_0$ parallel to the A/B interface.

The phase formation induced during MA is mainly dependent on the dynamics of milling media. The controlling factors include the energy transferred during the collision of the media with the powder, the frequency of these collisions, and the deformation behavior of the powder. Owing to the lack of sufficient knowledge on the dynamics of milling media, one cannot expect that the predictions to be accurate. The prediction can only tell within the same magnitude as the reality and show the general trends.

2.6 Modeling/Simulation of the Dynamics of Milling Media

2.6.1 Overview

MA is a process involving repetitive cold welding and fracture of powder caused by repeated impacts from milling media. From this point of view, the outcome of MA is

a function of powder property and milling dynamics. Thus knowing the dynamics of milling media during milling is essential.

The motion of milling balls in vibratory mills was first investigated by Kousaka et al. [106] and Inoue [107]. Kousaka et al. [106] found that the balls inside the mill move randomly by observing through a transparent vibratory mill and using a stroboscope. This random motion of balls poses the technical difficulty in measuring the impact force or the impact energy of individual balls because a huge number of random collisions occur within a very short time. Inoue [107] tried to analyze the motion of balls in a vibratory mill during grinding of powder particles by means of model simulation, using a one-dimensional mill model. The balls in his model were assumed to be rigid bodies having a coefficient of repulsion less than unity. It turned out that it was no longer possible to analyze the motion of more than six balls by his model because the impact frequency became nearly infinite under these conditions.

Subsequent modeling/simulation work [21,23,31,36,80,82,108-158] has addressed the difficulty aimed of better understanding the milling process. The final purpose is to design better equipment and to quantify the milling process.

Most of the studies on modeling and simulation are carried out by the following four groups: Maurice and Courtney [23,80,82, 112,108-117,119] from USA, Gaffet et al. [21, 120-123] from France, Hashimoto and Watanabe [124-129] from Japan, and McCormick et al.[31,130-134] from Australia.

Maurice [112] pioneered systematic study by modeling the dynamics of milling media and Maurice and Courtney [23,80,82,108-117,119] have published the majority of the work in this area. They classified the modeling/simulation into two interdependent types: local and global [112-114]. The local model [23,108-120] was defined to describe the various effects (thermal and mechanical) and events (deformation, fracture, and welding) when powder particles are entrapped between two colliding or sliding surfaces. The global model [109-111,118,119,135], which is device specific (attritor mill, conventional horizontal

ball mill, vibratory ball mill or planetary ball mill), must entail the study of factors such as the distribution of impact angles and the heterogeneity of powder distribution within the mill, factors that clearly differ from one type of mill to another. A large part of their work is about the local model considering elastic deformation of balls, the volume trapped per impact, and the deformation, cold welding, fracture, and temperature change of powder particles during impact. Although the events other than cold welding and fracture of powder particles have not been well described, the model has been used to calculate the particle size of the milled powder. Their global models on attritor and SPEX mills are dependent on experimental measurement [118] or simulation results from somewhere else [82], which includes impact frequency and impact velocities.

Gaffet's group [21, 120-123] simulated planetary mills and horizontal rod mills by using a two-dimensional model. The analytical mechanics, which is not capable of considering the ball rotation and slip, was employed to calculate the detachment of the balls, movement of balls after detaching and to determine the impact points on the vial. Although this group had deduced a model to simulate the impact process by a simple rheological body [120], this model was not combined with the models of the planetary or horizontal rod mills.

Hashimoto and Watanabe [124-129] conducted simulations on planetary and horizontal ball mills. in a different way from those described above, they employed the Kelvin model to describe the ball-powder-ball impact process. The frictions in oblique impacts were also considered. This Kelvin model has been converted into numerical models in one, two and three dimensions and the ball motion could be determined step by step.

McCormick's group have simulated one dimensional vibratory mills [131] and two dimensional planetary mills using analytical mechanics [130] and numerical methods [132,133]. Their outstanding contribution was that they employed a modified Kelvin model to describe the ball-powder-ball impact process. This model has been

validated by calculating and measuring the impact force distribution during the impact of freely dropping a ball onto a plate with a thickness of powder on it [131] and has been proved to be the best among the single impact models [132]. This model has been used to simulate the impact process in planetary mills [132,133].

In the following sections the work on modeling/simulation will be reviewed from the points of different effects, events happening during an impact (local model) and different mills (global model).

2.6.2 Deformation during Impact

Impacts are basic events in high-energy ball milling. How an impact happens is an unavoidable question in simulating a milling process. On the other hand, determination through simulation of parameters such as the impact stress, strain and duration time is useful for calculating cold welding, fragmentation and temperature increase. There are several different kinds of deformation during impacts: ball deformation, plastic and elastic deformation of powder compact and powder flow. Several methods have been used to simulate the impact process. However, there has been no study capable of describing all of the above deformations. Some even evade them by using a simple rigid impact [107]. The important models are Maurice and Courtney's Hertz impact model [23,112,114] and plastic/elastic model [108,113], Hashimoto and Watanabe's Kelvin model [124-129] and Dallimore and McCormick's modified Kelvin model [132,133]. Other models are from Bhattacharya and Arzt [137], Rahouadj and Gaffet [120] and Inoue and Okaya [143].

Hertz impact model [159] holds only for elastic impacts and is mostly suitable for low energy and head-on modes (impact velocity is less than 7.5 m/s for steel balls [160]) between two bare balls. It was used by Maurice and Courtney [23,112,114] to determine the maximum contact area, maximum impact force and pressure and impact duration time in MA, where the impacts happens at velocities up to more than 10 m/s with powder in between. The powder compact was viewed as a forged cylindrical body

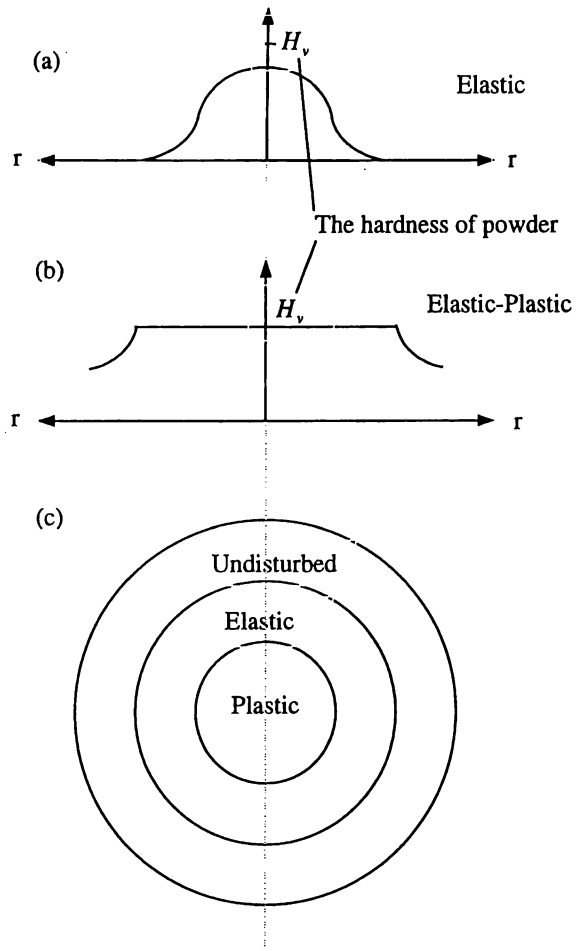

Figure 2-12. Schematic of the distribution of stress over the contact area during a collision between composite balls as described by Maurice and Courtney [108,113]. (a) Early in the collision, the balls deform elastically. (b) The powder begins to deform plastically when the stress attains yield point of powder. (c) During this stage, the center of the contact area is characterized by plastic deformation of both powder and ball, and outside this annulus there is no deformation of either (not to scale).

whose area was the Hertz contact area, and the volume of the powder compact involved in the impact had been determined by a model described in Section 2.6.4. However, Hertz impact [159] does not provide the impact pressure, force and area as functions of time. In order for the strain in the powder during this impact compact to be derived, they assumed that the velocity of the colliding objects decreased linearly with time.

In their later elastic/plastic yield model [108,113], Maurice and Courtney considered that powder particles caught between colliding balls undergo severe plastic deformation. The ball and the powder coating were viewed as a solid composite ball (assuming the powder's hardness is smaller than that of the ball) in modeling the impact process. They analyzed the collision mechanics using a method similar to those used by Andrews [161] and Maw et al. [162]. As shown in Figure 2-12, in the initial stage of impact, both powder and balls deform elastically. On further approach of the balls, the stress at the contact center attains the yield stress of powder and this stress is reached over a finite radius, which increases with time. Outside this radius, the stress distribution is the same as it would be in an elastic collision. The change of the powder hardness or work hardening was considered as a function of accumulated plastic strain. Also, both normal and tangential components of the impact force were considered in this process. Based on the above description, it can be concluded that this model is capable of providing better results than their first one. However, in this process they did not consider powder flow, which plays an important role during impact [132] when there is powder in between. It was not clear whether they used a numerical or an analytical approach in calculating the impact process.

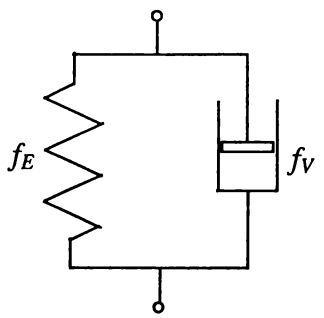

Figure 2-13. Kelvin model [124]

Hashimoto and Watanabe considered the impact process in a different way [124-129].

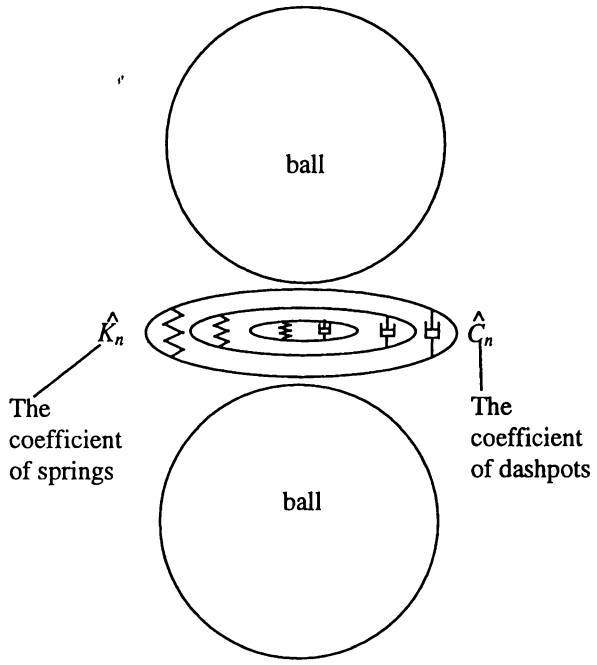

Figure 2-14. Dallimore & McCormick's modified Kelvin model [132]

Disregarding the micro-forging, cold welding and fracture of the powder particles during these collisions, they simplified these events as the impacts between two viscoelastic objects. The elastic spring component (f_E) represents the elastic deformation of the balls, which was solved by Hertz impact [159], the elastic deformation of the powder was ignored. The viscous dashpot component (f_V) is analogous of the drag force of powder flow, which was expressed by a coefficient of viscosity and the effective deformation rate. The shearing force during impact was also considered by viewing the process as a visco-elastic friction that obeys the Coulomb Damp Law. The spring and dashpot were coupled in parallel in accordance with the Kelvin (Voigt) model as shown in Figure 2-13. The plastic and elastic behaviour of the powder is not considered in this model. The Kelvin model as well as the modified Kelvin model, which is going to be discussed below, has the same problem: the dashpot and spring system could not provide any physical explanation to the analogous objects [163].

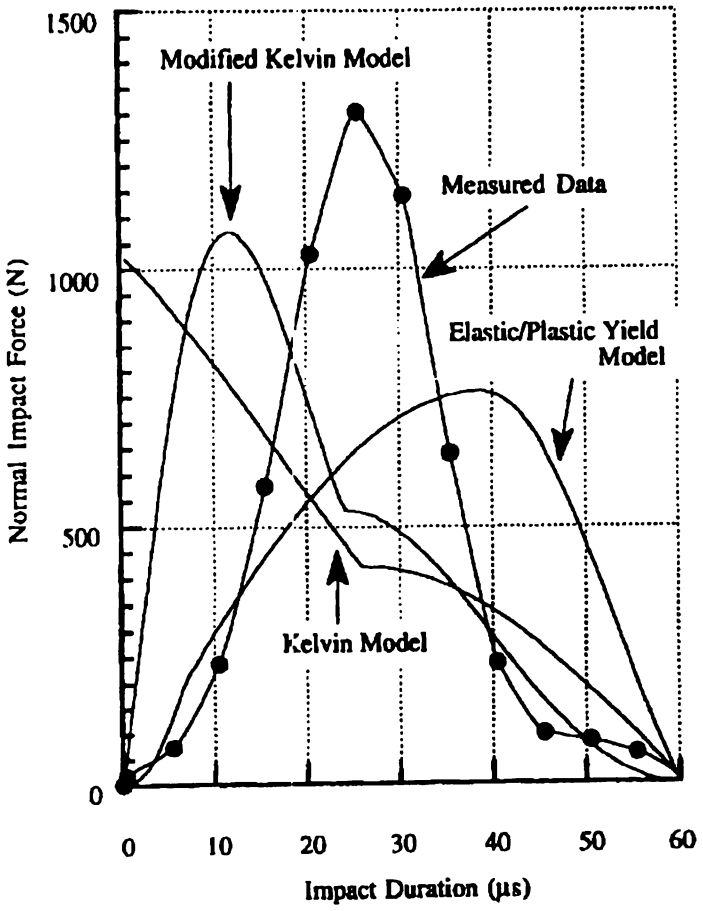

Figure 2-15. Comparison of different models and measured data [132]

Considering neither a Kelvin model nor an elastic/plastic yield model could simulate the ball-powder-ball or ball-powder-wall impact process, Dallimore & McCormick [132,133] put forward a modified Kelvin model, as described in Figure 2-14, to simulate the single head-on impact process. They assumed that the elastic force is proportional to the volume of the overlap while the damping force is proportional to both the velocity of approach and the instantaneous area of the impact. The coefficients of the spring and the dashpot have been determined by using the reverse engineering method [134]. The volumes and areas were calculated by assuming that the overlap is mainly contained within the powder coatings upon the balls and vial wall. It is not clear whether the 'overlap' refers to the elastic deformation of the impact

objects or the powder. If it is the former, there is still the same problem as described in Hashimoto's Kelvin model. If it is that of the powder, the deformation of the impact objects needs to be considered. The discrete/distinct element method (DEM) was employed in this simulation, where the system has been viewed as a number of small Kelvin models in their numerical model and the impact process was separated into small time steps. They made a comparison of the modified model with Maurice and Courtney's elastic/plastic yield model [108,113], Hashimoto and Watanabe's Kelvin model [124-129]. It shows that the modified model has better agreement with experiment in terms of the impact force as a function of time (Figure 2-15).

In simulating the impact process, Rahouadj and Gaffet employed rheological models (as shown in Figure 2-16), where E_A, E_B and E'_A are identical Young's modulus and σ_y is yield stress of powder [120]. Although the elastic and plastic deformation process could be simulated by using this model, the effect of the high strain rate, which plays an important role during high-energy milling, was ignored.

Bhattacharya and Arzt's [137] plastic deformation model considers the powder as a compact of porous particles. The pore size and porous particles were assumed to deform during the impact. The required energy to change the porosity could be quantified by using Carroll and Holt's model [164]. However, empirical equations for the deformation of balls and the plastic deformation of powder had to be used because they could not be calculated from first principle.

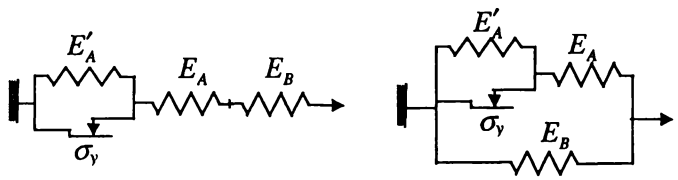

a. Serial Model b. Parallel Model

Figure 2-16. Rheological models [120]

Inoue and Okaya's model [107,143] is simpler. They considered only the coefficient of restitution during the impact. Thus from one point of view, it is only a "simplified" Kelvin model by taking away the dashpot part. It could not represent even part of the real impact process.

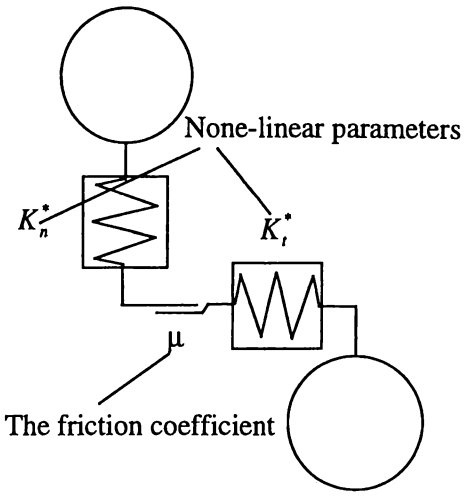

Figure 2-17. Inoue and Okaya's model [143]

2.6.3 Cold Welding and Fracturing

Cold welding and fracturing are very important events in MA. However, they have been considered only by Maurice and Courtney [108,113], although there are well understood theories to describe the cold welding and fracturing [165-167].

In Maurice and Courtney's model, cold welding was defined according to previous work by Bay [165-167]. It was assumed that the cold welding takes place only in the region over which intimate metal-metal contact is established via plastic deformation. When two particles of different hardness come together, the softer one will deform first until the two particles reach an equal hardness.

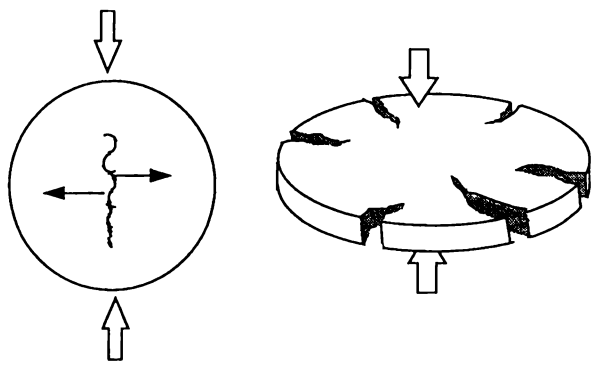

Figure 2-18. Fracture mode used by Maurice and Courtney [108,113]

In the fracturing mechanisms, it was assumed that the forging fracture (Figure 2-18) initiates during the impact when a critical tensile strain is attained and the

initial crack length is equal to the distance over which that threshold strain is exceeded. This requires that the crack exceed a certain length. If the particle is sufficiently small so that this length is greater than the particle size, the particle is considered below its comminution limit and will not fracture. Subsequent crack propagation occurs when the plastic energy release rate exceeds a value characteristic of the material.

2.6.4 Volume of Material per Collision

It is essential to know the volume of a powder cluster during an impact. Gilman and Benjamin [22] estimated that the amount of powder entrapped between two colliding bodies is around 0.2 mg. There have been few attempts to quantify this volume.

In Maurice and Courtney's first report [23,112], a theoretical sweeping mechanism was put forward by considering the influence of atmospheric force. The force resists the motion of the balls and the powder particles. Since the powder particles are much smaller than the balls, the particles experience a much greater deceleration. Thus in this model, powder was assumed to distribute uniformly throughout the free space of the container.

Considering balls flying from one end to the other in the SPEX mill, some powder particles fly away from the front of the balls while others are pushed ahead by the balls. Based on the above assumption, Maurice and Courtney [23] further assumed that as the ball approaches the surface of the vial, fewer and fewer powder particles "escape" from the path of the ball. Thus the volume of powder entrapped in the process was considered as the volume of a cone with length being $L-2R$, where L is the length of the vial and R, the radius of the flying ball [23], and the contact area is calculated using Hertz impact [159]. The swept volume for a SPEX mill is the volume of the cone as schematically expressed in Figure 2-19. By using the same method and considering the balls as a loose packed array, the swept volume for an attritor was

similarly determined.

However, this method seems only suitable for the one ball mill that vibrates only in one direction, where the ball does not touch the cylindrical wall of the vial. Since there is no scientific basis for the above assumptions, it is not surprising to see that their calculation is quite different from that experimentally estimated by Gilman and Benjamin [22].

In Maurice and Courtney's later reports [113], they assumed that balls are uniformly coated with powder. The thickness was determined by considering the friction 'interlocking' between the powder particles. The friction between balls and powder particles was also assumed to be the same as that between powder particles. Then by using geometrical (Figure 2-19) and mechanical analysis, the height of the powder cone resting on the ball could be deduced. However, the deduction seems to be wrong according to their assumption, although the approach is sound.

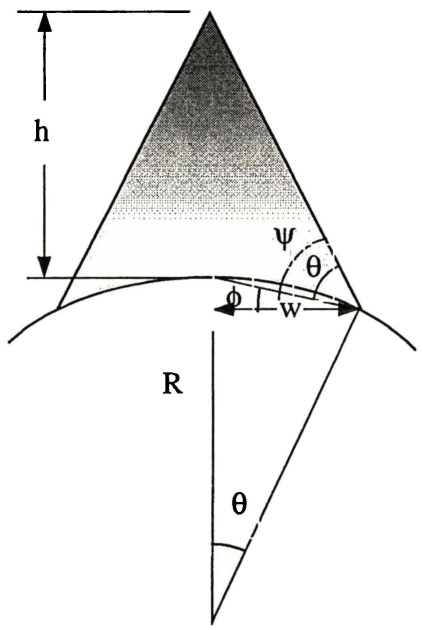

Figure 2-19. The modified 'swept' model [113].

The latest study by Gavrilov et al. [141] took an assumption that the powder particles are uniformly distributed in the container. The powder particles are supposed to be of a certain size. Thus when two balls come to contact, they will be surrounded by the powder particles and the volume enclosed by the balls and powder particles are defined to be the volume that participated in the impact. It is clear that this model is

too simple to represent even part of the practical process.

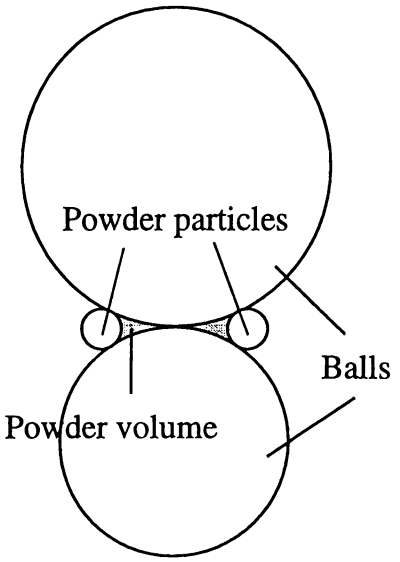

Figure 2-20. The volume of powder participated in the impact [141]

2.6.5 Temperature Increase

Schwartz and Koch [156] were the first to model the temperature increase [168], which resulted from localized shear of powder particles trapped between two colliding balls. Their calculation showed that the temperature increase was just tens of K. The impact velocity and impact duration used by them are 2 m/s and 2 μs respectively, which are both very low compared to the real condition. Davis et al. [82] used the same method. They calculated that the maximum temperature increase could reach 350 K (for $Ni_{32}Ti_{65}$) using their estimated impact velocity of 18.7 m/s (too high for a real condition) in a SPEX mill. By assuming that the plastic deformation work is entirely converted into a temperature increase in the head-on impacted powder, Maurice and Courtney [23] estimated that the temperature increase for most of materials is several hundred K. After considering the powder cooling between impacts, they found that particles will return to their pre-impact temperature before being struck again. Thus they concluded that the temperature effect is not enough to melt a powder during the milling.

2.6.6 Milling Time

Davis et al. [82], Maurice [113] and Maurice and Courtney [116] used an "average distribution method" to predict the milling time to achieve a particular particle

microstructure. This means that if *x%* of the powder experiences an impact, *nx%* of powder is going to experience impacts after *n-th* impact. However, ball milling is statistical in nature, which means that the accumulated impact process is not a "simple adding process". Thus their result cannot be relied on.

2.6.7 Global Modeling of Vibratory Mills

In the modeling of vibratory mills, a few studies have been performed on the dynamics of the shake ball mill [31,120,131] and the simplified SPEX mill [23, 111,112].

Huang et al. [31,131,153] simulated the operation of shake ball mill. The impact model [31] calculated the energy loss by multiplying the energy with a restitution coefficient. This model is similar to those of Inoue [107] and Maurice and Courtney [111]. In the simulation, a numerical method was employed. They found that the coefficient of restitution determines the observed dynamics of the bouncing ball system. Huang et al. [131] also measured the impact forces by adding a force transducer between the steel support panel and the container, which enabled them to build an empirical equation. This equation has been used to predict the impact force history during milling using the shake ball mill.

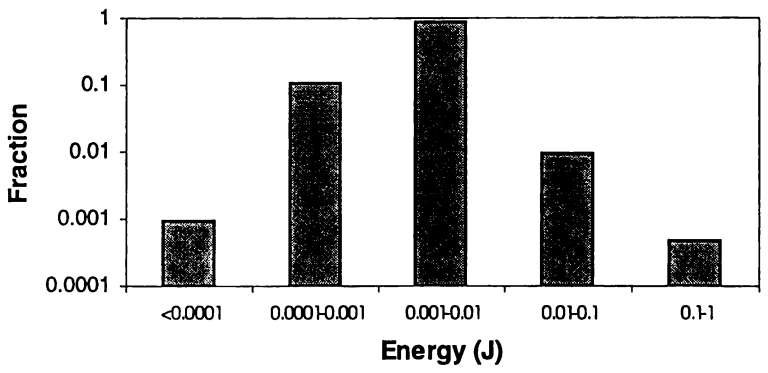

Figure 2-21. Energy Loss Distribution [114]

The most recent study of the shake ball mill was conducted by Gavrilov et al. [141]. They used a similar method to define the ball motion and container movement and their own model (see page 41) to estimate the powder volume.

The only study aimed at observing the ball and vial motion in a SPEX-8000 Mixer/Mill was conducted by Davis et al. [82]. The vial motion was recorded on videotape and then analysed by motion analysis software. Thus the trajectory of the vial was achieved. They were also the first to model the kinetics of ball milling in a SPEX-8000 mill, although it is not very clear how the ball motion was studied inside the vial. Their modeling result showed that the majority of the impacts have an energy dissipation of 0.001~0.01 J (Figure 2-21) and impact angle distribution (the triangle line in Figure 2-22).

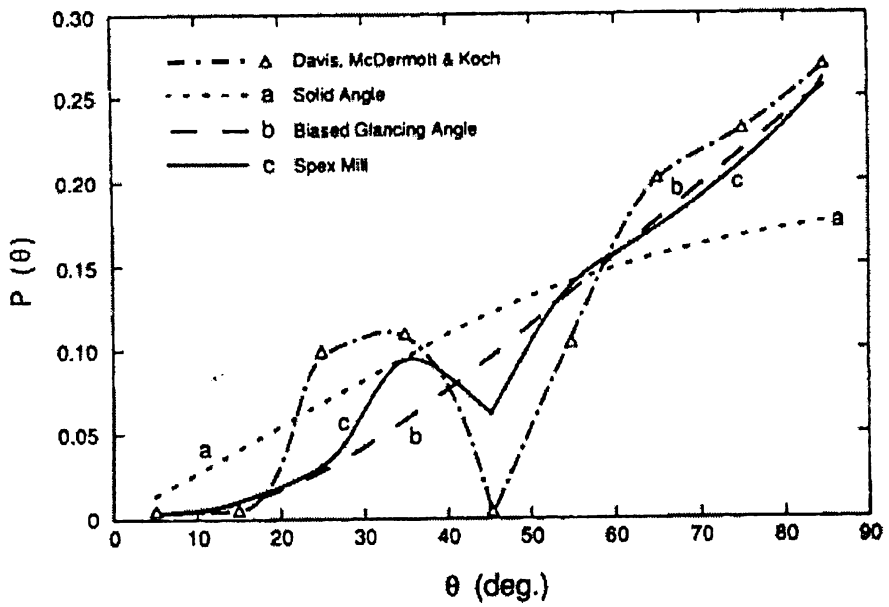

Figure 2-22. Frequency distribution of Impact Angles in a SPEX mill. The triangles represent simulation from Davis et al.'s work [114]. Results are for (a) a distribution of random, (b) a distribution of biased toward glancing angles and (c) an expected distribution with small number of balls.

Maurice and Courtney [23,112] simplified SPEX mills to a mill, which shakes in only one direction. Knowing the vial shaken amplitude and frequency, the ball velocity, which was assumed twice the average speed of the vial, was conservatively estimated to be about 3.9 m/s. Although their model could only simulate the head-on impact, they deduced the impact angle distribution (Figure 2-22) by using a geometrical probability method [114] in the aim to imitate Davis et al.'s [82] simulation result as described above. However, only one of these could mimic the trend of the angle distribution, which was based on that a small number of balls inside the vial so that there is no ball-ball impact.

In Maurice and Courtney's latest study [111], they considered the energy loss in the impact process and approached that the highest impact velocity is 6.9 m/s. They further simulated the dynamics of a one-dimensional mill, where the diameter of the vial is the same as the balls and moves in longitudinal direction only with the balls. This is their only global model that could simulate the dynamic motion in the milling process, although this motion only involves head-on impacts. A coefficient restitution e was assumed to simulate every impact process by using the following equation:

$$e = \sqrt{1 - \frac{U_p}{U_e}} \tag{1-1}$$

where U_p is the plastic deformation energy imparted to the powder calculated considering powder plastic deformation in their local model [108], and U_e the pre-collision kinetic energy. Thus they could record each collision during simulation.

The most outstanding study on SPEX mill was recently carried out by Caravati et al. [139]. They suggested a 3-D model, which describes the milling process of the SPEX mill containing only one ball and where the ball displacement was calculated step-by-step by numerical method. However, there are quite a few simplifications. They include: (a) the vial motion was depicted as an angular harmonic displacement in a vertical plane coupled with a synchronous rotation on the equatorial plane; (b) the

fulcrums were assumed to be stationary and the effect of the springs was neglected; (c) the impact was considered to be rigid; and (d) ball spinning, its effect on powder deformation and the effect of gravitational force on ball motion were ignored.

2.6.8 Global Modeling of Attritor mills

Attritor mills are complex and it is difficult to describe the motion of balls accurately. The only method used to model the ball motion is to view the media as a viscous liquid [112,151]. Lazarev et al. [151] modeled this process using a finite element method and until now, this method is still the best in this area. The simulation results are in agreement with Rydin's observation, which will be introduced later in this section. However, their model could not predict the impact velocities.

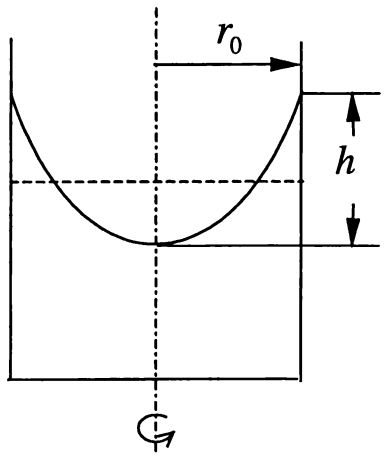

Figure 2-23. Fluid model [112] to determine the media velocity in an attritor.

Maurice and Courtney [112] also considered the milling media as a kind of liquid, which is agitated by the shaft (Figure 2-23). After measuring the height difference of the media between the center and the side, the media velocity was crudely calculated by using conventional fluid mechanics [169].

Some effort has also been directed towards calculating the relationship between specific energy and product particle size for WC regardless of the milling media [142]. The mean input mechanical energy per unit mass of powder was used to predict the product property [142]. Most recently, Zoz et al. [155] used a similar energy method for

their horizontal attritor. They calculated the energy input into the powder by calculating the difference between the energy needed to mill with and without powder, and the energy transferred to the cooling system. However, since MA is a high-energy process involving events of cold-welding and fracture, it is difficult for this model to explain the difference between the results of low energy and long time milling, and high-energy and short time milling.

Observation of ball motion plays an important role in these mills. Rydin et al. [118] observed the ball motion in an attritor mill by using cinematography to examine the behavior of the milling media by varying the rotation velocity from 0 to 250 rpm. They observed that firstly the balls in the tank are in an array of close packed and square packing. As the balls move with the shaft, the array is distorted and vacancies are produced and filled. By observing from the top of the mill, they found that 50 rpm is enough to force a significant fraction of the balls away from the attritor core and the voided region is approximately cone shaped. Increasing attritor rotational velocity exaggerates these effects: i.e., the cone volume is increased, and thus, fewer balls are located within the core and more on the periphery.

Rydin et al. [118] also measured the angular velocities of the balls as functions of the radial position in the attritor (Figure 2-24) at the mill top, bottom and the height along the sidewall (Figure 2-25). By looking at the mill from the top (Figure 2-24a), they found that the angular velocities close to zero along the attritor wall, and increase monotonically from the canister wall to the tips of the impeller arms. This velocity gradient causes the rolling/sliding events among the different layers of balls and the relative sliding is greatest for layers removed from the core. The number of sliding and rolling events are much higher than that of impacts. The velocity in the core is approximately constant.

By observing from the bottom of the mill, Rydin et al. [118] found that the ball motion is more constrained at the mill rotation speed of 50rpm, because the bottom of the impeller shaft is located two ball layers above the canister bottom and, in part,

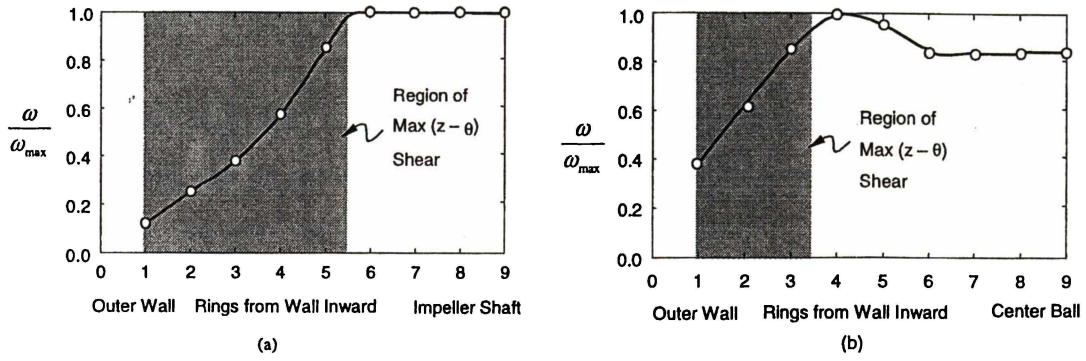

Figure 2-24. Rotational velocities (a) at the mill top for operating at 50 rpm and (b) at the mill bottom for operating at 250 rpm.

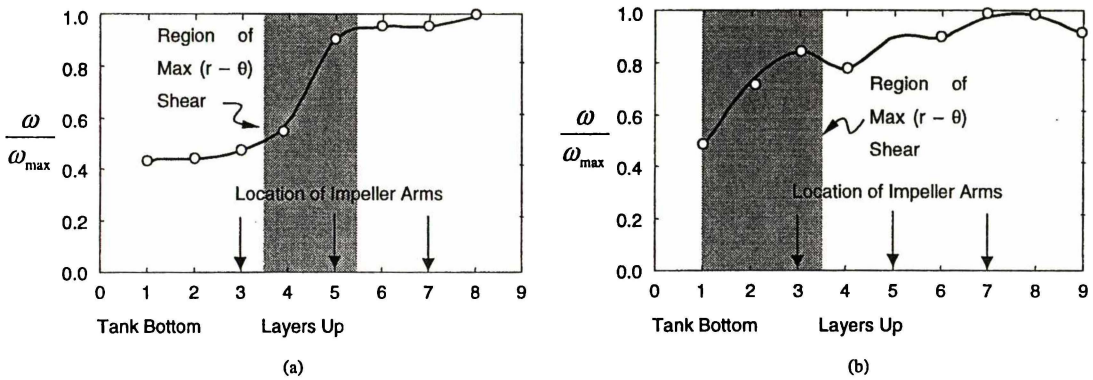

Figure 2-25. Vertical velocity gradients along the mill side for operating at (a) 50 rpm and (b) at 250 rpm.

because of the restraint on the ball motion provided by the weight of the balls in the attritor. With the shaft rotation speed of 250 rpm, they found that the rotational velocities of balls are greatest near the impeller arm tips. They suggested that there exists a possible turgid or dead zone in the area close to the canister wall.

By observing the mill through the sidewall, Rydin et al. [118] measured the velocity distribution along the height of the sidewall (Figure 2-25). They found that the impeller arms particularly located five layers above destroy the periodic array as they pass, resulting in the stepped velocity profile (Figure 2-25a). At 250 rpm, there is minimal disturbance of the close-packed array, leading to a smoother velocity profile (Figure 2-25b).

2.6.9 Global Modeling of Planetary Mills and Horizontal Mills

Since planetary mills and horizontal mills share so much similarity, the analysis on horizontal mills can be extended to planetary mills by simply replacing gravity with centrifugal acceleration. Here they are reviewed together.

Early study [170] to understand the dynamics in these mills was to evaluate the trajectories of motion of the ball during ball milling by using a graphic construction. Now observation of ball motion has been possible by using high speed photography to record the balls along certain trajectory through a transparent vial [36,129,120,135]. It has been found that certain conditions correspond to certain motion behavior of balls during milling. Such conditions include the friction coefficient between ball and wall, mill rotation speed, ball charge weight ratio.

Analytical solutions, which analyze the geometrical relation based on the classical mechanics, have been used to simulate the milling process using planetary mills or horizontal mills [36,120, 147]. Theoretically, the ball trajectory, detach angle and critical velocity have been solved by this method [36,120,138,147]. However, the motions of particles and balls are very complicated and this makes an analytical expression of mass trajectories impossible [149]. Much of the work [126-129,121,135,149,157,158] on this topic has proved that the numerical method, such as the DEM method, combined with suitable single impact model is a better way.

The containers are mostly close to cylinder-shaped and at least several times the diameters of the balls, thus most models have simplified the mills into 2-dimension [121,149,157,158]. Even though several have been performed in 3-dimension [126-129,135], their single impact models (Kelvin model, elastic/plastic deformation model and modified Kelvin model) are not sufficient to represent the real impact process.

2.7 Summary and Objectives

MA, as a robust process involving high-energy impacts of balls, can be used to produce various materials, which are either difficult or impossible to produce by ordinary means. Its mechanisms have been qualitatively understood. Although modeling studies have been performed by various researchers, there is still a long way to go before we are able to quantify this process. Better models to simulate the single impact process and 3-dimensional milling dynamics are needed to build a solid foundation for this quantification attempt.

The objectives of this thesis are:

- To develop a suitable single impact model, which is capable of describing the single impact process with powder in between.
- To build up a proper local model to portray the other basic events including the volume of powder per impact and the motion of balls considering the free movement of balls, the effects of ball spinning and oblique impacts.
- To deduce a proper global model to depict the motion of vial and balls in SPEX-800 Mixer/mill.
- To couple the global model with the local models so that the numerical simulation of the milling process could be possible.
- To illustrate the dynamics of the milling process.

2.8 References

1. Benjamin, J.S., "Mechanical Alloying", *Scientific America*, **234**, 1976, 40.
2. Benjamin, J.S., Volin, T.E., "The mechanism of mechanical alloying", *Metallurgical Transactions*, **5**, 1974, 1929.

3. Hoyt, S.L., "Hard Metal Carbides and Cemented Tungsten Carbide", *AIME Trans.*, **89**, 1930, 9.

4. Benjamin, J.S., "Dispersion strengthened superalloys by mechanical alloying", *Metallurgical Transactions*, **1**, 1970, 2943.

5. Benjamin, J.S., "Fundamentals of mechanical alloying", *Materials Science Forum*, **88-90**, 1992, 1.

6. Schaffer, G.B., McCormick, P.G., "Review article mechanical alloying", *Materials Forum*, **16**, 1992, 91.

7. INCO, *The Chronology of Nickel*, 1969.

8. Benjamin, J.S., "Mechanical Alloying - History and Future Potential", in *Advances in Powder Metallurgy and Particulate Materials*, compiled by J.M. Capus and R.M. German, Metal Powder Industries Federation, Princeton, NJ, 1992, *7(Novel Powder Processing)*, 155.

9. INCO, *The Chronology of Nickel*, 1972.

10. Koch, C.C., Calvin, O.B., McKamey C.G., Scarbrough, J., "Preparation of amorphous Ni60Nb40 by mechanical alloying", *Journal of Applied Physics Letters*, **43**, 1983, 1017.

11. Koch, C.C., "Materials synthesis by mechanical alloying", *Annual Review of Materials Science*, **19**, 1989, 121.

12. Koch, C.C., Jang, J.S.C., Lee, P.Y., "Amorphization of Intermetallic Phases by Mechanical Alloying/Mechanical Milling", in *New Materials by Mechanical alloying Techniques*, ed. Artz, E., Shultz, L., Germany, 1989, 101.

13. Gaffet, E. Malhouroux, N. and Abdellaoui, M., "Far from equilibrium phase transition induced by solid-state reaction in the Fe-Si system", *Journal of Alloys and Compounds*, **194**(2), 1993, 339

14. Weeber, A.W., Bakker. H., "Amorphization by ball milling: a review", *Physica*, **B153**, 1988, 93.

15. Murty, B.S., Mohan Rao, M. and Ranganathan, S., "Milling maps and amorphization during mechaincal alloying", *Nanostructured Materials*, **3**, 1993, 459.

16. Koch, C.C., "Mechanical milling and alloying", in *Processing of metals and alloys, materials science and technology – a comprehensive treatment*, Ed., Cahn, R.W., **15**, 1991, 193, Weinheim, VCH.

17. Suryanarayana, C., *Bibiography on mechanical alloying and milling*, Cambridge, UK, Cambridge Interscience Publ., 1995.

18. Lü, L., Lai, M.O., *Mechanical Alloying*, Kluwer Academic Publishers, U.S.A., 1998.

19. Murty, B.S. and Ranganathan, S., "Novel materials synthesis by mechanical alloying/milling", *International Materials Reviews*, **43**(3), 1998, 101.

20. Shoji, K. and Austin, L.G., "A model for batch rod milling", *Powder Technology*, **10**, 1974, 29.

21. Abdellaoui, M., Rahouadj, R. and Gaffet, E., "The physics of mechanical alloying in a modified horizontal rod mill: mathematical treatment", *Materials Science forum*, **225-227**, 1996, 255.

22. Gilman, P.S., Benjamin, J.S., "Mechanical alloying", *Annual Review of Materials Science*, **13**, 1983, 279.

23. Maurice, D.R., Courtney, T.H., "The physics of mechanical alloying: a first report", *Metallurgical Transactions A.*, **21A**, 1990, 289.

24. Calka, A., Radlinski, A. P., "Universal high performance ball-milling device and its application for mechanical alloying", *Materials Science and Engineering*, **A134**, 1991, 1350.

25. ANI Grinding Mills, Technical Bulletin at "http://www.ani-mills.com.au/tech/images/3d-mill.jpg".

26. Pacific Ceramic Machinery & Equipment at "http://www.pacceram.com/photos/PC7342-1.JPG".

27. Zoz, H., "Attritor technology - latest developments", *Materials Science Forum*, **179-181**, 1995, 419.

28. Zoz, H., Ernst, D., Weiss, H., Magini, M. Powell, C., "Mechanical alloying of Ti-24Al-11Nb(at%) using the Simoloyer", *Metall,* **50**(9), 1996, 575.

29. Zoz, H., Ernst, D., Mizutani, T., Okouchi H., "Mechanical alloying using cycle operation - a new way to synthesize CMB-materials", *Metall,* **51**(10), 1997, 568.

30. Zoz, H., Ernst, D., Reichardt, R., Mizutani, T., Nishida, M., Okouchi H., "Energy balance during mechanical alloying, messurement and calculation method supported by the MALTOZ-software", *Metall,* **52**(9), 1998, 521.

31. Huang, H., Pan, J., McCormick, P.G., "Prediction of impact forces in a vibratory ball mill using an inverse technique", *International Journal of Impact Engineering* **19**(2), 1997, 117.

32. Benjamin, J.S., "New materials by mechanical alloying", DGM Confer., *Calw-Hirsau, Germany, Oct. 1988*, Ed. Arzt, E. and Schultz, L., Publ. Deutsche Gesellschaft Für Metallkunde eV., 1989, 3.

33. Koch, C.C. "The synthesis of non-equilibrium structures by ball milling", *Materials Science Forum*, **88-90**, 1992, 243.

34. Schultz, L., Schnitzke, K. and Wecker, J., "Preparation and properties of mechaincally alloyed rare earth permanent magnets", *Journal of Magnetism and Magnetic Materials*, **80**(1), 1989, 115.

35. Schultz, L., Wecker, J. and Hellstern, E., "Formation and properties of NdFeB prepared by mecahincal alloying", *Journal of Applied Physics*, **61**(8), 1987, 3583 .

36. Le Brun, P., Froyen, L. and Delaey, L., "The modelling of the mechanical alloying process in a planetary ball mill: comparison between theory and in-situ observations", *Materials Science Engineering*, **A157**, 1992, 79.

37. Niu, X.P., Le Brun, P., Froyen, L., Peytour, C. and Delaey, L., "High strength and high stiffness Al-Fe-Mn alloys fabricated by double mechiancal alloying", *Powder Metallurgy Internat.*, No. 3, 1993, 120.

38. Niu, X.P., Froyen, L., Delaey, L., Peytour, C., "Effect of Fe content on the mechanical alloying and mechanical properties of Al-Fe alloys", *Journal of Materials Science*, **29**, 1994, 3724.

39. Froyen, L., Delaey, L., Niu, X.P., Le Brun, P. and Peytour, "Synthesizing aluminum alloys by double mechanical alloying", *JOM*, **47**, 1995, 16.

40. Cairns, R.L. and Benjamin, J.S., "Stress rupture behavior of a dispersion strengthened superalloy", *Transactions of ASME, Journal of Engineering Materials and Technology*, **95**(1), 1973, 10.

41. Benjamin, J.S. Volin, T.E. and Weber, J.H., "Dispersoids in mechanically alloyed superalloys", *High Temperature–High Pressure*, **6**(4), 1974, 443.

42. Tripathi, K.C. and Groszek, A.J., "Effect of hydrocarbons on milling of aluminum powder", *Aluminium*, **49**(9), 1973, 612.

43. White, Richard L., "The use of mechanical alloying in the manufacture of multifilamentary superconductor wire", *Ph.D. Thesis*, Stanford University, 1979.

44. Yavari, A.R., and Desre, P.J., "Amorphization by mechanical alloying and by solid-state reaction similarities and differences", *Journal of Materials Science and Engineering*, **A134**, 1991, 1315.

45. Quan, M.X., Wang, K.Y., Shen, T.D., Wang, J.T., "Solid state amorphization transformations induced by mechanical alloying", *Journal of Alloys and Compounds*, **194**, 1993, 325.

46. Kim, M.S. and Koch, C.C., "Structural development during mechanical alloying of crystalline niobium and tin powders", *Journal of Applied Physics,* **62**, 1987, 2450.

47. Cho, Y.S. Koch, C.C., "Mechanical milling of ordered intermetallic compounds: The role of defects in amorphization",*Materials Science Engineering*, **A161**, 1993, 65.

48. Li, B., Liu, L., Ma, X.M. and Dong, Y.D., "Amorphization in the Nb-Si system by mechanical alloying", *Journal of Alloys and Compounds*, **202**, 1993, 161.

49. Pan, C.W., Hung, M.P. and Chang, Y.H., "Magnetic properties of mechanically alloyed Fe3Sn", *Materials Science and Engineering*, **A185**, 1994, 147.

50. Biswas, A., Dey, G.K., Haq, A. J., Bose, D.K. and Banerjee, S., "Study of solid-state amorphization in Zr-30 at.% Al by mechanical attrition", *Journal Materials Research*, **11**, 1996, 599.

51. Schwarz, R.B., Petrich, R.R., Saw, C.K., "The synthesis of amorphous Ni-Ti alloy powders by mechanical alloying", *Journal of Non-Crystalline Solids*, **76**, 1985, 281.

52. Weeber, A.W., Wester, A.J.H., Haag, W.J. and Bakker, H., "The preparation of amorphous Ni-Zr alloys by different ball milling techniques", *Physica B*, **145**, 1987, 349.

53. Murty, B.S., Ranganathan, S. and Mohan Rao, M., "Solid state amorphization in binary Ti-Ni, Ti-Cu and ternary Ti-Ni-Cu system by mechanical alloying", *Materials Science and Engineering*, **A149**, 1992, 231.

54. Politis, C., "Amorphous superconducting Nb_3Ge and $Nb_3Ge_{1-x}Al_x$ powders prepared by mechanical alloying", *Physica B*, **135**, 1985, 286.

55. Matsuki, K., Inoue, A., Kimura, M. and Masumoto, T., "New amorphous Cu-Nb-(Si, Ge or Sn) alloys prepared mechanical alloying of elemental powders", *Materials Science and Engineering*, **97**, 1988, 47.

56. Askeland, Donald R., *The Science and Engineering of Materials*, Third S.I. Edition, Chapman &Hall, 1996, 254.

57. Mizutani, U. and Lee, C.H., "Mechanical alloying in Cu-V and Cu-Ta systems characterized by positive heat of mixing (overview)", *Materials Transactions, JIM*, **36**(2), 1995, 210.

58. Wang, J.S.C., Donelly, S.G., Godavarti, P. and Koch, C.C., "Microstructures and mechanical behavior of mechanically alloyed nickel aluminides", *International Journal of Powder Metallurgy*, **24**, 1988, 315.

59. Koch, C.C., Kim, M.S., "The structure of amorphous alloys synthesized by mechanical alloying – non glass forming systems", *Journal Physique*, **46**, 1985, C3-573.

60. Ivanov, E., Konstanchuk, I., Stepanov, A., Boldyrev, V., "Magnesium mechanical alloys for hydrogen storage", *Journal of Less Common Metals*, **131**, 1987, 25.

61. Benn, R.C., Mirchandani, P.K., Watwe, A.S., "Intermetallic systems produced by mechanical alloying", in *Modern Developments in Powder Metallurgy*, 21, 1988, 479.

62. Koch, C.C., "Intermetallic matrix composites prepared by mechanical alloying – a review", *Materials Science and Engineering*, **244A**, 1998, 39.

63. Koch, C.C, Whittenberger, J.D., "Mechanical milling/alloying of intermetallics", *Intermetallics*, **4**, 1996, 369.

64. Fecht, H.J., Hellstern, E., Fu, Z., Johnson, W.L., "Nanocrystalline metals prepared by high-energy ball milling", *Metallurgical Transactions A*, **21A**, 1990, 2333.

65. Malow, T.R. and Koch, C.C, "Grain growth in nanocrystalline iron prepared by mechanical attrition", *Acta Materialia*, **45**, 1997, 2177.

66. Moelle, C. and Fecht, H.J., "Thermal stability of nanocrystalline iron prepared by mechanical attrition", *NanoStructured Matererials*, **6**, 1995, 421.

67. Xu, J., Yin, J.S. and Ma, E., "Nanocrystalline AG formed by low-temperature high-energy mechanical attrition", *NanoStructured Matererials*, **8**, 1997, 91.

68. Shen, T.D, Ge, W.Q., Wang, K.Y., Quan, M.X., Wang, J.T., Wei, W.D. and Koch, C.C., "Structural disorder and phase transformation in graphite produced by ball milling", *NanoStructured Materials*, **7**, 1996, 393.

69. Oehring, M. and Bormann, R., "Nanocrystalline alloys prepared by mechanical alloying and ball milling", *Materials Science and Engineering*, **A134**, 1991, 1330.

70. McDermott, B.I. and Koch, C.C., "Preparation of beta brass by mechanical alloying of elemental copper and zinc", *Scripta Metallurgica*, **20**, 1986, 669.

71. Provenzano, V. and Holtz, R.L., "Nanocomposites for high temperature applications", *Materials Science and Engineering*, **A204**, 1995, 125.

72. Zhu, M., Li, B.L., Gao, Y., Li, L., Luo, K.C., Sui, H.X. and Li, Z.X., "Microstructure characteristics of nanophase composite synthesized by mechanical alloying of immiscible Pb-Al and Fe-Cu systems", *Scripta Metallurgica et Materialia*, **36**, 1997, 447.

73. Du, Y., Li, S., Zhang, K. and Lu, K., "BN/Al composite formation by high-energy ball milling", *Scripta Metallurgica et Materialia*, **36**, 1997, 7.

74. Naser, J., Reinhemann, W. and Ferkel, H., "Dispersion hardening of metals by nanoscaled ceramic powders", *Materials Science and Engineering*, **A234**, 1997, 467.

75. Lü, L., Lai, M.O. and Zhang, S., "Thermodynamic properties of mechanically alloyed nickel and aluminum powders", *Journal of Materials Research Bulletin*, **29**, 1994, 889.

76. Eckert, J., Schultz, L., Urban, K., "Formation of quasicrystals by mechanical alloying", *Applied Physics Letters*, **55**, 1989, 117.

77. Eckert, Jurgen, Schultz, Ludwig, Urban, Knut, Z. "Progress of quasicrystals formation during mechanical alloying in Al-Cu-Mn and the influence of the milling intensity", *Metallkde*, **81**, 1990, 862.

78. Schaffer, G.B., McCormick, P.G., "On the kinetics of mechanical alloying", *Metallurgical Transactions A*, **23A**, 1992, 1285.

79. Kuschke, W.-M., Keller, R.-M., Grahle, P., Mason, R., Arzt, E., Z. "Mechanisms of powder milling investigated by X-ray diffraction and quantitative metallagraphy", *Metsllkde*. **86**, 1995, 804.

80. Aikin, B. J. M. , Courtney, T. H. , Maurice, D. R., "Reaction rates during mechanical alloying", *Materials Science and Engineering*, **A147**, 1991, 229.

81. Davis, R.M., Koch, C.C., "Mechanical alloying of brittle components: silicon and germanium", *Scripta Metallurgica*, **21**, 1987, 305.

82. Davis, R. M., McDermott, B. and Koch, C. C., "Mechanical alloying of brittle materials", *Metallurgical Transactions A*, 19A, 1988, 2867.

83. Lee, P.Y., Koch, C.C., "Formation of amorphous Ni-Zr alloy powder by mechanical alloying of intermetallic powder mixtures and mixtures of nickel or zirconium with intermetallics", *Journal of Materials Science*, **23**, 1988, 2837.

84. Murty, B.S., Joardar, J. and Pabi, S.K., "Influence of Fe and Cr on the disordering behavior of mechanically alloyed NiAl", *NanoStructured Materials*, **7**, 1996, 691.

85. Lim, W.Y., Hida, M., Sakakibara, A., Takemoto, T. Yokomizo, S., "Structural stability and mechanochemical activity of titanium nitride prepared by mechanical alloying", *Journal of Materials Science*, **28**(13), 1993, 3463.

86. Jang, J.S.C. and Koch, C.C, "Hall-Petch relationships in mechanically alloyed Ni3Al with oxide dispersoids", *Scripta Metallurgica*, **22**, 1988, 677.

87. Welham, N.J., "Mechanical activation of the formation of an alummia-titanium trialuminide composite", *Intermetallics*, **6**(5), 1998, 363.

88. Ovecoglu, M.L. and Nix, W.D., "Characterization of rapidly solidified and mechanically alloyed Al-Fe-Ce powders", *International Journal of Powder Metallurgy*, **22**, 1986, 17.

89. Wang, K.Y., Shen, T.D., Wang, J.T. and Quan, M.X., "Amorphization reaction during mechanical alloying: influence of the milling atmospheres", *Scripta Metallurgica et Materialia*, **25**, 1991, 2227.

90. Ivison, P.K., Cowlam, N., Soletta, L., Cocco, G. Enco, S. and Battezzati, L., "Influence of hydrogen contamination on the amorphization reaction of CuTi alloys", *Materials Science Engineering*, **A134**, 1991, 859.

91. Eckert, J., Schultz, L., Hellstern, E., "Glass-forming range in mechanically alloyed Ni-Zr and the influence of the milling intensity", *Journal of Applied Physics*, **64**(6), 1988, 3224.

92. Niu, X.P., "Processing and characterisation of mechanically alloyed aluminium for high temperature and wear resistance applications", *Processing and Characterization of Mechanical Alloyed Aluminium for High Temperature and Wear Resistance Applications, Ph.D. Thesis*, K.U.Leuven, Belgium, April 1994.

93. Lee, S.E., Ra, H.Y., Yim, T.H., Kim, W.T., "Phase transformation induced by ball milling in Fe-Zr system and related magnetic properties", *Materials Science Forum*, **179-181**, 1995, 121.

94. Eckert, J., "Milling induced phase transitions and quasicrystals formation in Al-Cu-Based alloys", *Materials Science Forum*, **88-90**, 1992, 679.

95. Harringa, J. L., Cook, B.A., Beaudry, B.J., "Effects of vial shape on the rate of mechanical alloying in Si80Ge20", *Journal of Materials Science*, **27**, 1992, 801.

96. Li, Mo and Johnson, William L., "Instability of metastable solid solutions and crystal to glass transition", *Physical Review Letters*, **70**(8), 1993, 1120.

97. Butyagin, P.Ju., "The chemical forces in mechanical alloying", *Materials Science Forum*, **88-90**, 1992, 695.

98. Ma, E., Atzmon, M., "Phase transformations induced by mechanical alloying in binary systems (review)", *Materials Chemistry & Physics,* **39**(4), 1995, 249.

99. Najafabadi, R., Srolovitz, D.J., MA, E. and Atzmon, M., "Thermodynamic properties of metastable Ag-Cu alloys", *Journal of Applied Physics*, **74**(5), 1993, 3144.

100. Badmos, A.Y. and Bhadeshia, H.K.D.H., "The evolution of solutions – a thermodynamic analysis of mechanical alloying", M*etallurgical and Materials Transactions A*, **28A**, 1997, 2189.

101. Desré, P.J. and Yavari, A.R., "Suppression of crystal nucleation in amorphous layers with sharp concentration gradients", *Physical Review Letters*, **64**(13), 1533.

102. Yavari, A.R. and Desré, P.J., "Thermodynamic and kinetic justification for amorphization by mechanical alloying of A-B metal couples with zero heat of mixing ΔHmix", *Physical Review Letters*, **65**(20), 2571.

103. Gösele, U. and Tu, K.N., "Critical thickness of amorphous phase formation in binary diffusion couples", *Journal of Applied Physics*, **66**(6), 1989, 2619.

104. Ma, E. and Atzmon, M., "Calorimetric Evidence for Polymorphous Constraints on Metastable Zr-Al Phase Formation by Mechanical Alloying", *Physical Review Letters*, **67**(9), 1991, 1126.

105. Schwarz, R.B., "Microscopic model for mechanical alloying", *Materials Science Forum*, **269-272**, 1998, 665.

106. Kousaka, Y., Maki, N. and Yoshida, T., "Vertical motion of a non-repulsive body and a bed composed of repulsive bodies in vibrating field – fundamental study on grinding mechanicsm of vibration mill", *Kagaku Kogaku*, 37, 1973, 180.

107. Inoue, T., "A trial computer simulation of the movement of balls in the vibration mills.", *Funsai (Micromeritics)*, **18**, 1973, 50.

108. Maurice, D, Courtney, T. H., "Modelling of mechanical alloying: part I. deformation, coalescence and fragmentation mechanisms", *Metallurgical Transactions A*, **25A**, 1994, 147.

109. Maurice, D, Courtney, T. H., "Modelling of mechanical alloying: part II. development of computational modeling programs", *Metallurgical and materials Transactions A*, **26A**, 1995, 2431.

110. Maurice, D, Courtney, T. H., "Modelling of mechanical alloying: part III. applications of computational programs", *Metallurgical and materials Transactions A*, **26A**, 1995, 2437.

111. Maurice, D, Courtney, T. H., "Milling dynamics: part II, dynamics of a SPEX mill and a one-dimensional mill", *Metallurgical and materials Transactions A*, **27A**, 1996, 1973.

112. Maurice, David R., "The physics of mechanical alloying : a first report", *MSc Thesis*, University of Virginia, 1988.

113 . Maurice, David., "Local modeling of mechanical alloying", *PhD Thesis*, University of Virginia, 1992.

114. Courtney, T. H. and Maurice, D.R., "Some fundamental physics of the mechanical alloying process", in "*Solid State Powder Processing*", Edited by A.H. Clauer and J.J. deBarbadillo, TMS, 1990, 2.

115. Courtney, T. H. and Maurice, D., "Process modeling of the mechanics of mechanical alloying", *Scripta Materialia*, **34**(1), 1996, 5.

116. Maurice, D, Courtney, T. H., "Modelling of the mechanical alloying process", *Journal of Metals*, **44**(8), 1992, 10.

117. Aikin, B. J. M., Courtney, T. H., "The kinetics of composite particle formation during mechanical alloying", *Metallurgical Transactions A*, **24A**, 1993, 647.

118. Rydin, R. W., Maurice, D. and Courtney, T. H, "Milling dynamics: part I. attritor dynamics: results of a cinematographic study", *Metallurgical Transactions A*, **24**, 1993, 175.

119. Maurice, D, Courtney, T. H., "Milling dynamics: part III, integration of local and global modeling of mechanical alloying devices", *Metallurgical and materials Transactions A*, **27A**, 1996, 1981.

120. Rahouadj, R. and Gaffet, E., "Shock transfer in ball-milling: nanocomposite mechanical approach", *Materials Science forum*, **225-227**, 1996, 249.

121. Abdellaoui, and Gaffet, E., "Mechanical alloying in a planetary ball mill: kinematic description", *Journal De Physique IV, Colloque C3, supplement au Journal de Physiuque III*, **4**, 1994, C3-291.

122. Abdellaoui, and Gaffet, E., "The physics of mechanical alloying in a planetary ball mill: mathematical treatment", *Acta Metallurgica et Materialia*, **43**(3), 1995, 1087.

123. Abdellaoui, and Gaffet, E., "The physics of mechanical alloying in a modified horizontal rod mill: mathematical treatment", *Acta Metallurgica et Materialia*, **44**(2), 1996, 725.

124. Hashimoto, Hitoshi and Watanabe, Ryuzo, "Model simulation of energy consumption during vibratory ball milling of metal powder", *Materials Transactions, JIM*, **31**(3), 1990, 219.

125. Hashimoto, H. and Watanabe, R., "Model simulation of vibratory ball milling of metal powder", *Materials Science Forum*, **88-90**, 1992, 89.

126. Hashimoto, Hitoshi., Lee, Gil Geun and Watanabe, Ryuzo, "Simulation of ball motion for analysis of coating phenomena during tumbler-ball milling of Cu powder", *Materials Transactions, JIM.*, **35**(1), 1994, 40.

127. Hashimoto, Hitoshi. and Abe, Toshihiko, "Three-dimensional model simulation of ball motion in a tumbling ball mill", *Journal of the Japan Society of Powder and Powder Metallurgy*, **45**(10), 1998, 986.

128. Watanabe, R.,. Hashimoto, H.,. Lee, G.G.. "Computer simulation of milling ball motion in mechanical alloying", *Materials Transactions, JIM,* **36**(2), 1995, 102.

129. Watanabe, Hiroshi, "Critical rotation speed for ball-milling", *Powder Technology*, **104**, 1999, 95.

130. McCormick, P. G., Huang, H., Dallimore, M. P., Ding, J. and Pan, J., "The dynamics of mechanical alloying", *Proceedings of the 2nd International Conference on Structural Applications of Mechanical Alloying*, Vancouver, British Columbia, Canada, 1993, 45.

131. Huang, Han, Pan, Jie and McCormick, Paul G., "An Investigation of Chaotic Phenomena in a Vibratory Ball Milling System", *Complexity International*, **2**, 1995.

132. Dallimore, M.P. and McCormick, P.G., "Dynamics of planetary ball milling: A comparison of computer simulated processing parameters with CuO/Ni displacement reaction milling kinetics", *Materials Transactions, JIM*, **37**(5), 1996, 1091.

133. Dallimore, M.P. and McCormick, P.G., "Distinct element modelling of mechanical alloying in a planetary ball mill", *Materials Science Forum*, **235**, 1997, 5.

134. Huang, H., Dallimore, M.P., Pan, J., McCormick, P.G., "An investigation of the effect of powder on the impact characteristics between a ball and a plate using free falling experiments", *Materials Science and Engineering A*, **241**, 1998, 38.

135. Agrawala, S. Rajamani, R.K., Songfack, P. and Mishra, B.K., "Mechanics of media motion in tumbling mills with 3D discrete element method", *Minerals Engineering*, **10**(2), 1997, 215.

136. Babich, B.N., Djatlenko, V.A., "A mathematical model for the process of mechanical alloying", in *Proceedings of an ASM International Conference: Structural Applications of Mechanical Alloying*, Myrtle Beach, South Carolina, 27-29 March 1990, Edited by Froes, F.H. and deBarbadillo, J.J., 287.

137. Bhattacharya, A.K. and Arzt, E., "Plastic deformation and its influence on diffusion process during mechanical alloying", *Scripta Metallurgica et Materialia*, **28**, 1993, 395.

138. Burgio, N., Iasonna, A., Magini, M., Martelli, S. and Padella, F., "Mechanical alloying of the Fe-Zr system. Correlation between input energy and end products", *IL Nuovo Cimento*, **13D**(4), 1991, 459.

139. Caravati, C., Delogu, F., Cocco, G. and Rustici, M., "Hyperchaotic qualities of the ball motion in a ball milling device", *Chaos*, **9**(1), 1999, 219-226.

140. Gavrilov, Dmitri, Vinogradov, Oleg, and Shaw, William, J.D., "Computer simulation of mechanical alloying in shaker ball mill", *Proceedings of ICCM-10*, Whistler, B.C., Canada, Aug. 1995, III-11.

141. Gavrilov, Dmitri, Vinogradov, Oleg, and Shaw, William, J.D., "Simulation of grinding in a shaker ball mill", *Powder Technology*, **101**, 1999, 63.

142. Goodson, Rodney, Larson, Floyd and Sheehan, Lawrence, "Energy input monitoring during attritor milling", in *Advances in hard metal production, 1983 Nov. Lucerne, Switzerland*, Vol. 2, Shrewsbury MPR Publishing Services Ltd, 1983, 4-1.

143. Inoue, Toshio and Okaya, Katsunori, "Grinding mechanism of centrifugal mills – a simulation study based on the discrete element method", *International Journal of Mineral Processing*, **44-45**, 1996, 425.

144. Kheifets, A.S., Lin, I.J., "Energetic approach to kinetics of batch ball milling", *International Journal of Mineral Process*, **54**, 1998, 81.

145. Le Brun, P., Froyen, L. and Delaey, L., "The modelling of the mechanical alloying process in a planetary ball mill: comparison between theory and in-situ observations", *Materials Science and Engineering A*, **161**, 1993, 75.

146. Lira, B.B. and Kavetsky, A.," Applications of a new model-based method of ball mill simulation and design", *Minerals Engineering*, **3**(12), 1990, 149-163.

147. Lü, L., Lai, M.O., Zhang, S., "Modeling of mechanical alloying process", *Journal of Materials Processing Technology*, **52**, 1995, 539.

148. Park, Y.H., Jeong, H.Y., Lee, B.W, Kim, S.K, Kim, W.Y. and Bae, C.H., "An analysis of mechanical alloying process of vibratory ball milling by model simulation", *Journal of the Korean Institute of Metals and Materials*, **34**(7), 1996, 896.

149. Schilz, Jürgen, "Internal kinematics of tumbler and planetary ball mills: a mathematical model for the parameter setting", *Materials Transactions, JIM*, **39**(11), 1998, 1152.

150. Yang, Junyou; Wu, Jiansheng; Zeng, Zhenpeng, "Investigation on the deformation and energy transfer of powders during mechanical alloying (Chinese)", *Acta Metallurgica Sinica*, **34**(10), 1998, 1061.

151. Lazarev, A. S., Kolesnikov, A. A. And Koral, V. A., "Mass and energy transfer during the mechanical alloying of powders in an attritor", *Soviet Powder Metallurgy & Metal Ceramics*, **25**(8), 1987, 613.

152. Aikin, Beverly Jean Myers, "The kinetics of fracture and welding during mechanical alloying", *PhD Thesis*, University of Virginia, 1992.

153. Huang, Han, "The dynamics of mechanical milling", *PhD Thesis*, University of Western Australia, 1995.

154. Dallimore, Michael Paul, "Distinct element method modelling of a planetary ball mill", *PhD Thesis*, University of Western Australia, 1998.

155. Zoz, H., Ernst, D., Reichardt, R., Mizutani, T., Nishida, M., Okouchi, H., "Energy balance during mechanical alloying, messurement and calculation method supported by the MALTOZ-software", in *Process. Fabr. Adv. Mater. VII, Proc. Symp., 7th*, 1998, 279, Edited by: Srivatsan, T.S., Khor, K.A.

156. Schwarz, Ricardo B. and Koch, Carl C., "Formation of amorphous alloys by the mechanical alloying of crystalline powders of pure metals and powders of intermetallics", *Applied Physics Letters*, **49**(3), 1986, 146.

157. Mishra, Barada Kanta, "Study of media mechanics in tumbling mills by the discrete element method", *PhD Thesis*, University of Utah, 1991.

158. Mishra, B.K.. Rajamai, R.K., "Simulation of charge motion in ball mills. part 2: numerical simulations", *International Journal of Mineral Processing*, **40**(3-4), 1994, 187.

159. Timoshenko, S.P. and Goodier, J.N., *Theory of Elasticity*, 3rd Ed., McGraw-Hill, New York, 1970, 409.

160. Johnson, K.L., *Contact Mechanics*, Cambridge, 1985, 342.

161. Andrews, J.P., "Theory of collision of spheres of soft metals", *Philosophical Magazine S7*, **9**(58), 1930, 593.

162. Maw, N. Barber, J.R. and Fawcett, J.N., "The oblique impact of elastic spheres", *Wear*, **38**, 1976, 101.

163. Felbeck, David K. and Atkins, Anthony G., *Strength and Fracture of Engineering Solids*, Englewood Cliffs, NJ, Prentice-Hall, 1984, 255.

164. Carroll, M.M. and Holt, A.C., "Static and dynamic pore-collapse relations for ductile porous materials", *Journal of Applied Physics*, **43**(4), 1972, 1626.

165. Bay, N., "Cold pressure welding – the mechanisms governing bonding", *Transactions of the American Society of Mechanical Engineers*, 101, 1979, 121.

166. Bay, N., "Mechanisms producing metallic bonds in cold welding", *Welding Research Supplement*, May, 1983, 137s.

167. Bay, N., "Cold welding Part 1 characteristics, bonding mechanisms, bond strength", *Metal Construction*, **18**(6), 1986, 369.

168. Carslaw, H.S. and Jaeger, J.C., *Conduction of heat in solids*, Oxford, London, 1959.

169. Streeter, V.L., *Fluid Mechanics*, McGraw-Hill, New York, 1951, 25.

170. Joisel, A., "Broyeurs a satellites", *Revue des Materiaux de Construction et de Travaux Publics*, No. 493, 1956, 1

Chapter Three

Model for Single Head-on Impact

3.1 Introduction

Introduced in this chapter is a basic model to simulate the head-on impact process with a powder compact trapped in between. The elastic deformation of balls, and the elastic and plastic deformation and viscous flow of powder compact are considered. The validation and some simulation results are presented in the last section.

3.2 Description of an Impact Process

During ball milling process, impacts occur between balls or between a ball and wall with a powder compact being entrapped between them as shown schematically in Figure 3-1. The balls and vial wall are considered as tools.

Impact is a progressive process. It starts from the point at which the ball-powder-ball (or wall) contact is established. The impact further develops as the relative velocity between the tools decreases and the force applied onto the powder increases. As a result of this, the powder as well as the tools is deformed. The deformation includes elastic deformation of the tools, elastic and plastic deformation of the powder, and viscous flow of the powder, as shown schematically in Figure 3-2. Eventually the impact will reach the critical moment when the impact velocity of tools is zero. After

that, the tools and the powder compact start to recover their elastic deformation (as shown in Figure 3-2) and the tools accelerate in opposite directions until the contact breaks.

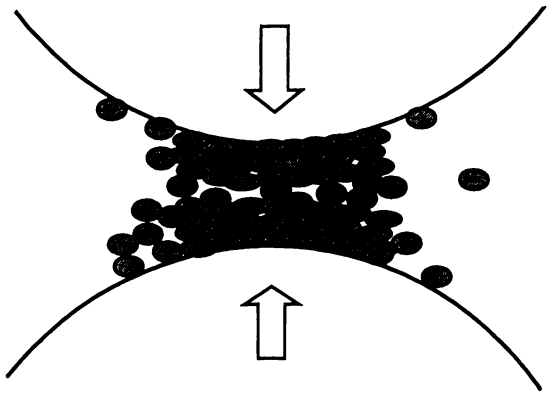

Figure 3-1. Schematic diagram showing an impact process of balls on a mini powder compact

3.3 Assumptions

In order to facilitate the construction of the mathematical model, the following assumptions have been made:

- Tools are hard enough to prevent any plastic deformation in them.
- For the impact between a ball and the wall of the vial, the wall is assumed to be a ball with a much larger diameter.
- Since the dimension of balls is far bigger than the contact area, the ball surface is

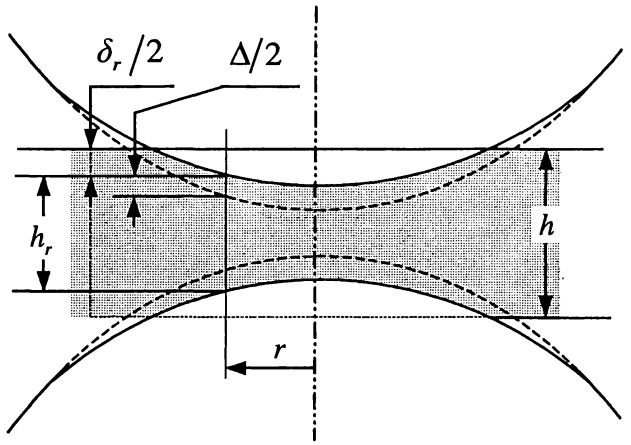

Figure 3-2. Deformation of balls during impact of tools

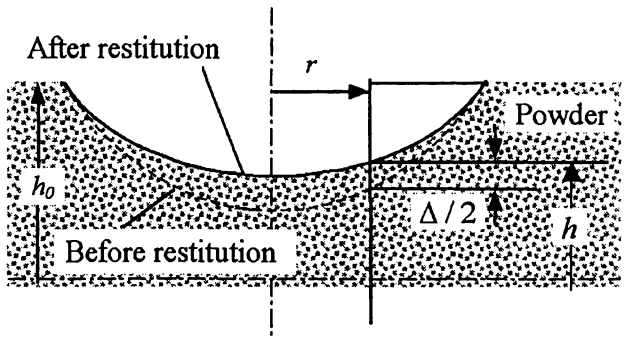

Figure 3-3. Powder Restitution

assumed to be flat in deducing the model for ball elastic deformation.

- In deducing the powder model for powder flow, it is assumed that the instantaneous changes in volume and dimension of the powder compact are negligible.
- The elastic deformation of tools and powder compact is fully recovered when the ball-powder contact breaks.

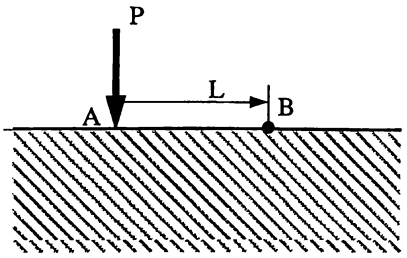

Figure 3-4. The concentrated force acted on a flat surface

3.4 The Deformation of Tools

To simulate the deformation of tools, Hertz's theory [1] is employed. As shown schematically in Figure 3-4, when a concentrated force, P, is applied at point A on a flat surface, point B will sink. The displacement of B in vertical direction, ζ, can be expressed using the following equation [1].

$$\zeta = \frac{1-\nu^2}{\pi E}\frac{P}{L} \qquad (3\text{-}1)$$

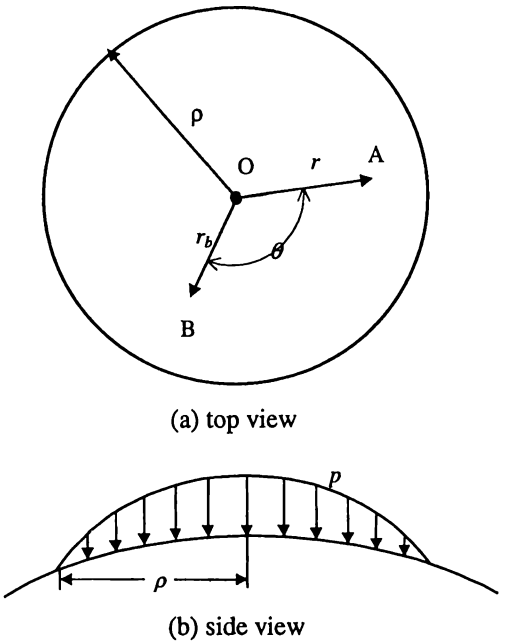

Figure 3-5. Schematic diagram of the contacting area

where L is the distance between point A and point B, E is Young's

modulus of elasticity and v is Poisson's ratio.

Equation (3-1) can be modified slightly to use the distance from point A and point B to the centre, r and r_b, and the angle between OA and OB, θ, to replace L (as shown in Figure 3-5a). Then we have

$$\zeta = \frac{(1-\upsilon^2)}{E} \frac{P}{\sqrt{(r_b + r\cos\theta)^2 + (r\sin\theta)^2}} \tag{3-2}$$

During impact, a pressure, p, acting on the contact area, which has a radius of ρ, varies at different points, as shown in Figure 3-5b. This pressure can be viewed as a series of concentrated forces. Then the displacement at any position in the contact area, Δ, caused by those concentrated forces can be calculated by integrating equation (3-2) in the area. This displacement is

$$\Delta = \frac{(1-\upsilon^2)}{\pi E} \int_0^{2\pi} \int_0^{\rho} \frac{p}{\sqrt{(r_b + r\cos\theta)^2 + (r\sin\theta)^2}} r dr d\theta \tag{3-3}$$

where r_b and θ determine the position of interest and p can be calculated by using equation (3-22).

3.5 Powder Flow

When a powder compact is pressed, its deformation can be seperated into two parts: elastic deformation and visco-plastic deformation. The second part can be viewed as a kind of powder flow, which is going to be discussed in detail in the following.

To describe the impact process, a cylindrical co-ordinate system is used as shown in Figure 3-6. Since the tools have the same curvature and the powder is homogeneous, the tool-powder-tool system is symmetrical with respect to both the z axis and the middle plane of the powder compact. Thus it is only nessessary to consider the top half of the system. During impact, the powder flows in both r and z directions, but not in θ direction. The flow rate in r direction within the powder compact, v_r, is described using the following equation.

$$v_r = A(r)\frac{v}{h}e^{-2bz/h} \tag{3-4}$$

where $A(r)$ is a function of r, b is a coefficient, v is the relative velocity between tools and h is the thickness of powder compact at distance, r, away from the centre.

Since the tool-powder-tool system is symmetrical to z axis, equation (3-4) satisfies the following boundary condition.

$$v_r = 0 \text{ when } r = 0 \tag{3-5}$$

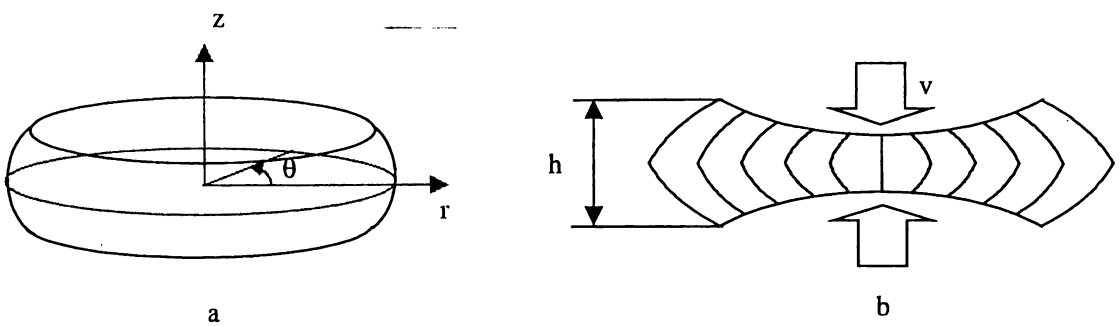

Figure 3-6. Cylindrical co-ordinate system to express powder flow when two balls of same size impact with a powder compact in between

From equation (3-4) the strain rate in r and θ directions, $\dot{\varepsilon}_r$ and $\dot{\varepsilon}_\theta$ respectively, can be calculated using the following equations.

$$\dot{\varepsilon}_r = \frac{\partial v_r}{\partial r} = \frac{dA(r)}{dr}\frac{v}{h}e^{-2bz/h} \tag{3-6}$$

$$\dot{\varepsilon}_\theta = \frac{v_r}{r} + \frac{\partial v_\theta}{r\partial\theta} = \frac{A(r)}{r}\frac{v}{h}e^{-2bz/h} \tag{3-7}$$

Based on the assumption that the volume of the powder compact remains unchanged for a very short time, the strain rate in z direction, $\dot{\varepsilon}_z$, can be related to $\dot{\varepsilon}_r$ and $\dot{\varepsilon}_\theta$ as follows:

$$\dot{\varepsilon}_z = -\dot{\varepsilon}_r - \dot{\varepsilon}_\theta = -\left[\frac{dA(r)}{dr} + \frac{A(r)}{r}\right]\frac{v}{h}e^{-2bz/h} \tag{3-8}$$

Since $\dot{\varepsilon}_z = \frac{\partial v_z}{\partial z}$, then from equation (3-8), we have

$$v_z = \int \dot{\varepsilon}_z dz = -\left[\frac{dA(r)}{dr} + \frac{A(r)}{r}\right]\frac{v}{h}\int e^{-2bz/h}dz = \left[\frac{dA(r)}{dr} + \frac{A(r)}{r}\right]\left[\frac{v}{2b}e^{-2bz/h} + f(r,\theta)\right] \tag{3-9}$$

As the powder compact is symmetrical to its middle plane and the flow rate at the top surface in z direction is the same as that of the tool. We have the following boundary conditions for equation (3-9).

$$v_z = 0 \text{ when } z = 0 \tag{3-10a}$$

$$v_z = -v \text{ when } z = \frac{h_0}{2} + \sqrt{R^2 - \rho^2} - \sqrt{R^2 - r^2} \tag{3-10b}$$

where h_0 is the maximum thickness of powder compact and ρ is the radius of contact area.

By substituting equations (3-10a) and (3-10b) into equation (3-9) respectively, we have

$$\left[\frac{dA(r)}{dr} + \frac{A(r)}{r}\right]\left[\frac{v}{2b} + f(r,\theta)\right] = 0 \tag{3-11a}$$

$$\left[\frac{dA(r)}{dr} + \frac{A(r)}{r}\right]\left[\frac{v}{2b} e^{-\frac{b}{h}\left(h_0 + 2\sqrt{R^2-\rho^2} - 2\sqrt{R^2-r^2}\right)} + f(r,\theta)\right] = -v \tag{3-11b}$$

By combining equations (3-5) and (3-4), we have

$$\left[A(r)\frac{v}{h}e^{-b}\right]_{r=0} = 0 \tag{3-11c}$$

Since $e^{-b} \neq 0$, $\frac{v}{h} \neq 0$, we have

$$[A(r)]_{r=0} = 0 \tag{3-11d}$$

The $A(r)$ function needs to satisfy the boundary condition defined by (3-11d).

Since $R >> r$, it is reasonable to assume that $\sqrt{R^2 - r^2}$ does not change with r. Then from equations (3-11a) and (3-11b), the functions for $A(r)$ and $f(r,\theta)$ can be obtained in the following equations:

$$f(r,\theta) = -\frac{v}{2b} \tag{3-12a}$$

$$A(r) = \frac{br}{1-\Theta} \tag{3-12b}$$

where, $\Theta = e^{-\frac{b}{h}\left(h_0+2\sqrt{R^2-\rho^2}-2\sqrt{R^2-r^2}\right)}$

It is evident that $[A(r)]_{r=0} = 0$, so the $A(r)$ function defined by (3-12b) satisfies the boundary condition defined by (3-11d).

Now the velocity field can be expressed by the following equations.

$$v_z = -\frac{1-e^{-2bz/h}}{1-\Theta}v \tag{3-13a}$$

$$v_r = \frac{rbe^{-2bz/h}}{h(1-\Theta)}v \tag{3-13b}$$

$$v_\theta = 0 \tag{3-13c}$$

and strain rate field can be expressed as:

$$\dot{\varepsilon}_z = \frac{\partial v_z}{\partial z} = \frac{-2be^{-2bz/h}}{h(1-\Theta)}v \tag{3-14a}$$

$$\dot{\varepsilon}_r = \frac{\partial v_r}{\partial r} = \frac{be^{-2bz/h}}{h(1-\Theta)}v \tag{3-14b}$$

$$\dot{\varepsilon}_\theta = \frac{v_r}{r} + \frac{\partial v_\theta}{r\partial\theta} = \frac{be^{-2bz/h}}{h(1-\Theta)}v \tag{3-14c}$$

$$\dot{\varepsilon}_{z\theta} = \dot{\varepsilon}_{\theta z} = \frac{1}{2}\left(\frac{\partial v_\theta}{\partial z} + \frac{\partial v_z}{r\partial\theta}\right) = 0 \tag{3-14d}$$

$$\dot{\varepsilon}_{r\theta} = \dot{\varepsilon}_{\theta r} = \frac{1}{2}\left(\frac{\partial v_\theta}{\partial r} + \frac{\partial v_r}{r\partial\theta} - \frac{v_\theta}{r}\right) = 0 \tag{3-14e}$$

$$\dot{\varepsilon}_{zr} = \dot{\varepsilon}_{rz} = \frac{1}{2}\left(\frac{\partial v_r}{\partial z} + \frac{\partial v_z}{\partial r}\right) = \frac{rb^2e^{-2bz/h}}{h^2(1-\Theta)}v \tag{3-14f}$$

From above, the equivalent strain rate can be expressed by [2]

$$\dot{\varepsilon}_e = \sqrt{\frac{2}{3}}\sqrt{\left(\dot{\varepsilon}_r{}^2 + \dot{\varepsilon}_\theta{}^2 + \dot{\varepsilon}_z{}^2\right) + 2\left(\dot{\varepsilon}_{r\theta}{}^2 + \dot{\varepsilon}_{\theta z}{}^2 + \dot{\varepsilon}_{zr}{}^2\right)} \tag{3-15}$$

If considering that all the work is used in the visco-plastic flow, the virtual work rate can be expressed by [2,3]

$$\dot{W}_v = \int_v \sigma_s \dot{\varepsilon}_e dV \tag{3-16}$$

where σ_s is stress due to visco-plastic flow within the powder compact. To simplify the deduction process, it is assumed that σ_s is a constant. Thus we have

$$\dot{W}_v = \sigma_s \frac{2}{\sqrt{3}} \int_v \left[\sqrt{3 + \left(\frac{rb}{h}\right)^2}\, \frac{be^{-2bz/h}}{h(1-\Theta)}v\right] dV$$

$$= \frac{4}{\sqrt{3}} \frac{bv\pi\sigma_s}{h} \int_0^{\rho} \left\{ \sqrt{3 + \left(\frac{rb}{h}\right)^2} \int_0^{\frac{h}{2}+\sqrt{R^2-\rho^2}-\sqrt{R^2-r^2}} \left[\frac{e^{-2bz/h}}{1-\Theta} \right] dz \right\} rdr$$

$$= \frac{2}{\sqrt{3}} \pi\sigma_s v \frac{h^2}{3b^2} \left[\left(\frac{b^2\rho^2}{h^2} + 3 \right)^{3/2} - 3^{3/2} \right] \tag{3-17}$$

The coefficient b must satisfy the requirement that the virtual work rate is the minimum. That is

$$\frac{d\dot{W}_v}{db} = 0 \tag{3-18}$$

Solving equation (3-17) and (3-18) we have

$$b = \frac{3h}{\rho} \tag{3-19}$$

Then the above strain rate field in equation (3-14) can be determined in the following equation.

$$\dot{\varepsilon}_z = -\frac{6e^{-6z/\rho}}{\rho\left[1 - e^{-\frac{b}{h}\left(h_0 + 2\sqrt{R^2-\rho^2} - 2\sqrt{R^2-r^2}\right)}\right]} v \tag{3-20a}$$

$$\dot{\varepsilon}_r = \frac{3e^{-6z/\rho}}{\rho\left[1 - e^{-\frac{b}{h}\left(h_0 + 2\sqrt{R^2-\rho^2} - 2\sqrt{R^2-r^2}\right)}\right]} v \tag{3-20b}$$

$$\dot{\varepsilon}_{\theta} = \frac{3e^{-6z/\rho}}{\rho\left[1-e^{-\frac{b}{h}\left(h_0+2\sqrt{R^2-\rho^2}-2\sqrt{R^2-r^2}\right)}\right]}v \tag{3-20c}$$

$$\dot{\varepsilon}_{z\theta} = \dot{\varepsilon}_{\theta z} = 0 \tag{3-20d}$$

$$\dot{\varepsilon}_{r\theta} = \dot{\varepsilon}_{\theta r} = 0 \tag{3-20e}$$

$$\dot{\varepsilon}_{zr} = \dot{\varepsilon}_{rz} = \frac{9re^{-6z/\rho}}{\rho^2\left[1-e^{-\frac{b}{h}\left(h_0+2\sqrt{R^2-\rho^2}-2\sqrt{R^2-r^2}\right)}\right]}v \tag{3-20f}$$

In the case where two impacting tools have different radii, R_1 and R_2, R in equations (3-20a)~(3-20f) is replaced by an equivalent radius R_e, which is related to R_1 and R_2 through the following equation.

$$\frac{2}{R_e} = \frac{1}{R_1} + \frac{1}{R_2} \tag{3-21}$$

Equation (3-21) is derived by taking the following consideration:

When $R_1 \neq R_2$, the mid-plane plane, $rO\theta$ (as shown in Figure 3-7a) is bent as shown in Figure 3-7b. In order to have a flat mid-plane $rO\theta$, the powder compact is arbitrarily straightened. Then the curvatures of the top and bottom surfaces are the same, which is $\frac{1}{R_e}$, as shown in Figure 3-7c. Based on geometric relationship (refer to Appendix I), we have equation (3-21).

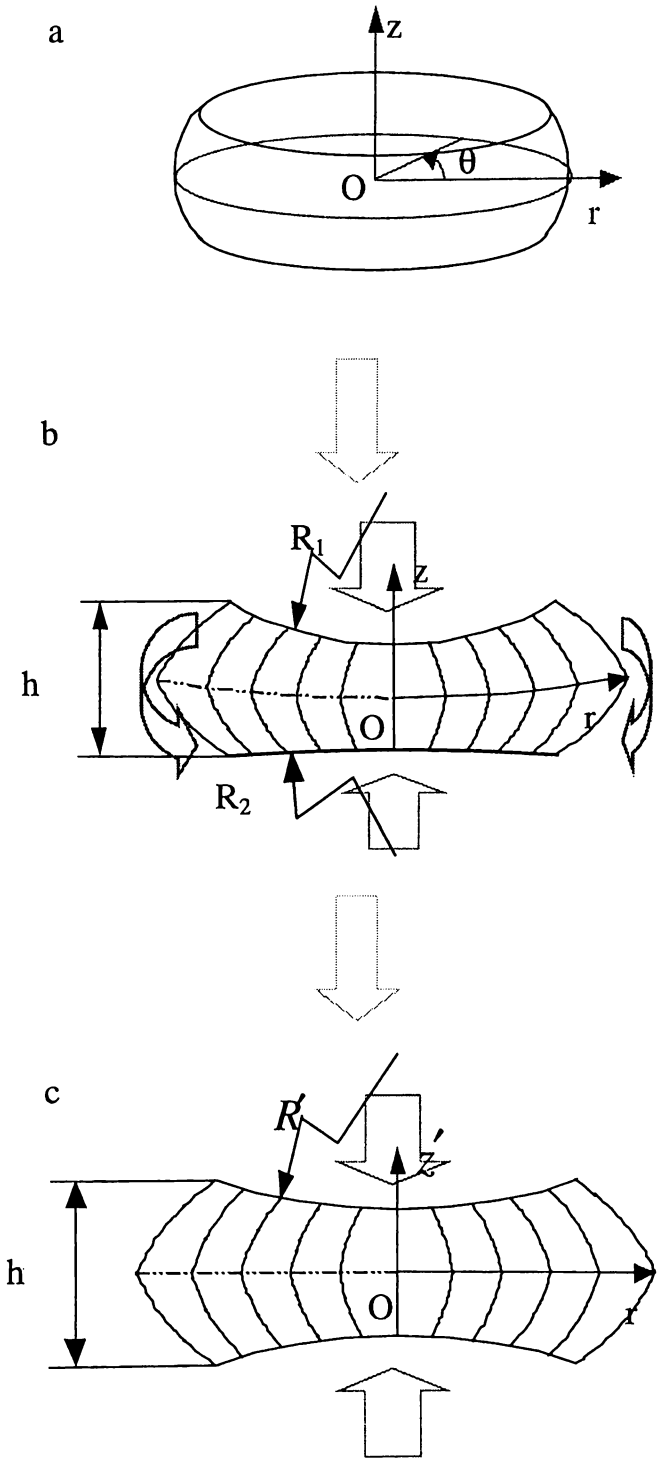

Figure 3-7. The process to get the equivalent radius R_e

3.6 Impact Force and Pressure

The pressure during the impact (p) can be separated into two components (as shown in Figure 3-8): one (p^e) caused by elastic deformation and the other (p^{vp}) is caused by internal resisting force of visco-plastic flow of powder. At time t, the contact pressure p at a distance, r, away from the central axis can be expressed by

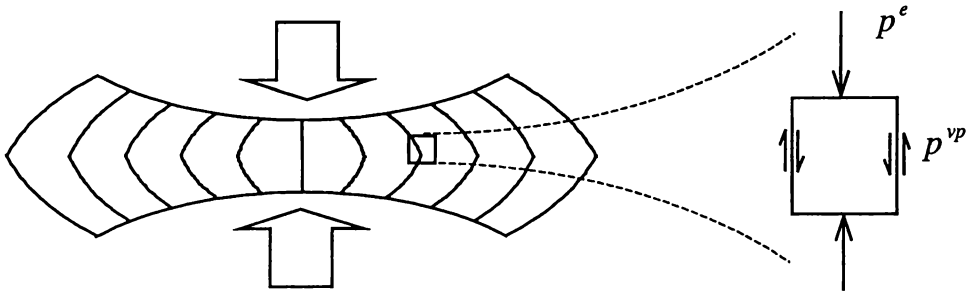

Figure 3-8. Two components of impact pressure

$$p = p^e + p^{vp} \tag{3-22}$$

p^e is related to the elastic strain in z direction, ε_z^e, according to the Hooke's law:

$$p^e = k_e \varepsilon_z^e \tag{3-23}$$

where k_e is elastic coefficient and will be determined in Section 3.10.

p^{vp} is used to simulate the work-hardening, which is strain rate sensitive. In high-

energy ball milling, powder deformation occurs at a high strain rate (over 1000/s), so the strain rate is the dominating factor, which controls the work hardening. Therefore p^{vp} is calculated by relating it to the visco-plastic shear strain rate in z direction, $\dot{\varepsilon}_{zr}$, through the following equation.

$$p^{vp} = 2\mu\dot{\varepsilon}_{zr} \tag{3-24}$$

where μ is strain rate coefficient which measures the strain rate sensitivity of work hardening component. $\dot{\varepsilon}_{zr}$ can be determined by equations (3-14f) and (3-19).

μ is equivalent to the viscosity of the powder compact and is proportional to the density of the powder compact. Of course, the density increase has its limit. μ can be assumed to be proportional to the flow shear stress of the powder compact, τ_s when $\tau_s < \frac{\sigma_s}{\sqrt{3}}$, where σ_s is the normal yield strength and $\frac{\sigma_s}{\sqrt{3}}$ is the apparently shear stress at yielding point [2]. Then we have

$$\mu = c_1\tau_s \tag{3-25}$$

where c_1 is constant. τ_s is related to the impact force F, the height and diameter of powder compact, h and ρ at time t through the following equation.

$$\tau_s = -\frac{F}{\pi\rho^2\left(\sqrt{3}+\frac{2\rho}{3h}\right)} \tag{3-27}$$

Equation (3-27) is derived in Section 3.9.

When $\tau_s \geq \frac{\sigma_s}{\sqrt{3}}$, the powder compact would yield by plastic deformation [2]. In this case, μ is assumed unchanged with deformation and can be calculated using the following equation.

$$\mu = c_1 \frac{\sigma_s}{\sqrt{3}} \tag{3-27}$$

The impact force, *F*, can be calculated by

$$F = \int_0^{2\pi} \int_0^{\rho} p \, r dr d\theta \tag{3-28}$$

3.7 Elastic Strain ε_z^e

During impact, the amount of elastic deformation of the powder compact keeps increasing until the impact tools start to bounce back and the deformation starts to recover its elastic component. Since the powder flows visco-plastically during impact, the pressure inside the powder compact increases with increasing the force caused by visco-plastic flow. This pressure in turns also causes the elastic deformation insider the powder compact to increase. Therefore it was assumed that the increase of the elastic deformation is propotional to the increase of the pressure caused by visco-plastic flow. In the meantime, the instantaneous approach of tools, $d\delta_z$, at a distance, *r*, away from the central axis is assumed to be proportional to the total pressure at the same point. From the above consideration, we have

$$\frac{d\delta_z^e}{d\delta_z} = k' \frac{p^{vp}}{p} \tag{3-29}$$

where k' is a coefficient, which is determined using impact experiment.

Then the total elastic deformation is

$$\delta_z^e = \delta_z^{e0} + d\delta_z^e = \delta_z^{e0} + k' \frac{p^{vp}}{p} d\delta_z \tag{3-30}$$

If this elastic deformation is fully recovered, the thickness of the powder compact corresponding to this point is

$$h_r^* = \frac{\delta_z^{e0}}{\varepsilon_z^{e0}} + \left(1 - k' \frac{p^{vp}}{p}\right) d\delta_z \tag{3-31}$$

Thus elastic strain ε_r^e can be determined by

$$\varepsilon_r^e = \frac{\delta_z^e}{h_r^*} = \frac{\delta_z^{e0} + k' \dfrac{p^{vp}}{p} d\delta_z}{\dfrac{\delta_z^{e0}}{\varepsilon_z^{e0}} + \left(1 - k' \dfrac{p^{vp}}{p}\right) d\delta} \tag{3-32}$$

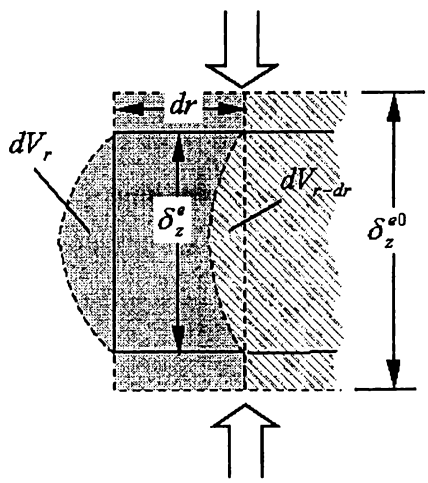

Figure 3-9. Powder flow caused by deformation

It should be noticed here that powder flows to its surrounding when powder compact is deformed. This needs to be taken into account to calculate the elastic deformation. In the above, $d\delta_z$ is assumed to be the same as the deformation of powder compact (including elastic deformation and visco-plastic flow). However, if a volume of powder, dV_{r-dr}, flows to layer from its inner layer, $r - dr$, powder deformation, $d\delta_z$, should be modified as

$$d\delta_z^{'} = d\delta_z - \frac{dV_{r-dr}}{rdr} \tag{3-33}$$

dV_{r-dr} can be determined through the following analysis.

As schematically shown in Figure 3-9, the volume of the layer r at t and $t-\Delta t$ are $2\pi rdr\delta_z^e/\varepsilon_r$ and $2\pi rdr\delta_z^{e0}/\varepsilon_r^0$ respectively. Considering that there is a powder volume of dV_{r-dr} flowed to this layer from its inner layer, which is $r-dr$ away from the center, the volume change at r distance away from the center can be determined by

$$dV_r = rdr\left(\frac{\delta_z^e}{\varepsilon_r} - \frac{\delta_z^{e0}}{\varepsilon_r^0}\right) - dV_{r-dr} \tag{3-34}$$

3.8 Impact Dynamics

When impact occurs, the force applied onto the powder compact increases, and in the mean time, the tools are decelerated in opposite directions. Eventually the tools reach a critical point, at which their relative velocity is zero. After that, the powder compact and tools start to recover their elastic deformation and the tools gain their velocity in opposite directions until the contact breaks.

At any time during the impact, the relative velocity can be determined by using the following equation based on the classical mechanics.

$$v' = v - \int_0^t F\left(\frac{1}{m_1} + \frac{1}{m_2}\right)dt \tag{3-35}$$

where v is the initial impact velocity; F is the impact force and m_1 and m_2 are tools' masses respectively

At any moment during the impact, the distance between tools, H, can be determined as follows:

$$H = H_0 - \int_0^t v dt \tag{3-36}$$

where H_0 is the distance between the tools when impact starts. It is equal to the original thickness of powder compact, h_0.

Then at any time the thickness of powder, h, is calculated by the following equation.

$$\mathrm{h} = \mathrm{H}_0 + \sqrt{\mathrm{R}^2 - \rho^2} - \sqrt{\mathrm{R}^2 - \mathrm{r}^2} - \left(\Delta - \Delta^*\right) \tag{3-37}$$

where Δ is the deformation of tools at distance r away from the contact centre and Δ^* is the deformation of tools at the brink of the contact area.

The radius of the contact area at any time can be calculated by using the following equation.

$$\rho^2 + \left[R - \frac{H_0 - H}{2} + \left(\Delta - \Delta^*\right)\right]^2 = R^2 \tag{3-38}$$

3.9 Determination of the Flow shear Stress in Powder Compact, τ_s

The flow shear stress in the powder compact, τ_s, can be related to the impact force by considering a simple model as shown in Figure 3-10. In this model, cylindrical powder compact is pressed between a hammer and an anvil at a very low speed. Since powder is "loose" materials, it is reasonable to assume there is no force beyond the pressing area. It is also assumed that the friction shear stress at the interfaces between the hammer and the powder compact, and between the powder compact and the anvil, is τ_s. For cylindrical system, if assuming the stress distributes evenly along r direction, as shown in Figure 3-11, we have the following equilibrium equation:

$$\frac{\partial \sigma_r}{\partial r} + \frac{\partial \tau_{zr}}{\partial z} + \frac{1}{r}\frac{\partial \tau_{\theta r}}{\partial \theta} + \frac{\sigma_r - \sigma_\theta}{r} = 0 \qquad (3\text{-}39)$$

Also supposing the strain distributes evenly along the peripheral direction in any z plane, we have $\tau_{r\theta} = \tau_{z\theta} = 0$. In axisymmitrical system, $\sigma_r = \sigma_\theta$, thus the above equation can be written as

$$\frac{\partial \sigma_r}{\partial r} + \frac{\partial \tau_{zr}}{\partial z} = 0 \qquad (3\text{-}40)$$

We also have the yield condition in this condition:

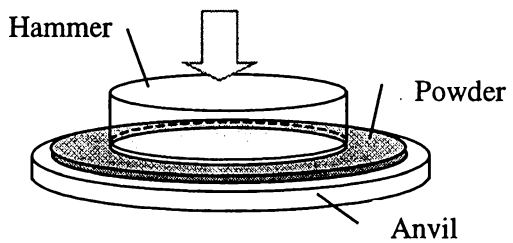

Figure 3-10. A compression experiment, where powder is free to flow to its around

$$(\sigma_r - \sigma_z)^2 + 3\tau_{zr}^2 = 3\tau_s^2 \rightarrow \sigma_r = \sigma_z \qquad (3\text{-}41)$$

Considering the friction over the contacting surface as the boundary condition as

$$\tau_{zr} = 2\tau_s \frac{z}{h} \qquad (3\text{-}42)$$

Equation (3-42) can be rewritten as

$$\frac{\partial \tau_{rz}}{\partial z} = \frac{2\tau_s}{h} \qquad (3\text{-}43)$$

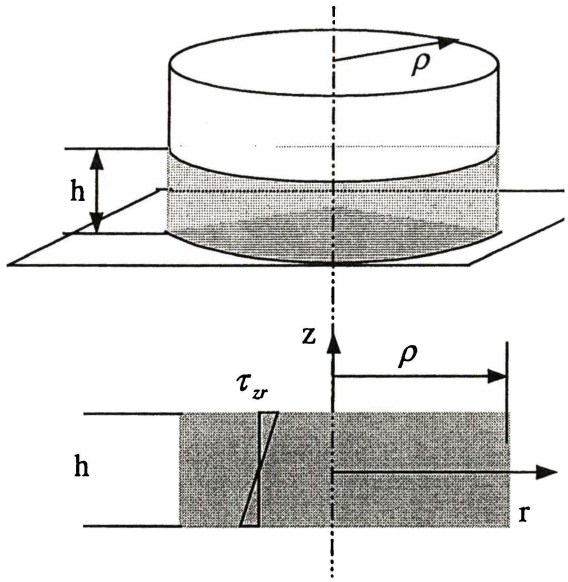

Figure 3-11. Schematic geometry of the powder compact and τ_{zr} distribution along thickness direction

From equations (3-40), (3-41) and (3-43), we have

$$\frac{\partial \sigma_z}{\partial r} = \frac{2\tau_s}{h} \qquad (3\text{-}44)$$

Since there is no applied force on the cylindrical side surface of the powder compact, equation (3-44) must satisfy the following boundary condition, which is defined by force equilibrium:

$$\sigma_z^b = -\sqrt{3}\tau_s \qquad (3\text{-}45)$$

where σ_z^b is the compressive stress in z direction at the side surface in the range from r to ρ, where, ρ is the radius of the hammer.

Integrating equation (3-43), we have

$$\int_{\sigma_z^h}^{\sigma_z} d\sigma_z = -\int_r^{\rho} \frac{2\tau_s}{h} dr \tag{3-46}$$

Then

$$\sigma_z = -\left[\sqrt{3}\tau_s + 2\tau_s\left(\frac{\rho - r}{h}\right)\right] \tag{3-47}$$

Since

$$F = \int_0^{2\pi}\int_0^{\rho} \sigma_z r dr d\theta \tag{3-48}$$

We have

$$F = -\left(\sqrt{3}\pi\rho^2\tau_s + \frac{2\pi\rho^3\tau_s}{3h}\right) \tag{3-49}$$

By rewriting equation (3-49), we have

$$\tau_s = -\frac{F}{\pi\rho^2\left(\sqrt{3} + \frac{2\rho}{3h}\right)} \tag{3-50}$$

where, F — the pressing force.

3.10 Determination of the Elastic Coefficient, k_e

The elastic coefficient of the powder compact, k_e, was determined by conducting a set of experiments, where a thickness of powder compact was cyclically compressed by two hammers.

Figure 3-12 shows a one-cycle compression experiment. From the result of recovery in this figure, if taking two points, which have extensions and loads x_1, x_2 and P_1, P_2 separately, we can write k_e by

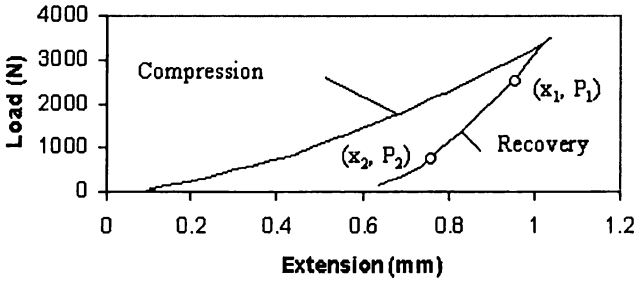

Figure 3-12. One cycle compression experiment

$$k_e = \frac{P_1 - P_2}{A} \frac{x}{x_1 - x_2} \tag{3-51}$$

where x is the thickness of powder after recovery and A, the contact area during compression.

3.11 Applying the Model

In order to apply the models, a numerical method was employed. Figure 3-13 shows the flow diagram of the calculation. At every time step, firstly the thickness

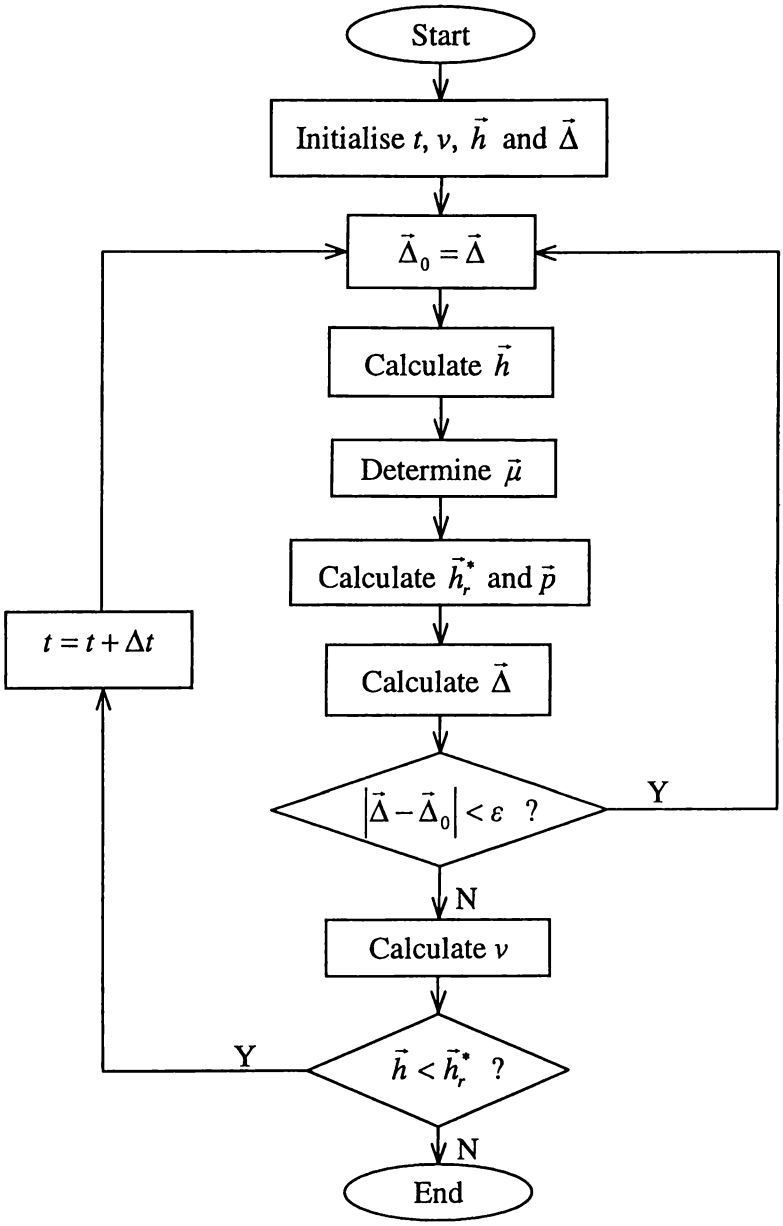

Figure 3-13. The computational logic for head-on impact model

distribution over the contact area of powder compact, $\vec{h}$, was calculated, and the viscosity distribution of powder compact was determined. Then the distribution of pressure, $\vec{p}$, and the distribution of deformation of tools, $\vec{\Delta}$, were determined. This process was iterated until $\vec{\Delta}$ did not change very much and went to the next time step. Calculation continued until the tools separated.

Before calculation, several unknown parameters need to be determined: the elastic coefficient k_e was determined through experiments using 304 stainless steel powder as described in Section 3.10; c_1 in equations (3-25) and (3-27) and k' in equations (3-29)~(3-31) were determined by using a reverse engineering method (as illustrated in Figure 3-14) in which the restitution coefficient (r_e) and the time (t_{max}) taken for the impact force to reach its maximum value of one of the experiments by Huang et al. [4] (sample A in Table 3-1).

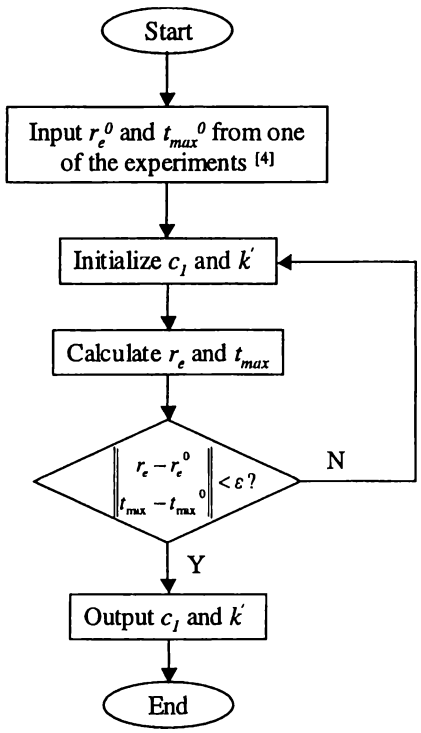

Figure 3-14. The method to determine c_1 and k'

3.12 Validation

The validity of the model has been tested by comparing the predicted impact force as a function of time and that measured by Huang et al. [4] under different conditions. The input parameters corresponding to the experiments conducted by Huang et al. [4] are shown in Table 3-1. Figure 3-15 shows the calculated and measured impact force as a function of time during impact under different conditions.

Table 3-1. Parameters in Huang et al.'s experiment [4]

Sample	The thickness of powder (mm)	The radius of ball (mm)	Impact velocity (m/s)
A	0.52	25.0	1.08
B	0.52	15.9	1.08
C	0.52	19.1	1.08
D	0.52	13.0	1.08
E	1.35	19.1	1.08
F	2.70	19.1	1.08
G	0.52	25.0	0.626
H	0.52	25.0	0.343

It has been explained in Section 3.11 that the parameters c_1 in equations (3-25) and (3-27) and k' in equations (3-29)~(3-31) were calculated by approaching the predicted time to the measured time taken for the impact force to reach its maximum value (for sample A). From Figure 3-15, the times taken for the impact forces to reach their maximum values predicted by the model strictly agree with the experimental results. It can also be seen that in most cases the simulation results are in overall good agreement with Huang et al.'s experimental results in the total impact duration time and the shape of the Impact Force-Time (F-T) curve. All the above results approve that the head-on impact model can predict the impact process.

However, there exist some discrepancies: the calculated forces are 150~450N higher than the measured maximum forces by Huang et al.'s experimental results and the maximum percentage error increases as the thickness of powder between balls increases (as shown in Table 3-2). To explain this discrepancy, we analysed the momentum change of the balls as following.

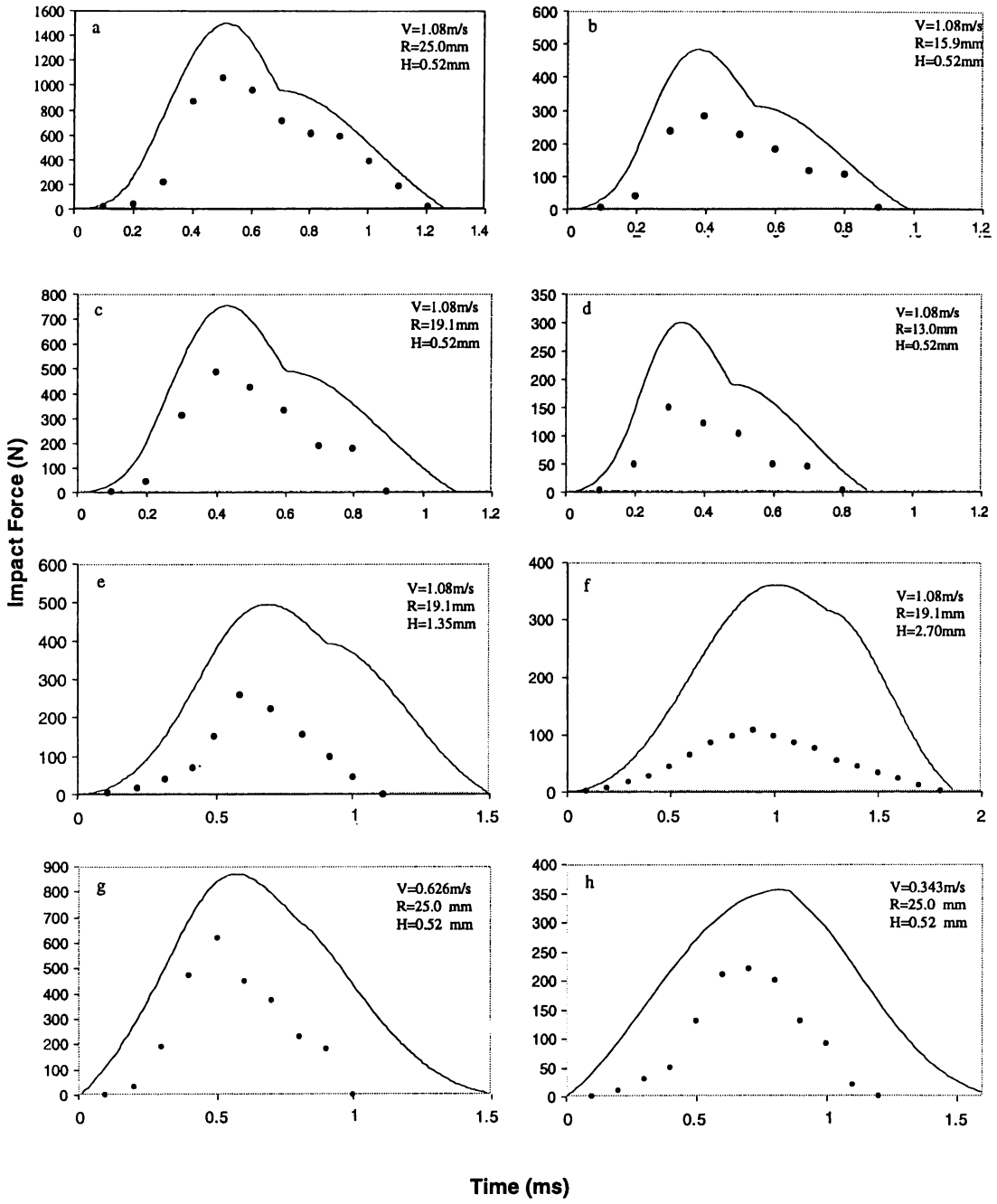

Figure 3-15. Impact forces as a function of time during impact under different conditions. V is relative velocity of tools, R is the radius of ball, and H is the initial thickness of powder compact. a~d: different ball diameters, a, e and f: different powder thickness, and a, g and h: different impact velocities

Table 3-2. Errors comparing between simulation results and Huang et al.'s experiment [4]

Sample	Maximum absolute error (N)	Maximum percentage error (%)
A	451.3	45.13
B	169.7	67.86
C	280.0	59.57
D	154.3	96.71
E	258.5	92.31
F	254.2	254.24
G	213.2	34.38
H	136.0	61.83

Table 3-3. Momentum and Momentum Changes in Huang et al.'s experiment [4]

Sample	$\sum F\Delta t$ (kg.s)	$m_b v_0$ (kg.s)
A	0.545	0.55135
B	0.189	0.24587
C	0.104	0.14184
D	0.055	0.07703
E	0.086	0.24587
F	0.081	0.25087
G	0.256	0.31958
H	0.109	0.17051

The measured total momentum change of the balls was determined by numerically integrating the measured F-T curve over the impact duration time, i.e. $\left(\sum F\Delta t\right)$, where F is the impact force and t is time. The initial momentum at the starting point of the impact was also calculated by multiplying the ball mass, m_b, and the initial velocity, v_0, $(m_b v_0)$.

Table 3-3 shows the comparison of the measured $\sum F\Delta t$ and $m_b v_0$ under different impact conditions. From Table 3-3, we can see in all cases, the measured $\sum F\Delta t$ is smaller than $m_b v_0$ and in some cases the difference is very large. This is certainly not reasonable, since the momentum change should be equal or greater than the initial momentum (i.e. $\sum F\Delta t > m_b v_0$) in order for the balls to stop or gain negative velocities. This observation suggests that the measured forces may be substantially lower than the real impact forces, or alternatively, the measured impact duration time may be shorter than the real duration time. The latter possibility is small considering the device used by Huang et al. [4] was a steel plate on a load cell. It is possible that the steel plate damped the impact and thus caused a smaller measured force. The thicker the powder compact, the more the damping effect the impact process has and thus the higher the measured error is. Dallimore and McCormick [5], who were co-authors of reference [4] together with Huang, also pointed out that there might be some error in the measured forces. Since the force predicted in our simulation was calculated based on the momentum change, as described by equation (3-35), the predicted force might be closer to the real force.

3.13 Application of the Head-on Impact Model to High-Energy Ball Milling

The model has been used to calculate the ball velocity, impact force and maximum pressure as functions of time during an impact between a stainless steel ball and a stainless steel wall, which might occur during high-energy ball milling using SPEX 8000 Mill/Mixer. The radius of the ball was 6.25 mm. The ball velocity just prior to impact was taken to be 10 m/s. The initial thickness of the powder trapped at the collision point was assumed to be 0.5 mm. Figure 3-16 shows the change of ball velocity, impact force and maximum pressure with time during this impact. It is clear that the impact lasts for about 0.32 ms and the impact force increases to its maximum

within 0.05 ms. After this point, the impact force quickly decreases and the speed of deceleration reduces. At 0.1 ms the velocity reaches zero and there is a turn for impact force at this point. For the rest of impact duration, the impact force reduces slowly and the velocity starts to increase slowly in opposite directions until the impact force reaches zero. The maximum pressure has the same tendency as the impact force. However, it reaches its peak slightly earlier than the impact force.

Simulations were carried out on the impacts between steel balls. Figure 3-17 shows the change of ball velocity, impact force and maximum pressure as functions of time during impact between two stainless steel balls at the same impact velocity and with the same thickness of powder as that of ball and wall described above. Comparing these two cases, we can find similar trend. While, it can be clearly visualized that there do exist some differences: the ball-ball impact results in a higher pressure, a lower impact force and a shorter impact duration time.

This discrepancy can be explained. For ball-ball system the equivalent radius is half

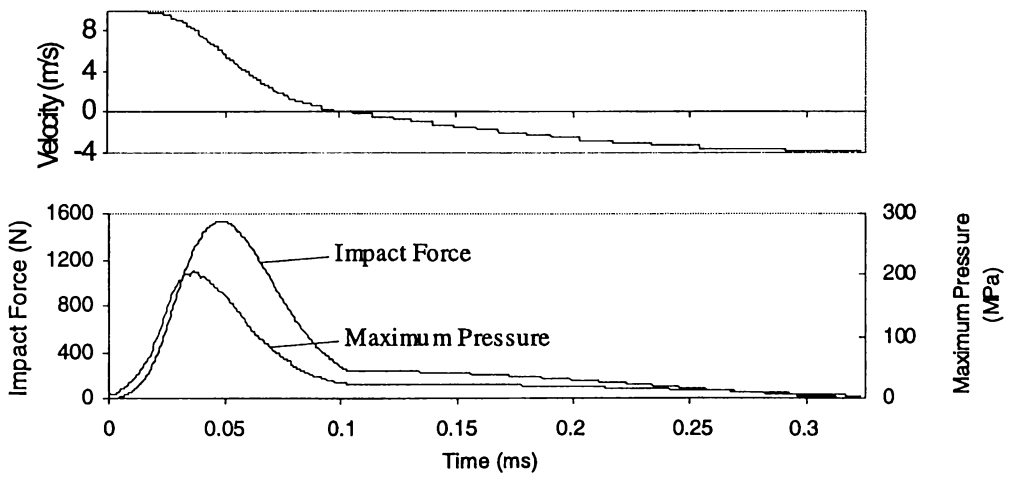

Figure 3-16. Impact force, maximum pressure and ball velocity as functions of time during a typical ball-wall impact. Ball initial velocity: 10 m/s; radius of ball: 6.25 mm; ball material: stainless steel; and initial thickness of powder compact: 0.5mm

of that for ball-wall system, according to equation (3-21). This causes a ball-ball system to have the smaller contact area, so this system gains a higher impact pressure although the impact force is lower. Thus the powder in ball-ball impact system undergoes more severe deformation. Since in ball-ball system, the balls decelerate faster, as shown in equation (3-36), the impact reaches its critical point earlier and has shorter impact duration.

Figure 3-16 and Figure 3-17 show that a single impact lasts for approximately 0.2~0.3 ms. This is about 100 times larger than the value used in the phase transformation model by Schwarz [6].

Simulations have also been carried out to examine the effects of various factors on impact pressure. These factors include impact velocity, ball size, ball density and powder thickness. Figure 3-18 shows the results of these simulations.

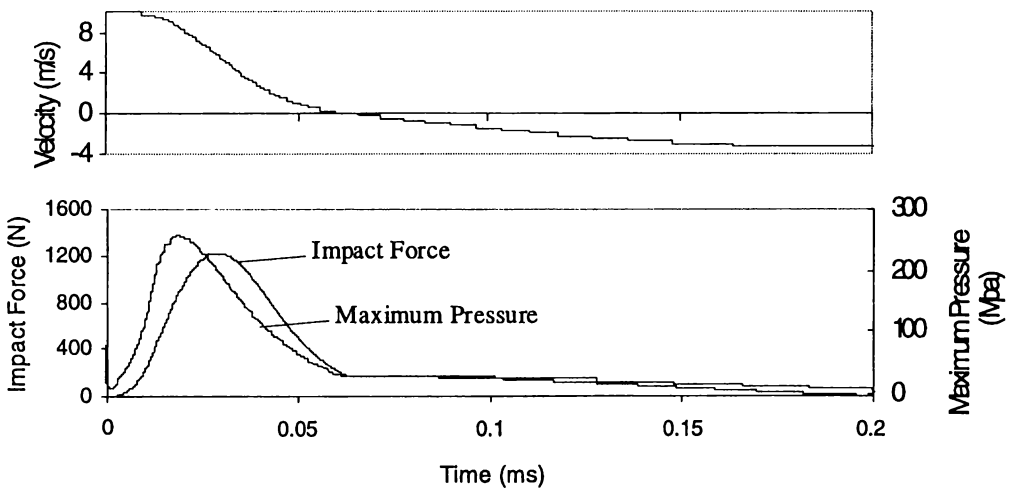

Figure 3-17. Impact force, maximum pressure and ball velocity as functions of time during a typical ball-ball impact. Ball initial velocity: 10 m/s; radius of ball: 6.25 mm; ball material: stainless steel; and initial thickness of powder compact: 0.5mm

Figure 3-18a shows that the maximum impact pressure increases almost linearly with the increase of the impact velocity. Figure 3-18b shows that the impact pressure increases with increasing the ball volume for a given impact velocity. As the mass of a ball increases significantly with its volume, this really shows that the impact pressure increases with impact energy. On the other hand, if the impact energy remains unchanged ($\frac{1}{2}mv^2$), our simulation shows (Figure 3-18c) that the impact pressure decreases with increasing ball volume. This is expected considering the fact that when two very big balls impact upon each other at a given energy (say 10 J), the impact velocity must be very small, in the mean time, and the contact area is very big.

As expected, changing ball density also influences the impact maximum pressure even though the mass of balls remains unchanged (as shown in Figure 3-18d). It can be seen in Figure 3-18d that the higher the ball density, the higher the maximum pressure.

Figure 3-18e shows how the maximum pressure changes with varying the thickness of powder while the ball size and impact velocity remains unchanged. It can be seen that the higher the powder thickness, the lower is the maximum impact pressure. This is caused by the change of the contact area and the decrease of the strain rate in equations (3-20a)~(3-20f) as the result of the change of powder thickness. It is clear that the damping effect of the powder is quite significant.

Figure 3-19a shows the ball deformation distribution over the contact area. Just as expected, ball deforms the most at the contact center. While, it also deforms at and beyond the brink of the contact area because of the wide stress field as shown in equation (3-1). Figure 3-19a also shows that at the brink of the contact area, there is a sharp turn of the pressure-distance curve.

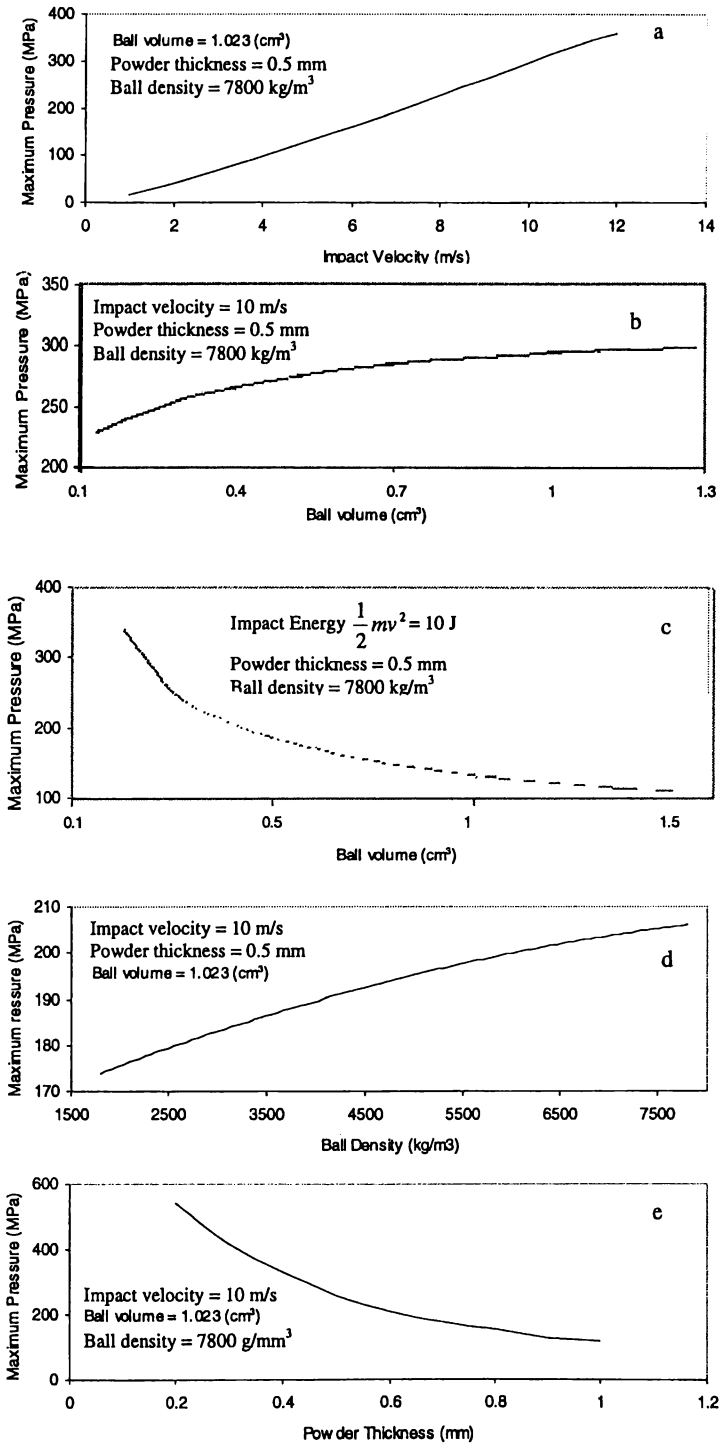

Figure 3-18. Maximum Pressure as functions of impact velocity, ball diameter, ball density and powder thickness respectively

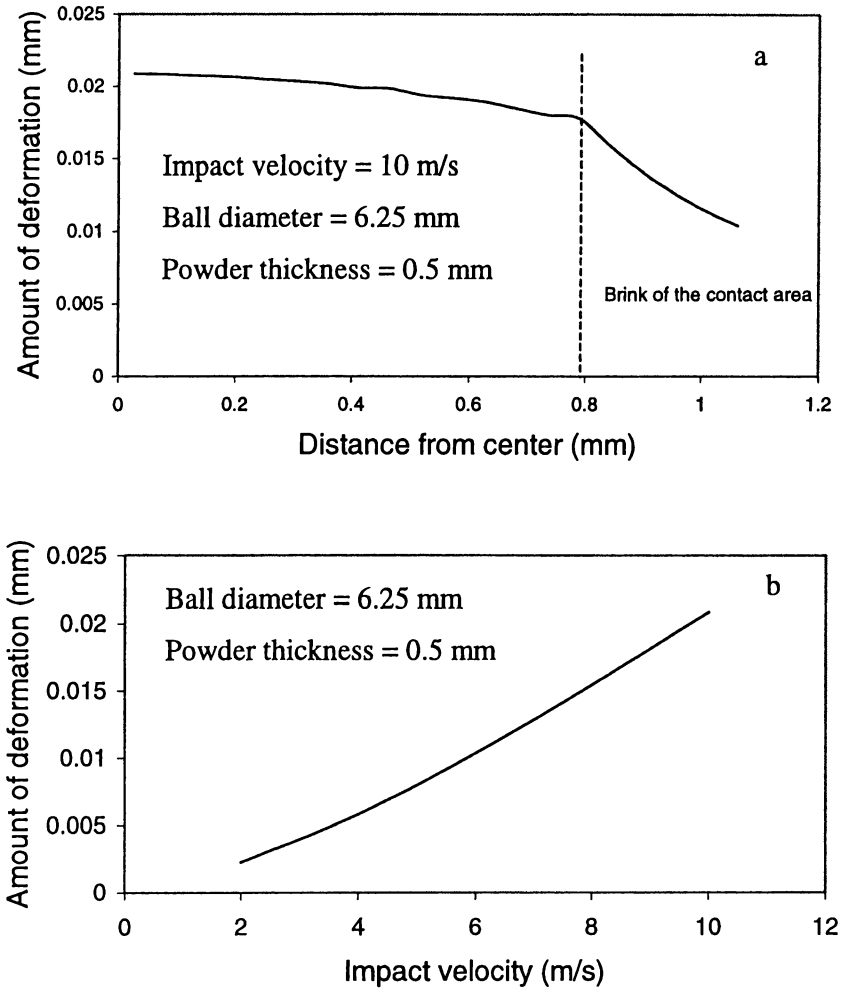

Figure 3-19. Ball deformation and its function of the impact velocities

Figure 3-19b shows the maximum amount of deformation as a function of impact velocity with constant ball size and powder thickness. It can be seen that the amount of ball deformation increases nearly linearly with the increasing of impact velocity. It is also noticed that ball deforms by nearly 20 μm when the impact velocity is close to 10 m/s. This is quite significant in comparison with the thickness of the powder involved in the impacts as shown in Chapter 4. Thus the ball deformation should be considered in simulation of impact.

3.14 Summary

A 3-dimensional model for single head-on impact process with powder in between has been deduced. The elastic deformation of balls, the elastic and plastic deformation and viscous flow of powder are considered. Experimental results in literature have been used to validate the simulation results. Application of the model in high-energy ball milling shows that the ball-ball and ball-wall impacts do have some difference, and the ball size, impact velocity and powder thickness may affect the impact pressure. It is also shown that the deformation of balls during impact is substantial.

3.15 References

1. Timoshenko, S.P. Goodier, J.N. *Theory of Elasticity*, McGraw-Hill, New York, 1970, 398.
2. Zhao, Zhiye and Wang, Guodong., *Modern Plastics*, Northeastern University Press, China, 1989.
3. Lemaitre, Jean and Chaboche, Jean-Louis, *Mechanics of Solid Materials*, Cambridge University Press, 1990, 38.
4. Huang, H., Dallimore, M.P., Pan, J., McCormick, P.G., "An investigation of the effect of powder on the impact characteristics between a ball and a plate using free falling experiments", *Materials Science and Engineering A*, **241**, 1998, 38.
5 Dallimore, M.P. and McCormick, P.G., "Distinct element modelling of mechanical alloying in a planetary ball mill", *Materials Science Forum*, **235**, 1997, 5.
6 Schwarz, R.B., "Microscopic model for mechanical alloying", *Materials Science Forum*, **269-272**, 1998, 665.

Chapter Four

Models for Other Forms of Impact and Powder Volume Trapped at Collision Point

4.1 Introduction

In Chapter 3, direct head-on impact was described as shown in Figure 4-1a. However, during ball milling, direct head-on impacts rarely occur. In most cases, the two balls impact at an angle not equal to zero degree, as shown in Figure 4-1b, i.e., which is oblique impact. In addition, the balls also spin at high speeds. In these cases, the two impacting balls not only press on the powder, but also slide along the tangile direction. Therefore, the friction force caused by the sliding balls must be considered as well as the pressing force. When an impact occurs, it lasts for a period of time. Within this period, other balls or wall may impact on one or both of the balls, resulting in a situation of multi-ball impact (as shown in Figure 4-1c). To simulate high-energy ball milling, we need to describe all these three forms of impact.

The thickness of the powder coating at the time of an impact has significant influence on the impact force during impact, on the dynamics of milling process and on the rate with which MA is accomplished. To simulate high-energy ball milling, we also need to determine the powder thickness or volume for every impact.

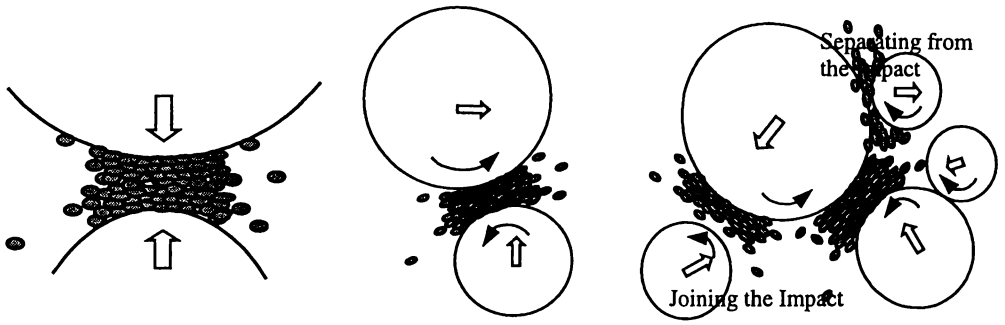

a. Head-on impact b. Oblique impact c. Multi-ball impact

Figure 4-1. Schematic diagrams showing different forms of impacts

4.2 Model for Oblique Impact

To analyse the oblique impact dynamics, a 4-dimension Cartesian coordinate system (as shown in Figure 4-2) was attached to the center of the contacting area. The Cartesian coordinate was orientated in such a way that axis x was aligned to the direction of the line connecting the centres of the two impact balls, and axis y was aligned to the tangential direction of the ball surface at the centre of contact area and in the same plane as the velocity of ball i, $\vec{v}_i$. Axis z was perpendicular to both x and y.

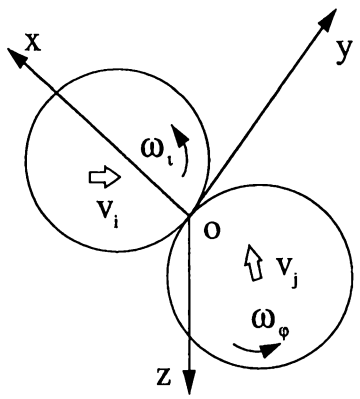

Figure 4-2. Coordinate system for impacting balls

The pressing force can be calculated by considering the head-on component of the impact using the model described in Chapter 3. The friction force can be determined by taking the following considerations. The sliding of the two balls is caused by ball spinning as shown in Figure 4-3a and by relative movement of the balls in the tangential direction (i.e. in y and z directions) as shown in Figure 4-3b.

The shear stresses on ball i from ball j due to the friction force caused by the spinning of balls in y and z direction, ${\tau^{ij}}_{\omega y}$ and ${\tau^{ij}}_{\omega z}$ can be calculated using the following equations.

$$ {\tau^{ij}}_{\varpi y} = \mu \frac{\varpi_{yj} R_j - \varpi_{yi} R_i}{h_r} \tag{4-1a} $$

$$ {\tau^{ij}}_{\varpi z} = \mu \frac{\varpi_{zj} R_j - \varpi_{zi} R_i}{h_r} \tag{4-1b} $$

where ϖ_{yj} and ϖ_{zj} are the components in y and z directions of the spinning angular velocity of ball j, ϖ_{yi} and ϖ_{zi} are those of ball i, R_i and R_j are the radii of balls i and j, h_r is the thickness of powder at a distance, r, away from the contact center, and μ is the viscosity of the powder compact trapped at the collision point. μ is related to the visco-plastic flow of the powder during impact and has already been determined in Chapter 3.

The shear stresses on ball i from ball j due to the friction force caused by the relative movement of the balls in y and z directions, ${\tau^{ij}}_{vy}$ and ${\tau^{ij}}_{vz}$, can be calculated using the following equations.

$$ {\tau^{ij}}_{vy} = \mu \frac{v_{yj} - v_{yi}}{h_r} \tag{4-2a} $$

$$\tau^{ij}{}_{vz} = \mu \frac{v_{zj} - v_{zi}}{h_r} \tag{4-2b}$$

where, v_{yj} and v_{zj} are the components in y and z directions of the parallel velocity of ball j and v_{yi} and v_{zi} are those of ball i.

The resistant forces of the powder compact on the impact balls can be determined by integrating these stresses across the contact area.

The resistant force acting on ball i by ball j can be determined by

$$\vec{F}^{ij} = \vec{F}^{ij}{}_x + \vec{F}^{ij}{}_y + \vec{F}^{ij}{}_z \tag{4-3}$$

where, $\vec{F}^{ij}{}_x$, $\vec{F}^{ij}{}_y$ and $\vec{F}^{ij}{}_z$ are resistant forces acting on ball i from ball j in directions x, y and z respectively. Their values are determined by

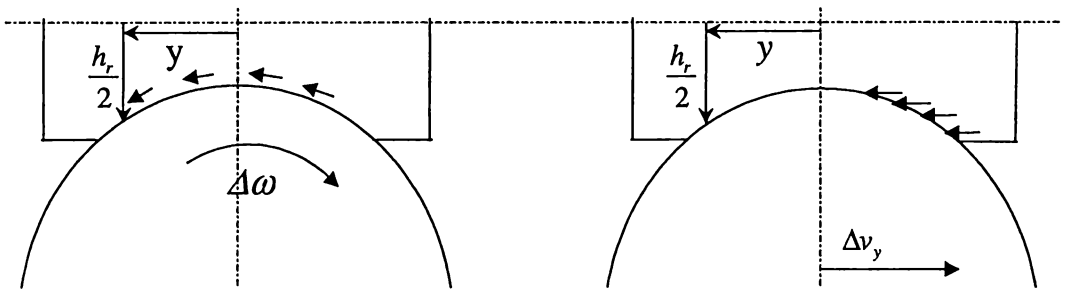

a. Sliding caused by spinning of balls

b. Sliding caused by difference in velocity of parallel movement of balls

Figure 4-3. Schematic diagrams showing different modes of sliding of balls

$$\left|\vec{F}^{ij}{}_x\right| = \int_0^{\rho}\int_0^{2\pi} prdrd\theta \tag{4-4a}$$

$$\left|\vec{F}^{ij}{}_y\right| = \int_0^{\rho}\int_0^{2\pi} \tau^{ij}{}_{\omega y} rdrd\theta + \int_0^{\rho}\int_0^{\pi} \tau^{ij}{}_{vy} rdrd\theta \tag{4-4b}$$

$$\left|\vec{F}^{ij}{}_z\right| = \int_0^{\rho}\int_0^{2\pi} \tau^{ij}{}_{\omega z} rdrd\theta + \int_0^{\rho}\int_0^{\pi} \tau^{ij}{}_{vz} rdrd\theta \tag{4-4c}$$

Using numerical method, the stresses p, $\tau^{ij}{}_{\omega}$ and $\tau^{ij}{}_{v}$ caused by the impact and the change of ball velocity can be determined by equations (2-22), (4-1) and (4-2) respectively.

The torque acting on ball i caused by the friction force acted from ball j can be determined by

$$\vec{T}^{ij} = \vec{T}^{ij}{}_y + \vec{T}^{ij}{}_z \tag{4-5}$$

where $\vec{T}^{ij}{}_y$ and $\vec{T}^{ij}{}_z$ are determined by

$$\vec{T}^{ij}{}_y = \vec{F}^{ij}{}_y R \tag{4-6a}$$

$$\vec{T}^{ij}{}_z = \vec{F}^{ij}{}_z R \tag{4-6b}$$

The parallel and angular velocity of ball i after a small time step, Δt, can be determined by using the following equations.

$$\vec{v}_i' = \vec{v}_i + \frac{\vec{F}^{ij} + \vec{G}^i}{m_i}\Delta t \tag{4-7}$$

$$\vec{\omega}_i = \vec{\omega}_i^{\,0} + \frac{\vec{T}^{ij}}{J_i}\Delta t \tag{4-8}$$

where $\vec{G}^i$ is the gravity force of ball *i*. It can be calculated by

$$\left|G^i\right| = m_i g \tag{4-9}$$

and the position of ball *i* after Δt can be determined by

$$\vec{S}_i' = \vec{S}_i - \vec{v}_i \Delta t \tag{4-10}$$

4.3 Model for Multi-Ball Impact

In order to describe a multi-ball impact, the impact was separated into several single impacts. The forces acted on every impacting ball were determined as analyzed above and in Chapter 3. Then the resultant force and torque of these forces was determined.

If ball *i* is impacting with *n* balls, the resultant force and toque can be determined by using the following equations.

$$\vec{F}^i = \vec{G}^i + \sum_{j=1}^{n} \vec{F}^{ij} \tag{4-11}$$

$$\vec{T}^i = \sum_{j=1}^{n} \vec{T}^{ij} \tag{4-12}$$

where, $\vec{F}^{ij}$ and $\vec{T}^{ij}$ can be determined by using equations (4-3) and (4-5) respectively.

The parallel and angular velocity of ball i after Δt can be determined by using the following equations.

$$\vec{v}_i' = \vec{v}_i + \frac{\vec{F}^i}{m_i}\Delta t \tag{4-13}$$

$$\vec{\omega}_i = \vec{\omega}_i^{\,0} + \frac{\vec{T}_i}{J_i}\Delta t \tag{4-14}$$

Where J_i is the moment of inertial of ball i.

The position of ball i after Δt can be determined by

$$\vec{S}_i' = \vec{S}_i - \vec{v}_i \Delta t \tag{4-15}$$

4.4 Volume of Powder Trapped at Collision Point

In modeling the ball milling process, it is essential to determine the volume of the powder compact trapped at each collision. The methodology used in the present study to determine the volume of powder trapped in collision was similar to that used by Maurice and Courtney [1]. It was assumed that when powder was poured onto a flat surface it formed a cone (Figure 4-4). A ball surface can be viewed as a complex body, which is combined by many small tilted "flat surfaces" (Figure 4-5).

It was assumed the powder distributes uniformly throughout the free space of the container. When a ball, which does not rotate, travels in the container, the powder will be "swept" by the ball. This process can be viewed as pouring the powder onto those many small tilted "flat surfaces".

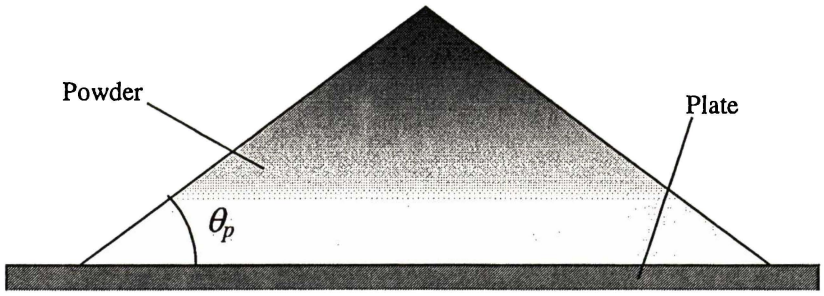

Figure 4-4. When powder is poured onto the surface of a plate, it forms a pile of a cone. The angle between the cone surface and the surface of the plate, θ_p, can be measured by an experiment for different powders.

Due to the geometric limit, there is a maximum volume of powder coated on the surface of a ball. Using the geometric model as described in Figure 4-6, the maximum volume (refer to Appendix II for details) is

$$V_{\max} = \frac{1}{3}\pi R^3\left[\sin^3\psi_{pb}\tan\theta_p - \left(1-\cos\psi_{pb}\right)^2\left(2+\cos\psi_{pb}\right)\right] \tag{4-16}$$

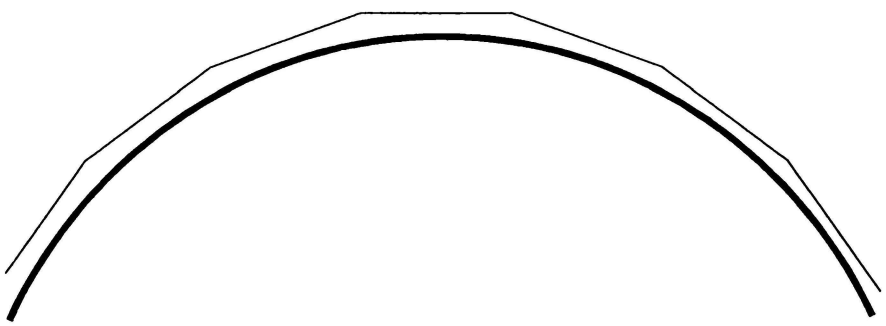

Figure 4-5. A ball surface can be viewed as a complex body, which is combined by many small tilted "flat surfaces"

$$\text{Where, } \psi_{pb} = \begin{cases} \theta_b, (\theta_b < \theta_p) \\ \theta_p, (\theta_b \geq \theta_p) \end{cases}$$

Where, θ_b is the friction angle of powder on ball surface, θ_p is the angle between the cone surface and the cone bottom when pouring the powder on a plate surface as shown in Figure 4-4 and ψ_{pb} is the angle formed by the cone resting on ball surface as shown in Figure 4-6. θ_b can be determined by the following equation:

$$\tan\theta_b = f_{pb} \tag{4-17}$$

where f_{pb} is the friction coefficient between powder particle and ball surface.

The maximum thickness of powder compact in this case is

$$h_{\max}(r) = [R\sin(\psi_{pb}) - r]\tan\theta_p - \sqrt{R^2 - r^2} + R\cos\psi_{pb} \tag{4-18}$$

After a ball travels by a distance, *S*, the thickness of powder accumulated on the ball surface could be:

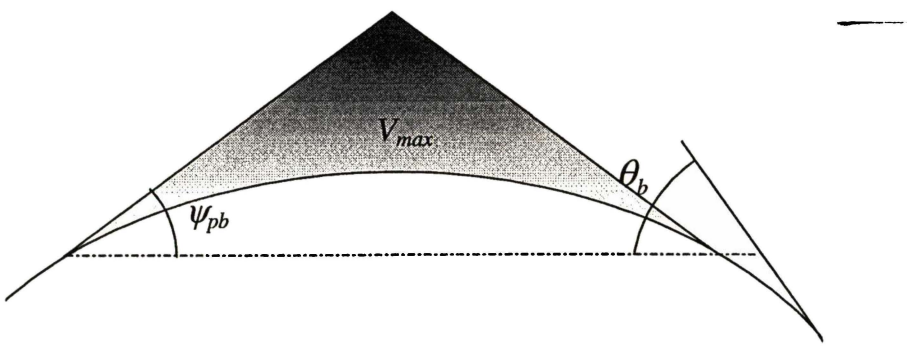

Figure 4-6. The shape of powder pile coated on the surface of a ball was assumed to be a cone

$$h_p = \frac{SV_p}{V_{container} - V_{balls}} \tag{4-19}$$

where, V_p is the total volume of powder, $V_{Container}$ is the volume of vial and V_{balls} is the total volume of balls.

While, if this thickness is greater than the maximum powder thickness at a distant, r, from the central axis, it will slip away to its surrounding, thus the powder thickness distribution over the ball surface is

$$h(r) = \begin{cases} h_p, & when\ h_p < h_{\max}(r) \\ h_{\max}(r), & when\ h_p \geq h_{\max}(r) \end{cases} \tag{4-20}$$

In this case if $h_p < h_{\max}(0)$, we have

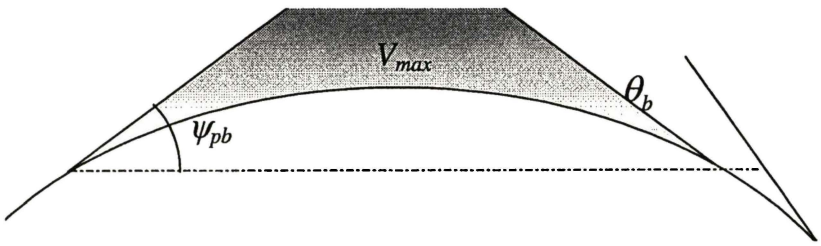

Figure 4-7. The shape of powder pile coated on the surface of a ball is assumed to be a cone

$$V_{\max} = \frac{1}{3}\pi R^3 \left\{ \left[\sin^3 \psi_{pb} \tan\theta_p - (1-\cos\psi_{pb})^2 (2+\cos\psi_{pb}) \right] - \left[1 - \frac{h_p}{h_{\max}(0)} \right]^3 \sin^3 \psi_{pb} \tan\theta_p + \lambda^2 (3-\lambda) \right\} \quad (4\text{-}21)$$

where $\lambda = 1 - \sqrt{1 - \left[\frac{h_p \sin\psi_{pb}}{h_{\max}(0)} \right]^2}$

In real situation, balls spin very fast and this causes a more evenly distribution of the thickness. Therefore it is reasonable to assume that the volume of powder calculated by equations (4-16)~(4-21) is evenly distributed on the surface of balls. This assumption generates the minimum thickness of powder compact:

$$h_{\min} = \frac{V_{\max}}{4\pi R^2} \quad (4\text{-}22)$$

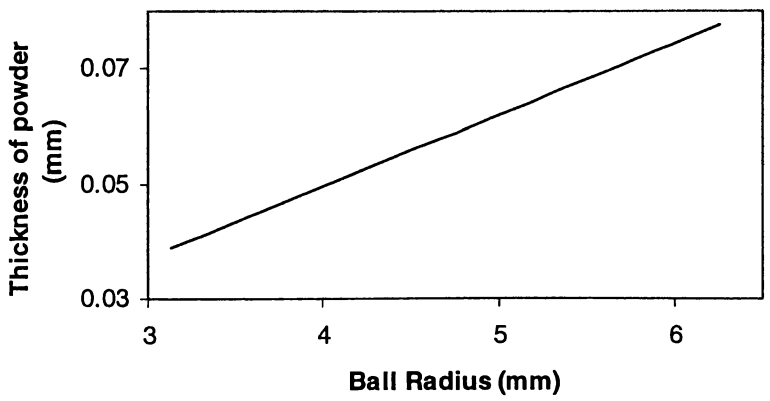

Figure 4-8. Powder thickness coated on the impacting ball as a function of ball size

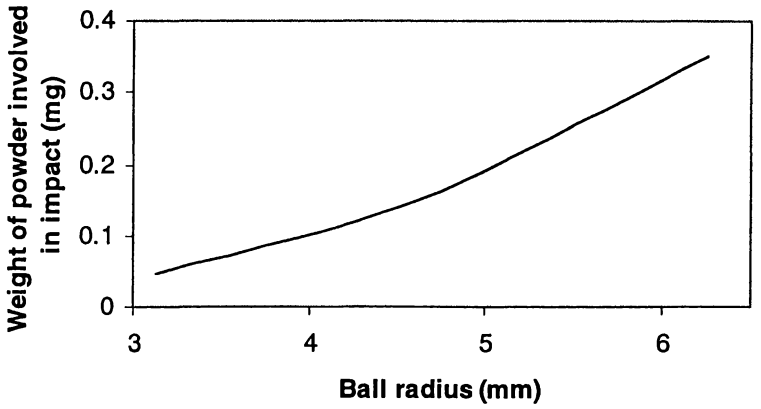

Figure 4-9. Coating weight involved in an impact as functions of the radius of ball

Figure 4-8 shows the minimum thickness of the powder coated on the surface of a ball by using equation (4-22). The set up was 3 gram stainless steel powder and 5 stainless steel balls were placed inside a vial with a diameter of 38 mm and height of 47 mm. As shown in Figure 4-8, the thickness of powder trapped at collision increases with the radius of balls and falls in the range of 0.03~0.07 mm.

From the calculated thickness of the powder and the contact area corresponding to an impact velocity of 10 m/s, the weight of stainless steel powder trapped was determined. Figure 4-9 shows calculated weight of stainless steel powder involved in an impact as a function of the radius of ball. It can be seen that the weight of powder involved in an impact is in the range of 0~0.4 mg. This is in good agreement with the experimental values by Gilman and Benjamin [2].

4.5 Reference

1. Maurice, David., "Local modeling of mechanical alloying", *PhD Thesis*, University of Virginia, 1992.
2. Gilman, P.S., Benjamin, J.S., "Mechanical alloying", *Annual Review of Materials Science*, **13**, 1983, 279.

Chapter Five

Global Model of SPEX 8000-Mixer/Mill

5.1 Introduction

In this chapter a three dimensional model is developed to simulate the global behaviour of a SPEX-8000 Mixer/Mill. The vial motion is numerically described based on the mechanics of the machine. The dynamics of balls are described based on the impact mechanics introduced in Chapter 4.

5.2 The Model for the Motion of Vial

Figure 5-1 shows a schematic working diagram of the SPEX mill. The mill operates by agitating a small vial at a high frequency in complex 3 dimensional cycles. The vial is driven by a motor and controlled by the bearing and the combined effect of the springs. A simplified model as shown in Figure 5-2 was used to deduce the vial motion. Two Cartesian coordinate systems were employed: one $(O-XYZ)$ was attached to the earth and the other one $(o'-x'y'z')$ was attached to the vial, as shown in Figure 5-2. OX was the central axis of the horizontal crankshaft and OY was the perpendicular line passing the intersection of OX and shaft-arm. $o'x'$ was the centre axis of the vial cylinder and $o'y'$ was in the longitudinal direction of the shaft-arm. At any time the positions in coordinate system $o'-x'y'z'$ were converted to the positions in $O-XYZ$, using the following equations based on the geometrical relationships:

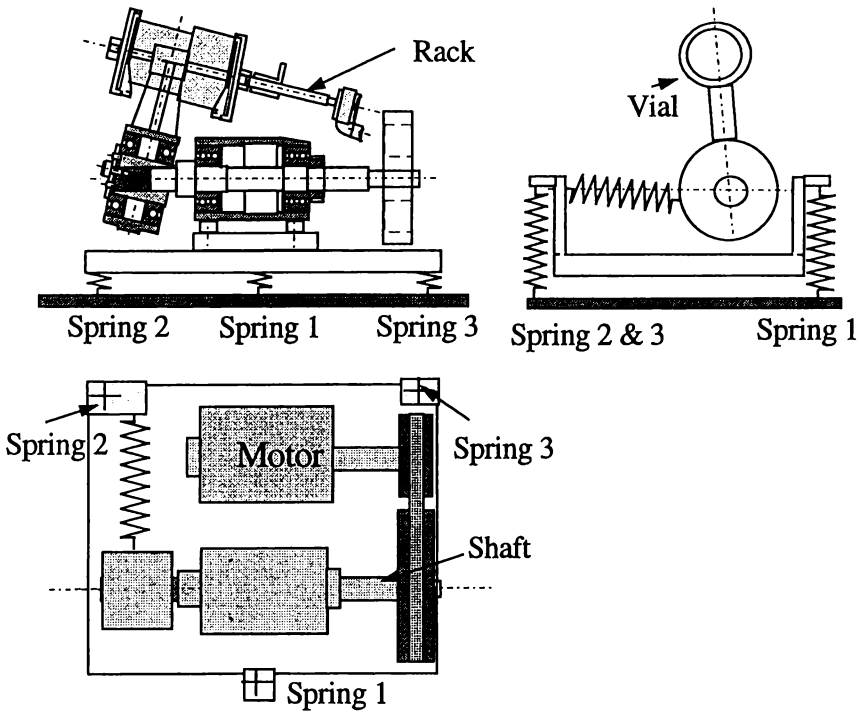

Figure 5-1. Schematic working diagram of a SPEX-8000 Mixer/Mill

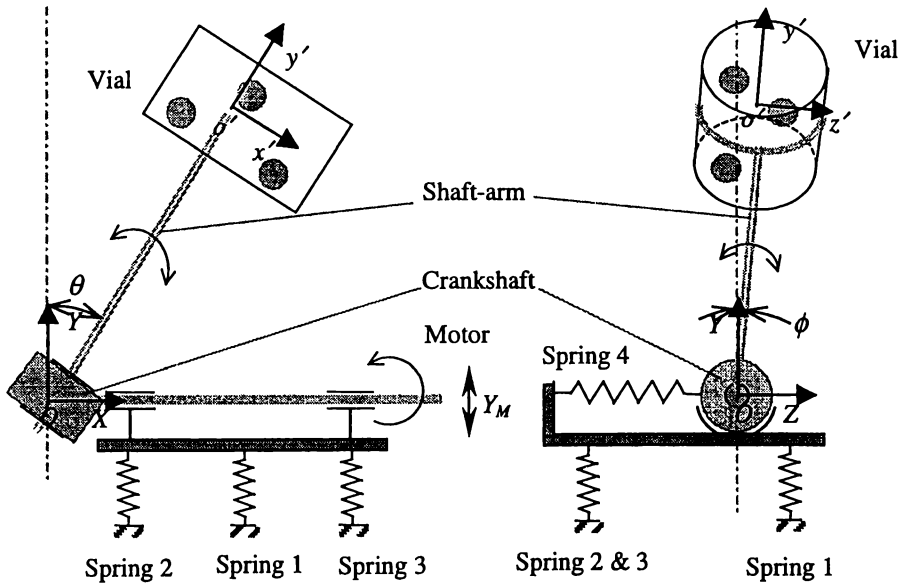

a. Front view

b. Side view from left

Figure 5-2. Diagram of the abstract model for a SPEX-8000 Mixer/Mill

$$X = x'\cos\theta_0 - \frac{(y'+d)\tan\theta_0\cos(\omega t-\phi)+z'\sin\theta_0\sin(\omega t-\phi)}{\sqrt{1+\tan^2\theta_0\cos^2(\omega t-\phi)}} \quad (5\text{-}1a)$$

$$Y = x'\sin\theta_0\cos\omega t + \frac{(y'+d)\cos\phi - z'[\sin\theta_0\sin\omega t\tan\theta_0\cos(\omega t-\phi)+\cos\theta_0\sin\phi]}{\sqrt{1+\tan^2\theta\cos^2(\omega t-\phi)}} + Y_m \quad (5\text{-}1b)$$

$$Z = x'\sin\theta_0\sin\omega t + \frac{(y'+d)\sin\phi + z'[\sin\theta_0\cos\omega t\tan\theta_0\cos(\omega t-\phi)+\cos\theta_0\cos\phi]}{\sqrt{1+\tan^2\theta_0\cos^2(\omega t-\phi)}} \quad (5\text{-}1c)$$

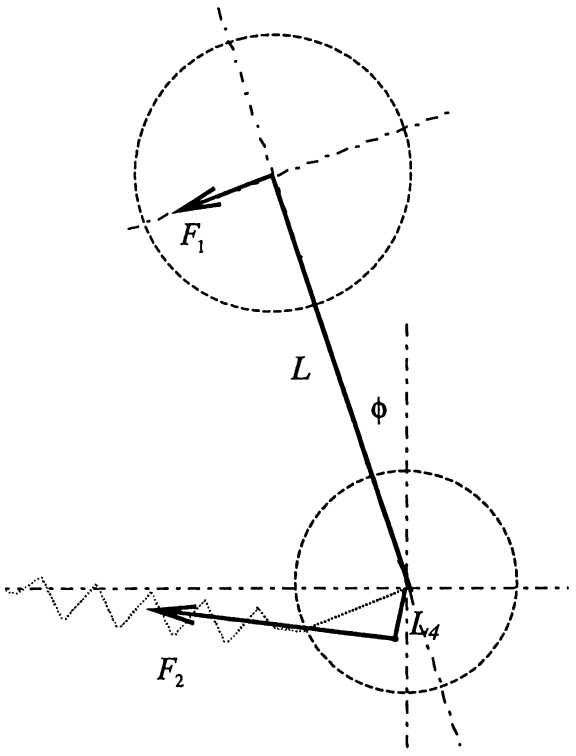

Figure 5-3. Free body diagram of shaft-arm motion balanced by Spring 4

where d is the length of shaft-arm, θ_0 is the initial angle between shaft-arm and axis y when milling starts, ϕ *is* the angle between shaft arm and line OY and ω is the angular velocity of crankshaft rotation.

Since the movement of the vial is balanced by the reaction force of spring 4 as shown in the free body diagram in Figure 5-3, a moment equilibrium equation was obtained:

$$F_1 L = F_2 L_4 \quad (5\text{-}2)$$

where F_1 is the reaction force of the vial on the shaft-arm due to acceleration/deceleration of the vial, F_2 is the elastic force from spring 4, and L and L_4 are force arms for F_1 and F_2 respectively as shown in Figure 5-3. They were

determined by the following equations:

$$F_1 = m_v\left(\frac{d^2Y}{dt^2}\cos\theta_0\cos\phi + \frac{d^2Z}{dt^2}\sin\theta_0\sin\phi\right) \tag{5-2a}$$

$$L = d + R_v \tag{5-2b}$$

$$F_2 = k_4\left[\sqrt{(l_1 + R_c)^2 + R_c{}^2 - 2(l_1 + R_c)R_c\cos\phi} - l_0\right] \tag{5-2c}$$

$$L_4 = \frac{(l_1 + R_c)R_c\sin\phi}{\sqrt{(l_1 + R_c)^2 + R_c{}^2 - 2(l_1 + R_c)R_c\cos\phi}} \tag{5-2d}$$

Where R_c is the radius of crankshaft, l_1 is the length of spring 4 when $\phi = 0$ and l_0 is the initial length of spring 4.

As the fulcrums of the SPEX mill are on top of springs 1, 2 and 3, they vibrate as the vial swings about point O (Figure 5-4). These springs were combined into one spring, which has an elastic coefficient k. It was assumed that the fulcrums vibrate only in y direction. According to Newton's second law of motion, we have:

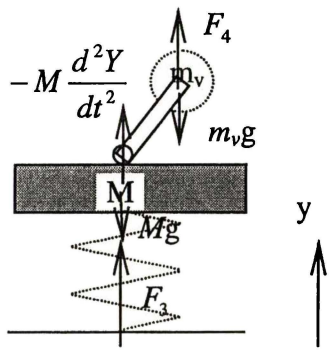

Figure 5-4. Free body diagram of the fulcrum's motion balanced by Springs 1, 2 and 3 in y direction

$$F_3 + F_4 - M\frac{d^2Y_m}{dt^2} = m_v g + Mg \tag{5-3}$$

where m_v is the mass of the vial, F_3 is the elastic force from springs 1, 2 and 3 and F_4 is the component in Y direction of the reaction force of the vial on the shaft-arm

due to acceleration/deceleration of the vial. They were related to Y and Y_m as follows:

$$F_3 = kY_m \tag{5-3a}$$

$$F_4 = m_v \frac{d^2Y}{dt^2} \tag{5-3b}$$

The initial position and velocity of the vial can be set as the initial conditions for equation (5-2) and the initial position and velocity of the fulcrums can be set as the initial conditions for equation (5-3a) and equation (5-3b). By assuming the movement of the vial is in a steady state, equations (5-1) ~ (5-3) can be solved numerically, and thus the position and motion of the vial at any time can be predicted.

5.3 Dynamics of Balls Inside the Vial

5.3.1 The Initial Positions and Velocities of Balls

The initial positions and velocities of balls must be determined before simulation. The following procedures were used in determining the initial positions of balls in the vial.

- Put the first ball on the bottom of the vial end as shown in Figure 5-5a, then line the other balls along the cylindrical wall until angle β reaches a limit;
- Rotate the vial by $\frac{\beta}{2}$ in the direction shown in Figure 5-5a, we get Figure 5-5b;
- Use the same method to put other balls in the next layer until the end as shown in Figure 5-5c.

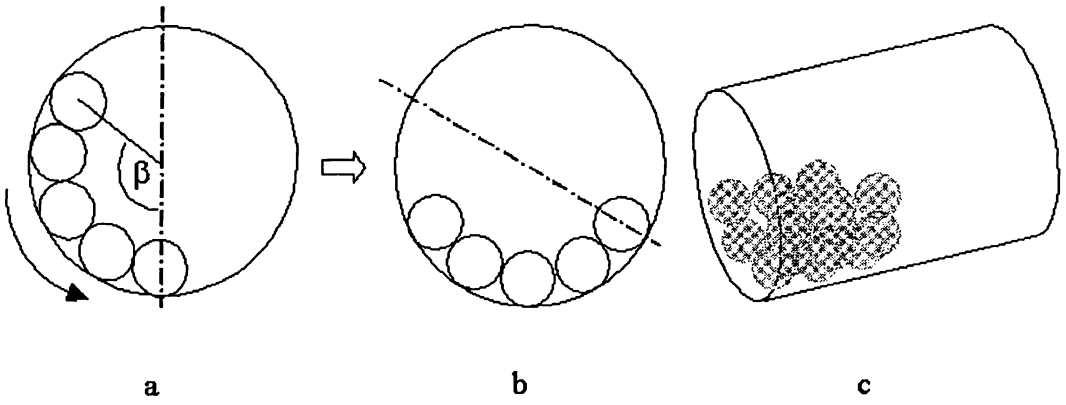

Figure 5-5. Ball original positions

When milling starts, the balls move together with the vial, thus the initial velocities of balls were assumed to be the same as those of the vial at the points where the balls and vial are in contact. This can be calculated by differentiating equations (5-1a~c) and setting $t = 0$.

5.3.2 Free Movement of Balls

During milling, balls are subjected to gravity forces and this affects their motion, especially during free travelling, which dominates most of the time during milling. These forces were considered to be active at any time (including dynamic impact process). The spinning velocities of balls remain constant during free flying. The velocities of balls were calculated using the following equations:

$$v_{xi} = v_{0xi} \tag{5-4a}$$

$$v_{yi} = v_{0yi} - g\Delta t \tag{5-4b}$$

$$v_{zi} = v_{0zi} \tag{5-4c}$$

where v_{xi}, v_{yi} and v_{zi} are the end velocities of the ball in x, y and z direction respectively after a small time step, Δt, g is the gravitational acceleration and v_{0xi}, v_{0yi} and v_{0zi} are the start velocities of the ball in x, y and z direction respectively at the beginning of the time step, Δt.

The positions of balls were calculated by using the following equations:

$$X_i = X_{0i} + v_{x0i}\Delta t \tag{5-5a}$$

$$Y_i = Y_{0i} + v_{y0i}\Delta t - \frac{1}{2}g\Delta t^2 \tag{5-5b}$$

$$Z_i = Z_{0i} + v_{z0i}\Delta t \tag{5-5c}$$

where X_i, Y_i and Z_i are the end positions of the ball in x, y and z directions respectively after time step Δt and X_{0i}, Y_{0i} and Z_{0i} are the start positions of the ball in x, y and z directions respectively at the beginning of time step Δt,

5.3.3 Impact between Balls

The positions of all the balls were monitored. After every small time interval, Δt, the distance between two different balls was calculated using the following equation:

$$d_{ij} = \sqrt{(X_i - X_j)^2 - (Y_i - Y_j)^2 - (Z_i - Z_j)^2} \tag{5-6}$$

If $d_{ij} \le r_{bi} + r_{bj}$, where r_{bi} and r_{bj} were the radii of ball i and j respectively, it was considered that the two balls were impacting. Then the positions, velocities and spinning velocities of the two balls at that time were used as the initial values for impact and the impact process was simulated using the local model described in Chapter 4.

5.3.4 Impact between a Ball and the Cylindrical Wall

To determine if a ball was impacting on the wall of the vial, we calculated the distance between wall and ball. To facilitate the calculation, the position of the ball in the $O-XYZ$ coordinate system (X_i, Y_i, Z_i) was converted to the position of the ball in the $o'-x_i'y_i'z_i'$ coordinate system (x_i', y_i', z_i') by using the following equations:

$$x' = X\cos\theta_0 + (Y - Y_m)\sin\theta_0\cos\omega t + Z\sin\theta_0\sin\omega t \tag{5-7a}$$

$$y' = \frac{-X\tan\theta_0\cos(\omega t-\phi)+(Y-Y_m)\cos\phi+Z\sin\phi}{\sqrt{1+\tan^2\theta_0\cos^2(\omega t-\phi)}} - d \tag{5-7b}$$

$$z' = -\{X\sin\theta_0\sin(\omega t-\phi)+(Y-Y_m)[\sin\theta_0\sin\omega t\tan\theta_0\cos(\omega t-\phi)+\cos\theta_0\sin\phi]-$$
$$Z[\sin\theta_0\cos\omega t\tan\theta_0\cos(\omega t-\phi)+\cos\theta_0\cos\phi]\}/\sqrt{1+\tan^2\theta_0\cos^2(\omega t-\phi)} \tag{5-7c}$$

The distance of the ball to the central axis of the vial, d_{ic}, is:

$$d_{ic} = \sqrt{y'^2 + z'^2} \tag{5-8}$$

If $d_{ic} \le r_{bi}$, where r_{bi} is the radius of ball i, it was considered that this ball was

impacting the cylindrical wall at (x_c', y_c', z_c'), which can be determined by the following equations:

$$x_c' = x_i' \tag{5-9a}$$

$$y_c' = R_v y_i' / d_{ic} \tag{5-9b}$$

$$z_c' = R_v z_i' / d_{ic} \tag{5-9c}$$

Then the velocity of the vial wall at the contact point can be determined by differentiating equations (5-1a~c). This velocity and the position of the contact point, the position, parallel and spinning velocities of the ball at that time were used as the initial values for the impact. The impact process was then simulated using the local model described in Chapter 4.

5.3.5 Impact between a Ball and the Ends of the Vial

The distances between ball *i* and the vial ends are

$$d_{ieL} = |x_i' + L_{eL}| \tag{5-10a}$$

$$d_{ieR} = |x_i' - L_{eR}| \tag{5-10b}$$

where d_{ieL} is the distance of the ball to the left end of the vial, d_{ieR} is the distance to the right end of the vial, L_{eL} is the distance from the left end to o' and L_{eR} is the distance from the right end to o'.

If either $d_{ieL} \le r_{bi}$ or $d_{ieR} \le r_{bi}$, it was considered that the ball was impacting with the

left or right end. The corresponding impacting point on the end wall (x_e', y_e', z_e') can be determined by the following equations:

$$x_e' = \begin{cases} -L_{eL} & when\ d_{ieL} \le r_{bi} \\ L_{eR} & when\ d_{ieR} \le r_{bi} \end{cases} \quad (5\text{-}11a)$$

$$y_e' = y_i' \quad (5\text{-}11b)$$

$$z_e' = z_i' \quad (5\text{-}11c)$$

Then the position of the contact point on the end, (x_e', y_e', z_e'), was used to determine the initial velocities at the contact point by differentiating equations (5-1a~c). This velocity and the position of the contact point, the position, parallel and spinning velocities of the ball at that time were used as the initial values for the impact. The impact process was then simulated using the local model described in Chapter 4.

5.4 Methodology of Computation

Based on the models developed, computation was performed to monitor the positions and velocities of all the balls step by step with small time intervals. The simulation employed the following process:

(1) Initialise the values used for simulation. These values include the maximum running time, the process parameters of milling indicating the number and size of balls, and the properties of powder, vial and balls.

(2) At every time interval, each ball was examined to determine whether it was involved in an impact. If it was not involved, it was in free flying, then go to (5).

(3) Determine whether this impact happened at the last time interval. If this impact did not happen at the last time interval, the impact was a new one. Then time, impact objects, positions, velocities, impact velocities and impact angle were recorded.

(4) Calculate the impact force, pressure, velocities, spinning velocities and positions using the local model described in Chapter 4. Go to (6).

(5) Calculate the velocities and positions using the model described in Section 5.3.2.

(6) Set the end velocities, spinning velocities and positions of the balls at the end of the impact as the initial value of the corresponding parameters for the next time step.

(7) Determine if time reaches the maximum running time. If not, go to (2). If yes, stop the program.

Chapter Six

Results and Discussion on Modeling of SPEX 8000 Mixer/Mill

6.1 Introduction

Described in this chapter are the simulation results on the milling dynamics of SPEX-8000 Mixer/Mills. The 3-dimensional motion of the vial was first studied considering the specific movement of this machine. Then the dynamics of the milling balls were investigated. As calculated in Section 5.4, the thickness involved in an impact is about 0.02~0.08 mm. The radius of balls varies from 3.94 mm to 6.26 mm as shown in Table 6-1 and the number of balls varies from 1 to 15. It was assumed that the balls and vial wall were always covered by a layer of powder with a thickness of 0.05 mm to simplify the simulation process. Then the powder involved in an impact was 0.1 mm thick. It takes 10^{-5} second for a ball to travel the distance of 0.1 mm at a velocity of 10 m/s, so the time-step in the program was set to be 2×10^{-7} second in order that the powder layer was not 'broken' unreasonably by the impacting balls with a few time steps.

Table 6-1. Size of balls used in simulation

Ball Weight (gram)	2	3	4	5	6	7	8
Ball Radius (mm)	3.941	4.511	4.965	5.349	5.684	5.984	6.256

After every 500 time-steps (i.e. 10^{-4} second), the positions and velocities of balls were calculated.

6.2 Motion of the Vial

By using the measured parameters as listed in Table 6-2, a series of simulations were performed to predict the vial motion during milling.

Table 6-2. Measured Parameters

The length of the arm, d	0.1 m
Starting angle of the arm, θ_0	30°
Vial mass, m_v	0.85 kg
Vial radius, R_v	0.019 m
Mill mass, M	14.074 kg
Rotation speed of the motor, ω	1500 rpm
The length of spring 4 when $\phi = 0$, l_1	0.012 m
The original length of spring 4, l_0	0.065 m
The elastic coefficient of Spring 4, k_4	260 kN/m
The elastic coefficient of the 3 springs combined, k	126 kN/m × 3

Figure 6-1a and Figure 6-1b show the calculated angle between shaft arm and the vertical plane XOY, ϕ, and the displacement of the fulcrums, Y_m, as functions of time respectively. It can be seen that $\phi(t)$ is close to a sine wave, while the fulcrums vibration $Y_m(t)$ is quite complex, but overall still takes a waveform, which is a combination of several different waves. The amplitude of the overall wave for $Y_m(t)$ is approximately 0.5 mm.

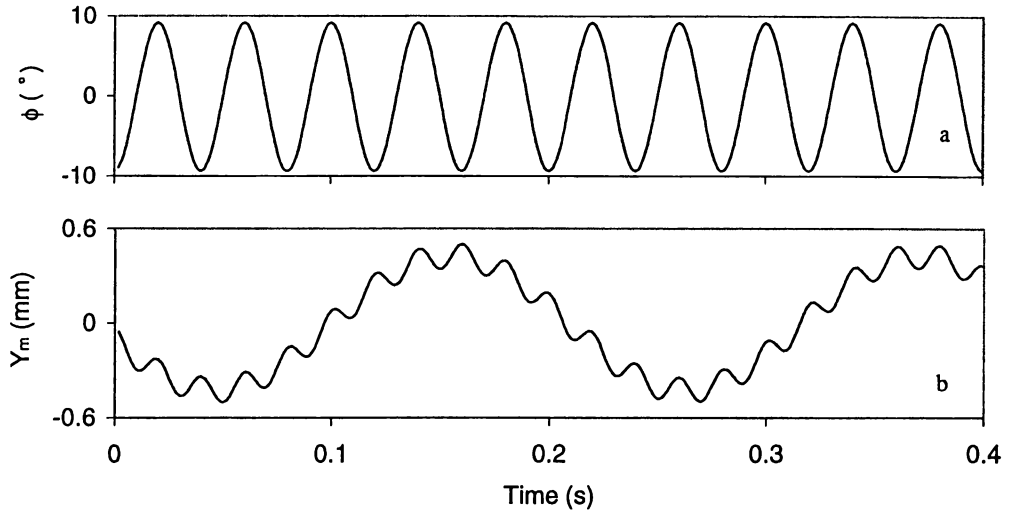

Figure 6-1. ϕ and Y_m as functions of time predicted by the program

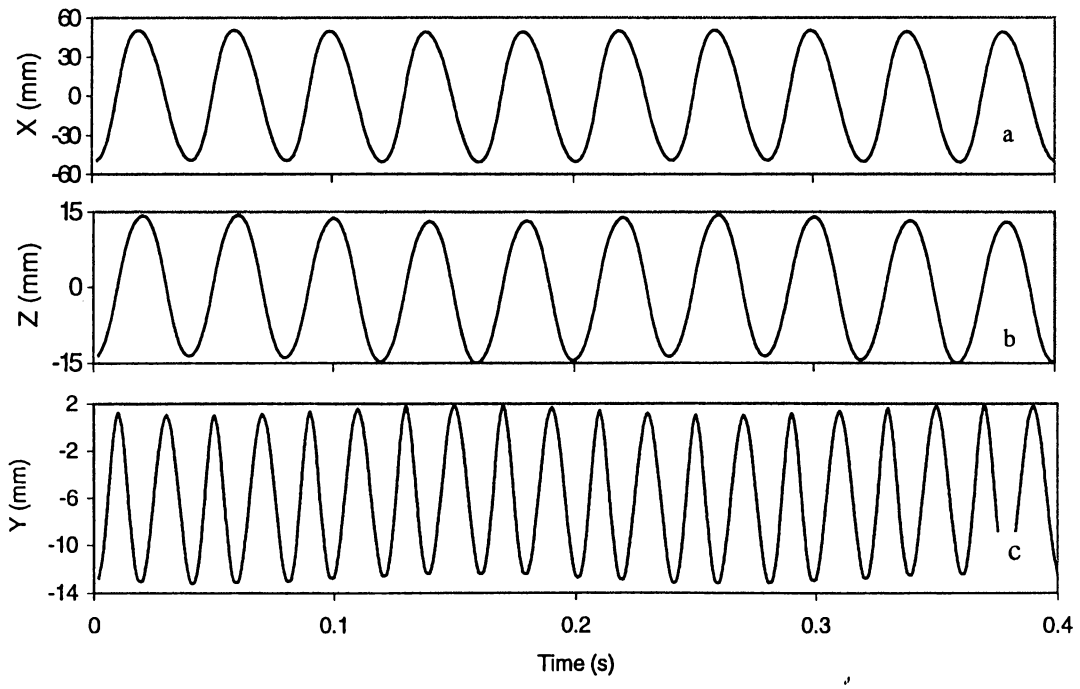

Figure 6-2. The predicted positions of the end of the shaft arm as functions of time

Figure 6-2 shows the predicted positions of the end of shaft-arm in *X*, *Y* and *Z* directions as functions of time. It is clear that the vial vibrates in 3 directions, especially in *X* and *Z* directions and the amplitudes of the vibrations in those directions could reach 51 and 15 mm respectively. In *Y* direction, the motion of vial is mostly affected by the vibration of the fulcrums, so the vial does not vibrate with very large amplitude, but at a much higher frequency.

Figure 6-3 is the predicted positions of the right end of the vial in *X*, *Y* and *Z* directions as functions of time. It can be seen that the motion of this point in *X* and Z directions takes a much large vibration amplitude than that of the end of the shaft arm. The motion in *Y* direction takes more complex cycles.

After it has been used for a certain time, the mill might get 'old' and the springs might become loosened because of fatigue. Simulations were performed to study the

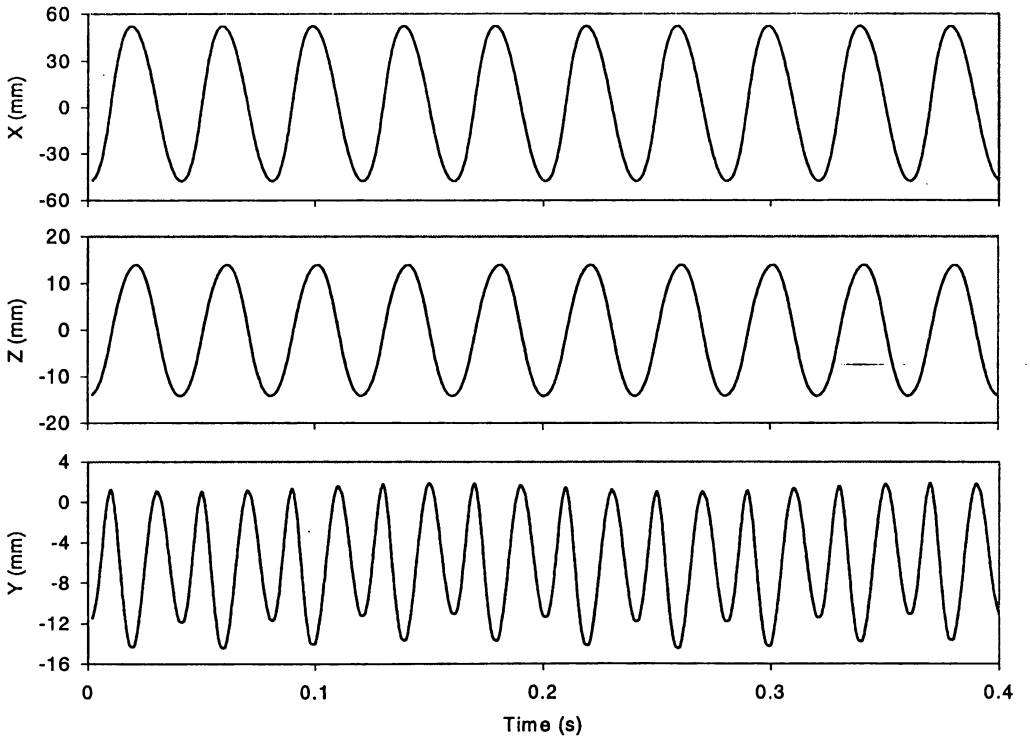

Figure 6-3. The predicted vial motion in X, Y, Z directions as functions of time for the right end of the vial

effect of 'loosened' spring 4, whose elastic coefficient was 150 kN/m (as shown in Figure 6-4). In this case, the vial vibrates at an angle ϕ of nearly twice that of the real situation, where the elastic coefficient is 260 kN/m. Since the space inside the mill is quite limited, the above situation suggests this vibration might be abnormal and cause the vial to bump the mill frame.

As introduced in Section 2.6.7, most of the previous studies heavily simplified the motion of SPEX mills into that of vibration in only one direction [1,2,3]. Although Caravati et al. [4] analyzed this process using a 3-dimensional model, they assumed there was no movement of fulcrums and the effect of the springs was ignored. While, present simulation results prove that the vibration of the vial is not negligible in any of the 3 directions. The vibratory motion of the fulcrums and the effect of spring 4 should also be considered in order to develop a model which can realistically describe the motion of the vial. This is the strength of the current model.

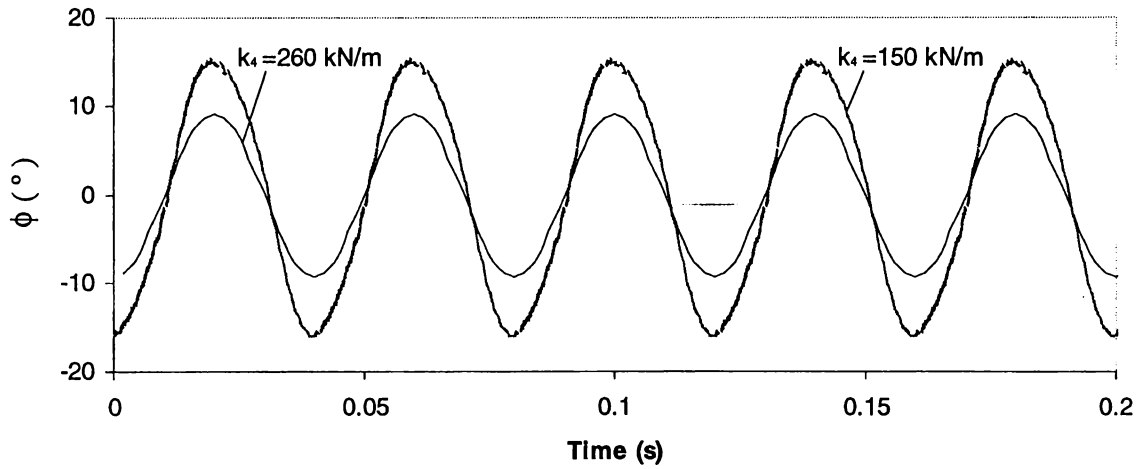

Figure 6-4. The effect of 'loosened' spring 4, whose elastic coefficient is 150 kN/m comparing with a regular spring 4, whose elastic coefficient is 260 kN/m

6.3 One Ball in the Vial

A series of simulations were performed under the condition that there was only one ball with 3.94 mm in radius inside a vial with 38 mm in diameter and 47 mm in length to study the ball trajectory and velocity. The positions of the ball and the vial were monitored. Figure 6-5 shows examples of the results which allow visualization of the movement of ball and vial.

To study the milling dynamics, the 3-dimensional trajectory of the ball was calculated for 1 second. Figure 6-6 shows the result. From Figure 6-6a and Figure 6-6b one can see that the trajectory of the ball is very irregular. Figure 6-6c shows that the ball is running or rolling/sliding close to the cylindrical wall for most of the time.

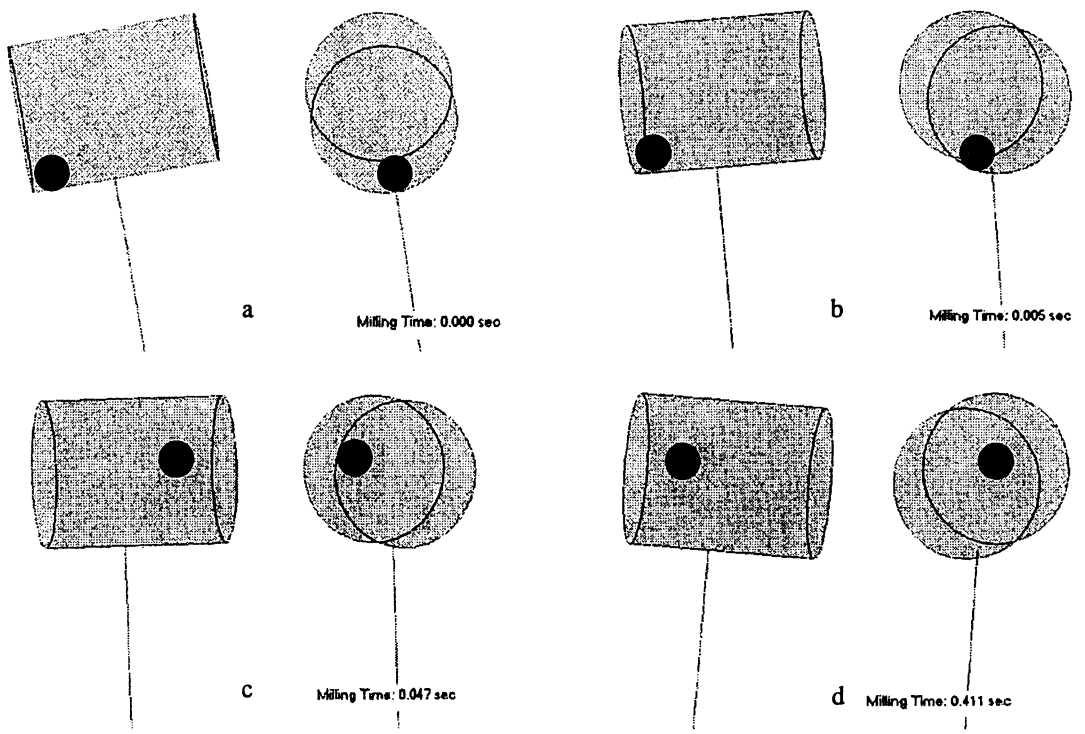

Figure 6-5. Examples of simulated result showing the ball position inside the vial at different times for a mill with one ball

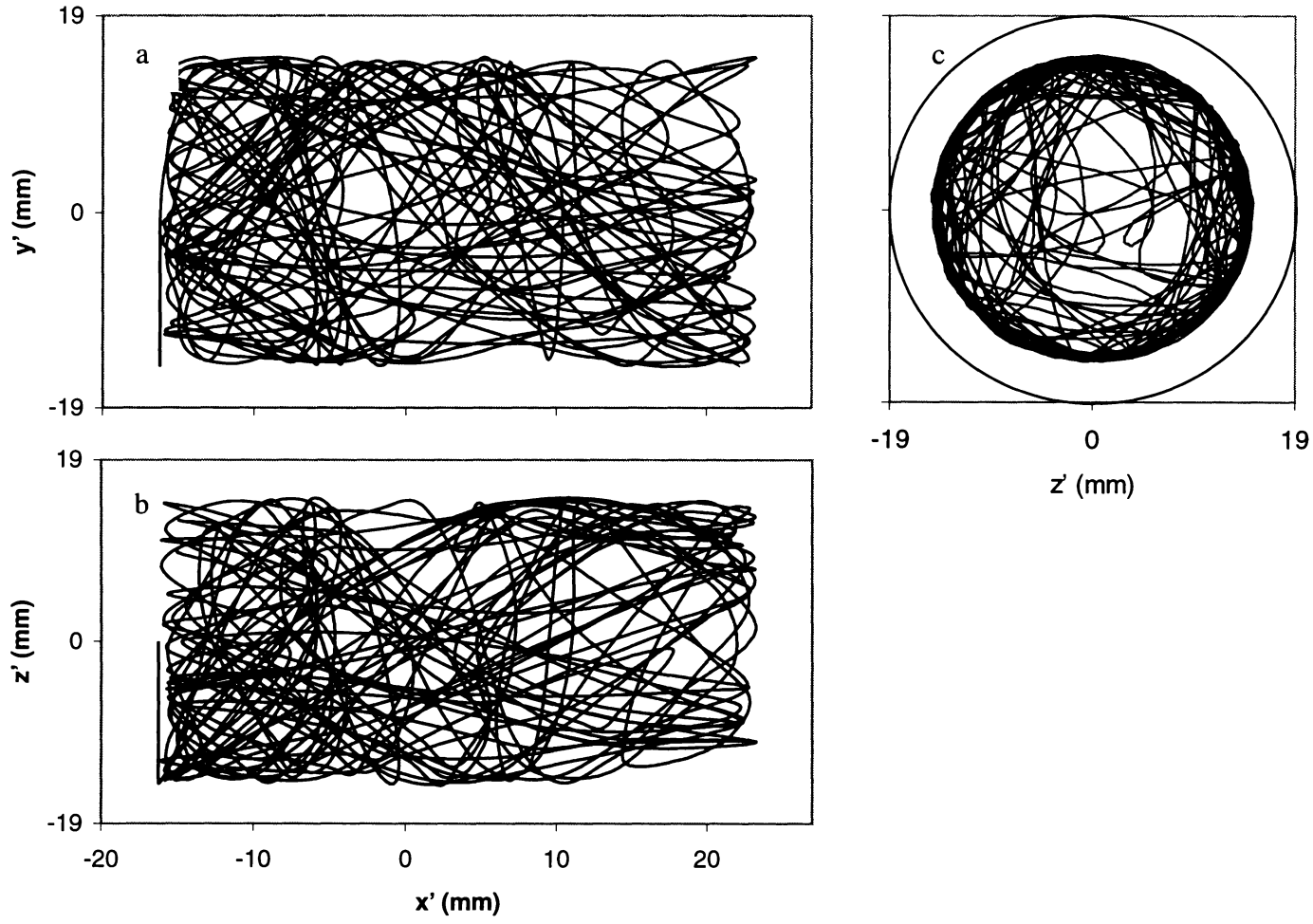

Figure 6-6. The trajectory of the ball in 1 second for SPEX 8000 Mixer/Mill with one ball in the vial, projected to (a) plane $x'o'y'$, (b) plane $x'o'y'$ and (c) plane $y'o'z'$

Since the vial is a cylinder, it is convenient to convert the position in $o'-x'y'z'$ system into a cylindrical system. Thus functions $r=\sqrt{y'^2+z'^2}$, where r was the distance from the ball to axis $o'x'$, and $v_r=\sqrt{v_{y'}^2+v_{z'}^2}$, where v_r was the velocity of the ball in r direction, were used to describe the position and velocity of the ball.

The position of the ball in r direction in the vial with 1 second is shown in Figure 6-7a and the trajectory of the ball projected to the left end of vial during 0 to 0.2 second is shown in Figure 6-7b. It can be seen that the ball nearly keeps sticking to the cylindrical wall at the starting stage of milling when the milling has not reached the stable condition. At the beginning the ball does not move or rotate relative to the vial, then it starts to slip and roll from its starting position (as shown in Figure 6-5a). As time goes, the ball slips and rolls from its starting position (Figure 6-5a) on the cylindrical surface of the vial along a spiral route (Figure 6-5b). When it hits the vial end (Figure 6-5c), it starts a new spiral route. After this stage, the ball reaches a stable stage (Figure 6-5d). It starts to avoid the sticking to the cylindrical wall as shown in Figure 6-7a. This is more clearly demonstrated in Figure 6-7c, which shows the trajectory of the ball projected to the left end of the vial during 0.8~1 second. The ball moves in several different modes: free flying, slipping and rolling on the cylindrical surface, and bumping on the end and cylindrical wall of the vial. Although it impacts the cylindrical wall occasionally, the ball bumps away immediately.

Figure 6-8 shows the spinning speed of the ball as a function of time during 0~1 second. It can be seen that the ball spins at a high speed in the range of 0~120 rotations per second. This speed varies with time and has a mean value of approximately 80 rotations per second.

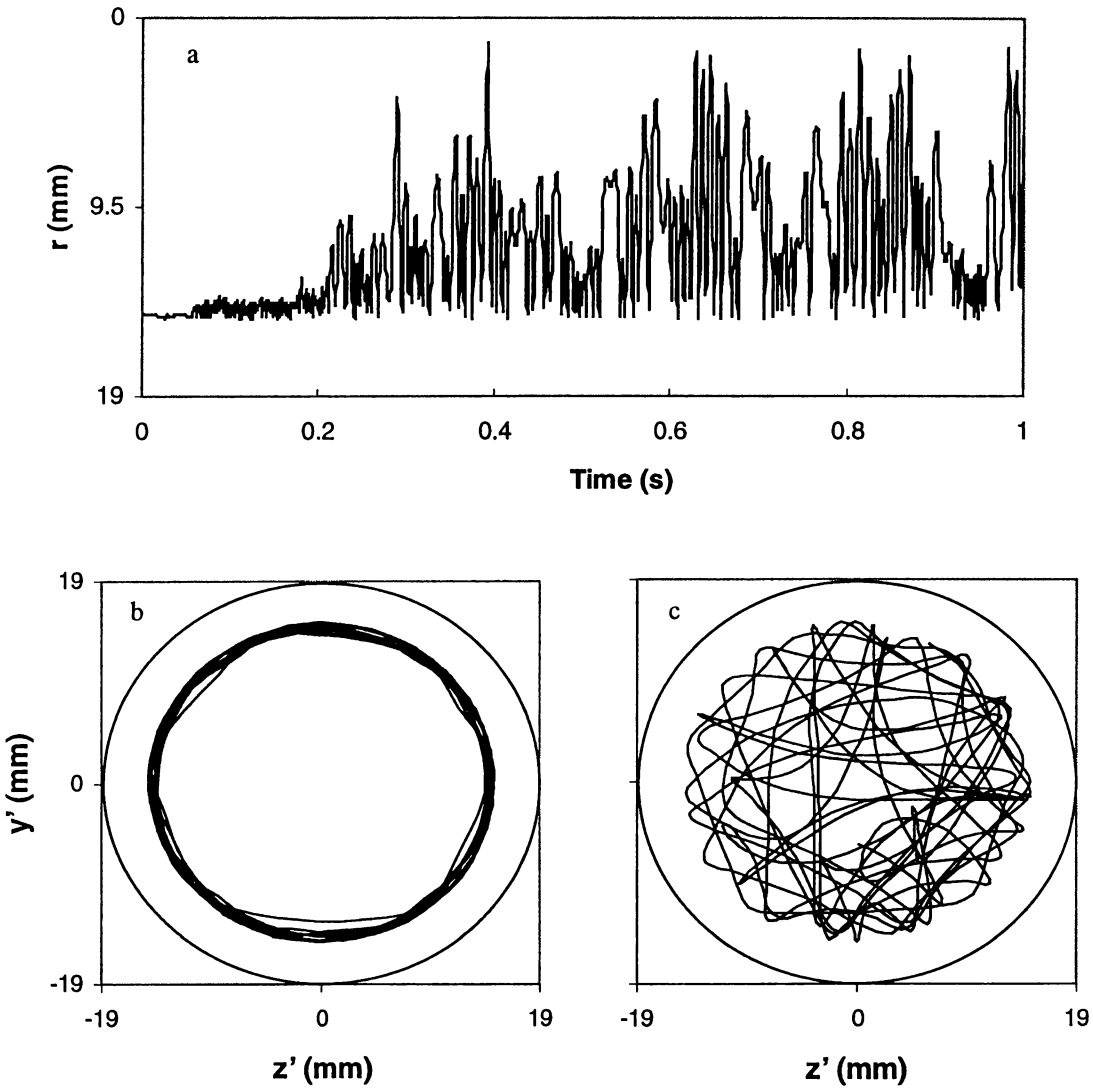

Figure 6-7. (a) Ball position in r direction in the vial as a function of time, (b) the trajectory of the ball projected to plane $y'o'z'$ as a function of time during 0~0.2 second and (c) the trajectory of the ball projected to plane $y'o'z'$ as a function of time during 0.8~1 second

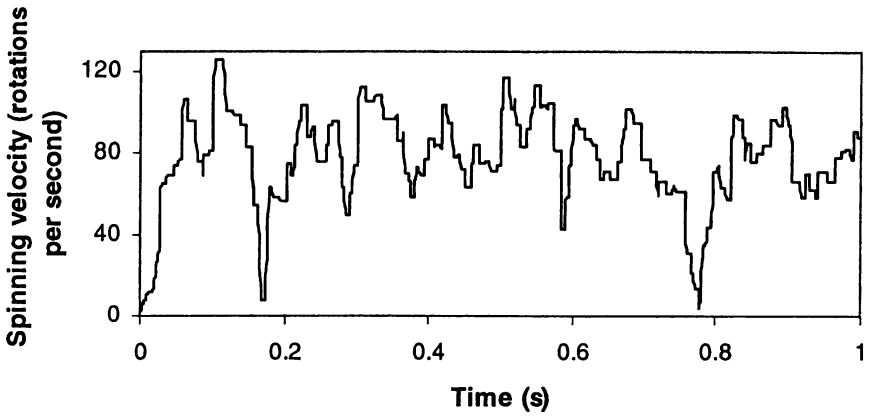

Figure 6-8. The spinning speed of the ball as a function of time

The velocity of the ball in reference with the vial in different directions as functions of time is shown in Figure 6-9. Figure 6-9a shows the change of velocity of the ball in the longitudinal direction of vial. This determines the impact velocity, which is defined as the relative velocity between the impact objects in head-on direction, between the ball and the ends of vial. It can been seen that the ball quickly gains velocity in this direction in the starting stage. Figure 6-9b shows the change of velocity of the ball in the peripheral direction of vial. This establishes the tangential velocity between the ball and the cylindrical wall. While, the velocity in *r* direction increases slowly as shown in Figure 6-9c. This velocity builds up the impact velocity between the ball and the cylindrical wall. In this early stage, the velocity fluctuates in a higher range than its later stage. It can be imaged that the ball has an unstable movement. After this stage, the ball "gets used" to its environment and has a smaller vibratory range of velocity.

Figure 6-10 shows the impact velocity of each of the impacts, which occur during 1 second. It has been shown in Figure 6-9c that the velocity in *r* direction is not very high in the starting 0.05 second and this causes the impact velocity of most of impact to be very small. However, the frequency of impacts in this small time period is very high. With increasing time, the frequency of impact decreases and impact velocity increases. After about 0.3 second, the impact frequency reaches nearly saturation. The impact frequency is about 165 Hz, which is much higher than the frequency of vial vibration, which is 25 Hz. This might be explained by the fact that too many impacts

happen between the ball and the cylindrical wall of vial. It was counted that 65% of these impacts are between the ball and the cylindrical wall and the remaining were between the ball and the two ends of vial. The maximum impact velocity is about 6 m/s.

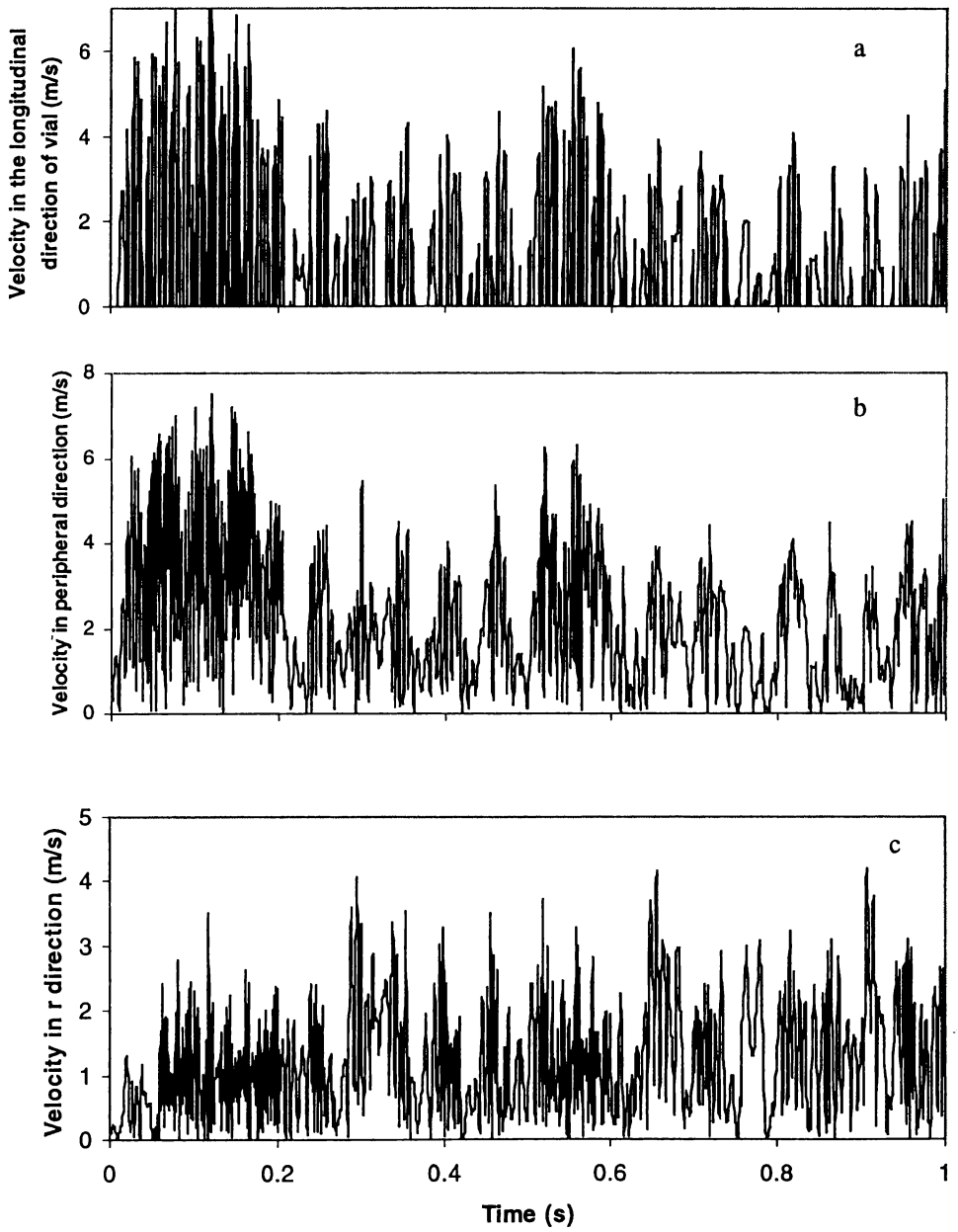

Figure 6-9. Velocity of the ball in reference with to the vial in different directions as functions of time

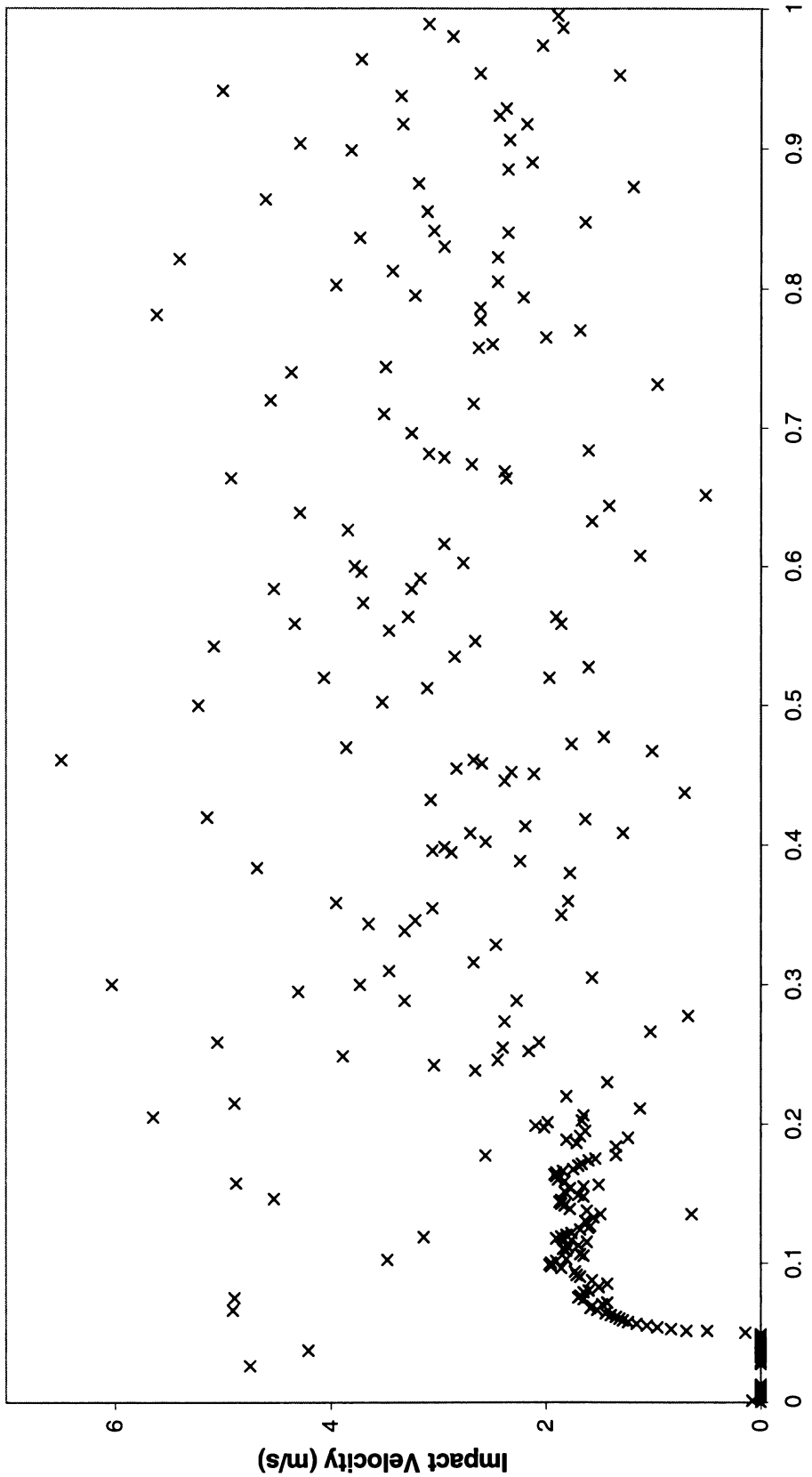

Figure 6-10. The impact velocity of each of the impacts occurred during 1 second

6.4 Multi Balls in the Vial

6.4.1 The Motion of Balls

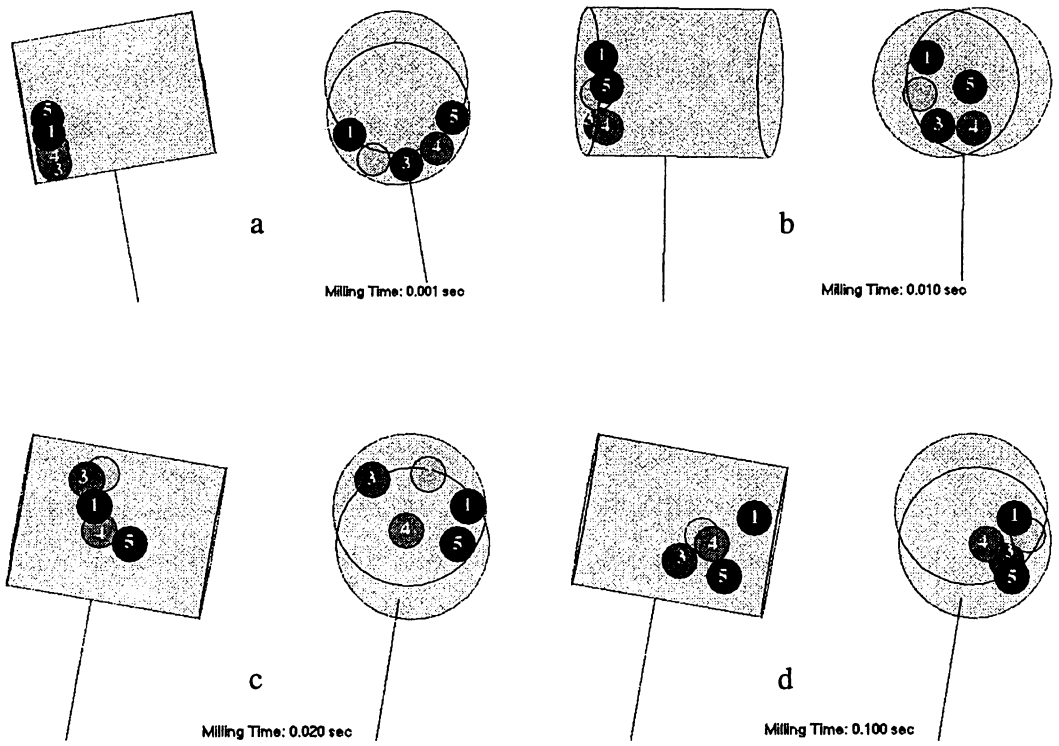

Figure 6-11. Example images showing the positions of the vial and balls at different times after milling starts for five ball mill.

Figure 6-11 shows the positions of balls and vial at different times calculated from a simulation where 5 stainless steel balls with 3.94 mm in radius were placed in the vial. A visualized demonstration program in this condition has been developed by the author and it is available from "http://www.geocities.com/www67/MA-Demo.zip".

Figure 6-12a ~ Figure 6-12c show the position of a selected ball in r direction as a function of time during milling for 1 second for 5, 10 and 15 stainless steel balls with

3.94 mm in radius respectively. It can be seen that the process of multi-ball milling can also be separated into two parts: initial stage and steady state similar to that of using only one ball. During the initial stage, balls slip and roll from their starting positions (Figure 6-11a) on the cylindrical surface of the vial along a spiral route (Figure 6-11b, Figure 6-11c and Figure 6-12), when any of them hits the vial end, it starts a new spiral route. This stage lasts for less than 0.05 second, which is much shorter than that of one ball in the vial. This is explained later in this section. After the initial stage, ball movement is in a steady state typically as shown in Figure 6-11d. At this stage, the larger the number of balls is in the vial, the higher the possibility the balls stay close to the cylindrical wall during milling, as shown in Figure 6-12.

Figure 6-13 shows the impact velocity of each of the impacts which occur in 0.5~1 second for 2, 5 and 10 balls. It can be seen that most of impacts are ball-wall impacts (crosses in Figure 6-13). The frequency of ball-ball impacts increases as the number of balls increases. Among the ball-ball impacts, there are several multi-ball impacts (circles in Figure 6-13). At the very initial stage, there are a large number of impacts and the impact frequency decreases as time increases. The ball-ball impacts influence the motion of balls and cause the balls to fly off after a shorter time than in the case of only one ball being used. After this stage, each ball moves in several different modes: free flying, slipping and rolling on the cylindrical wall, bumping on the ends and cylindrical surface of the vial, and impacting with other balls. At this stage, the impact frequency (shown in Table 6-3 and Figure 6-13) does not change significantly over time. The impact frequency is discussed later in Section 6.4.3.

Table 6-3. Impact frequency in different periods during milling using 5 balls

Time section	0.5~1.5	1.5~2.5	2.5~3.5	3.5~4.5	4.5~5.5	5.5~6.5	6.5~7.5
Impact times	467	439	474	448	465	453	481

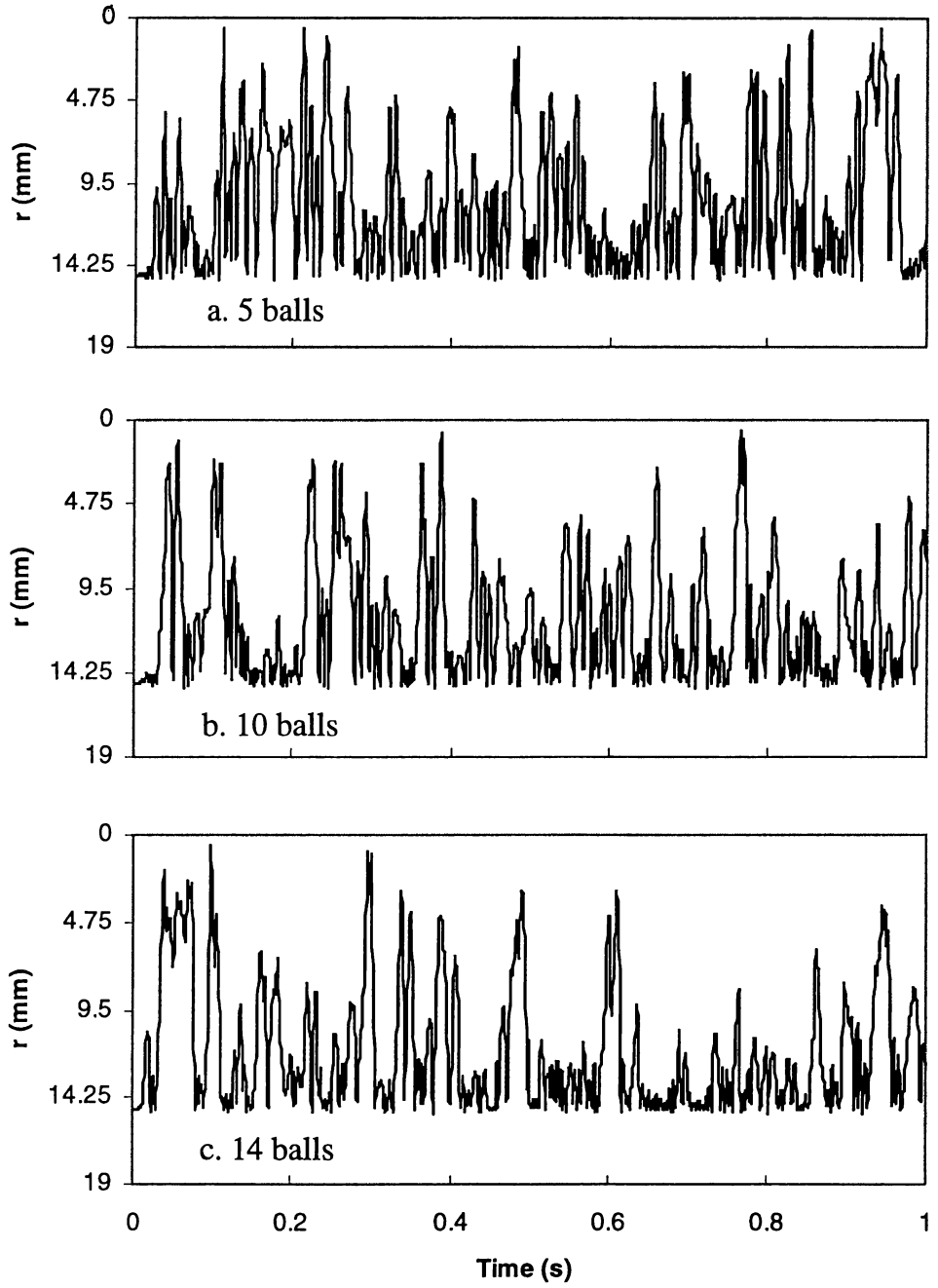

Figure 6-12. Typical position of a selected ball in *r* direction as a function of time for the condition of using 5, 10 and 14 balls respectively

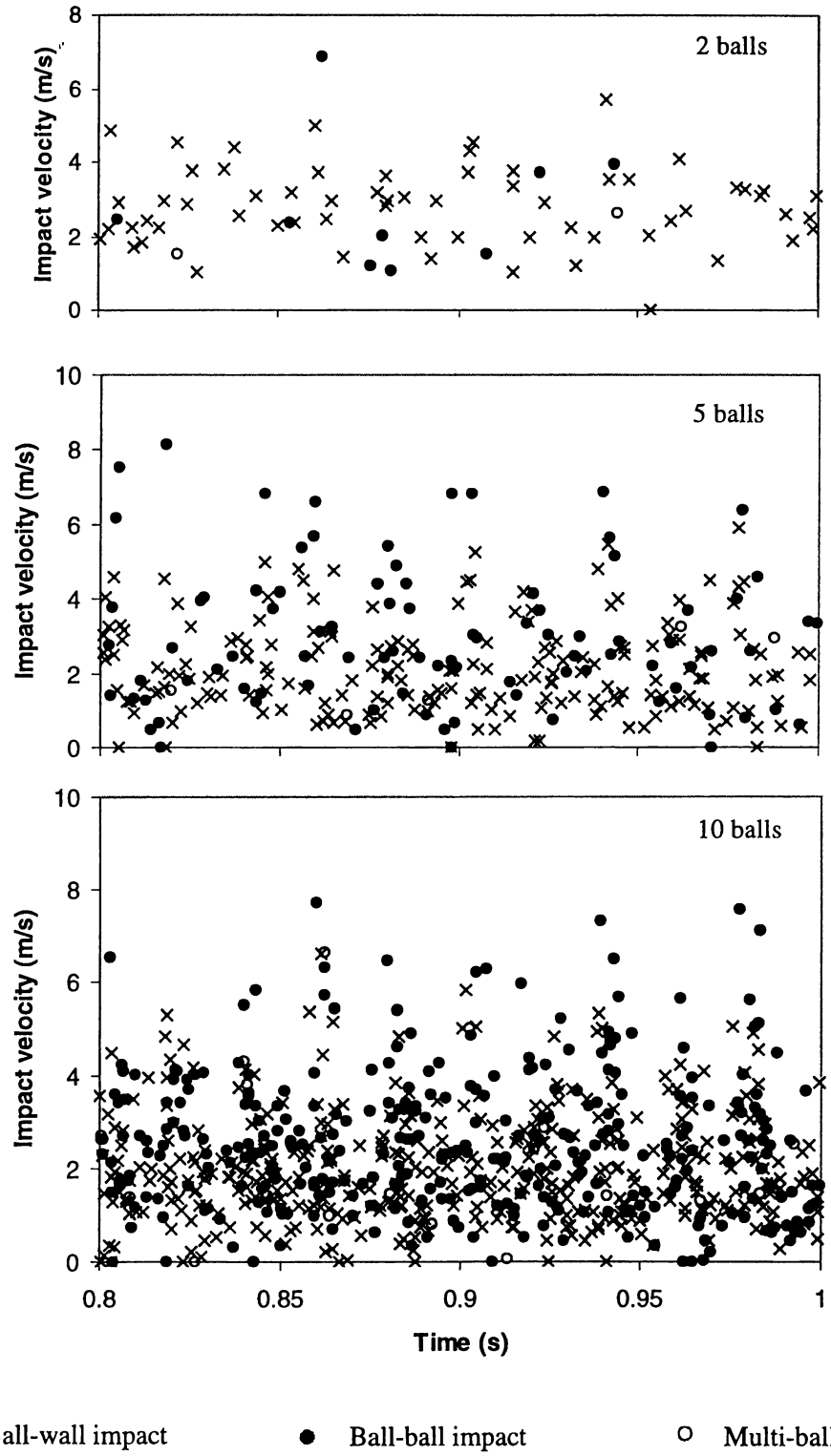

Figure 6-13. The impact velocity of each of the impacts, which occur during milling using 2, 5 and 10 balls respectively

6.4.2 Distribution of Impact Angles

The distribution of impact angles is considered to be important in MA using high-energy ball milling [5,6]. Here the impact angle was defined as follows. When two balls impact each other, they have the velocity of $\vec{v}_1$ and $\vec{v}_2$. Then their relative velocity is $\vec{v} = \vec{v}_1 - \vec{v}_2$. The impact angle is the angle between $\vec{v}$ and the line passing the centers of two balls.

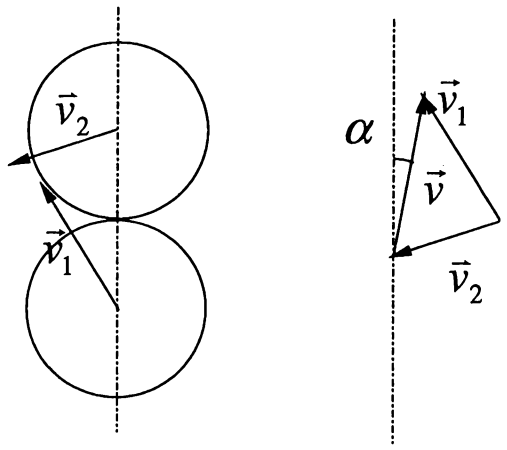

a. Two balls impact with velocities of $\vec{v}_1$ and $\vec{v}_2$

b. The impact angle is the angle between $\vec{v}$ and the line passing the centers of two balls.

Figure 6-14. Definition of impact angle

Figure 6-15 and Figure 6-16 show the distribution of impact angles for different number of balls, predicted by the simulation. It is appears that the majority of the impacts occur at angles in the range of 15~75°.

In order to validate this prediction, the probability for an impact to occur at a particular angle was also determined using geometrical analysis (refer to Appendix III for details). It is assumed that the probability of a ball at any position in the vial is the same. The thin solid lines in Figure 6-15 and Figure 6-16 show the distribution of impact angle based on this geometrical analysis. Comparison of the prediction made using simulation and that made using geometrical analysis shows good agreement for the range of small impact angles and some discrepancy for the range of large impact angles. This discrepancy is likely to be caused by the fact that the balls are close to the cylindrical wall for most of the time.

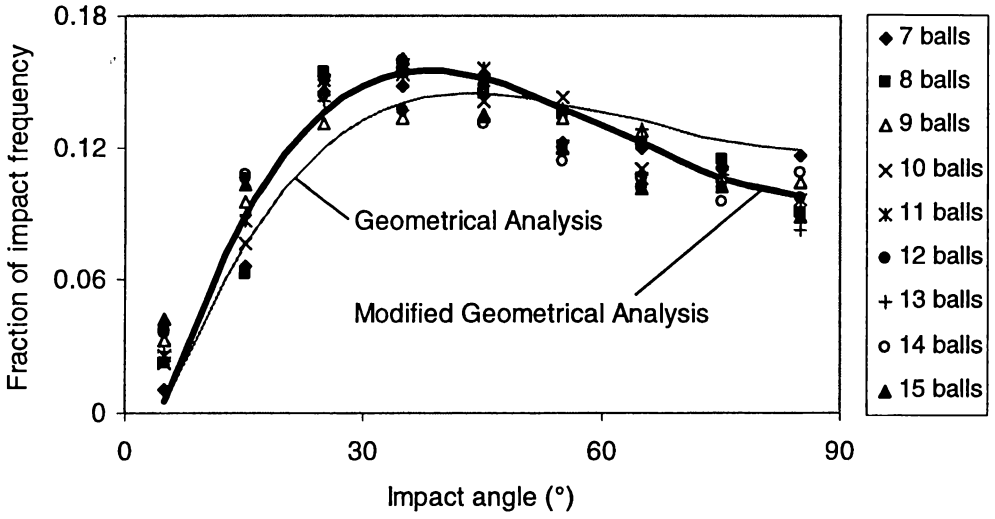

Figure 6-15. The fraction of the impact frequency as a function of impact angle for different number of balls with 3.94 mm in radius

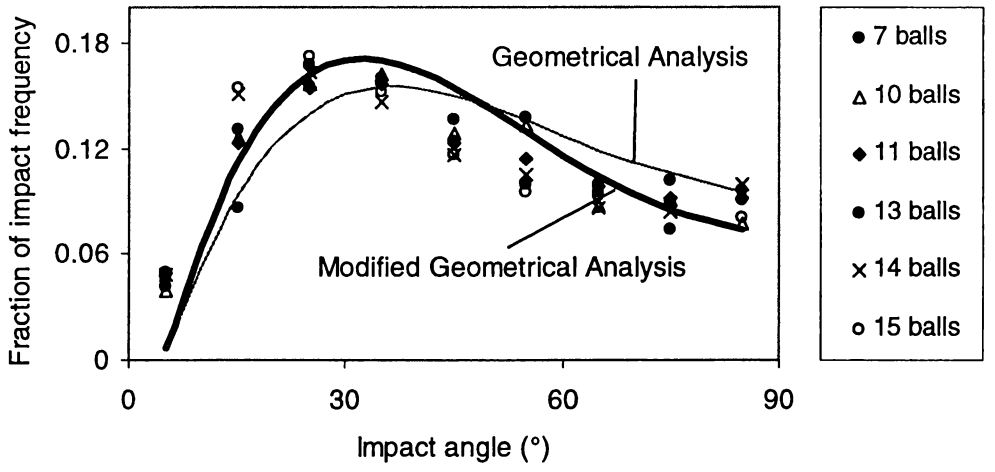

Figure 6-16. The fraction of the impact frequency as a function of impact angle for different number of balls with 4.96 mm in radius

By analyzing the simulation results it can be found that the balls have the tendency of flying close to the cylindrical wall of the vial, especially for large number of balls. If it is assumed that the balls are only in the space between $r = 0.3R_v$ and $r = R_v$ when impacts occur the result of geometrical analysis shows good agreement for the whole range of impact angles with that of simulation (as shown in the thick solid lines).

6.4.3 Frequency of Impacts

Figure 6-17 shows the frequency of ball-wall impacts as a function of the number of balls for different ball masses (refer to Appendix IV for detailed impact number and velocity distribution). The balls are stainless steel balls. For a given ball size, the results show that the ball-wall impact frequency is almost linearly proportional to the number of the small balls (with 3.94 mm and 4.96 mm in radii) for the whole range of 1~15. For big balls, the impact frequency is initially almost linearly proportional to the number of balls, but start to rapidly increase with the increasing number of balls.

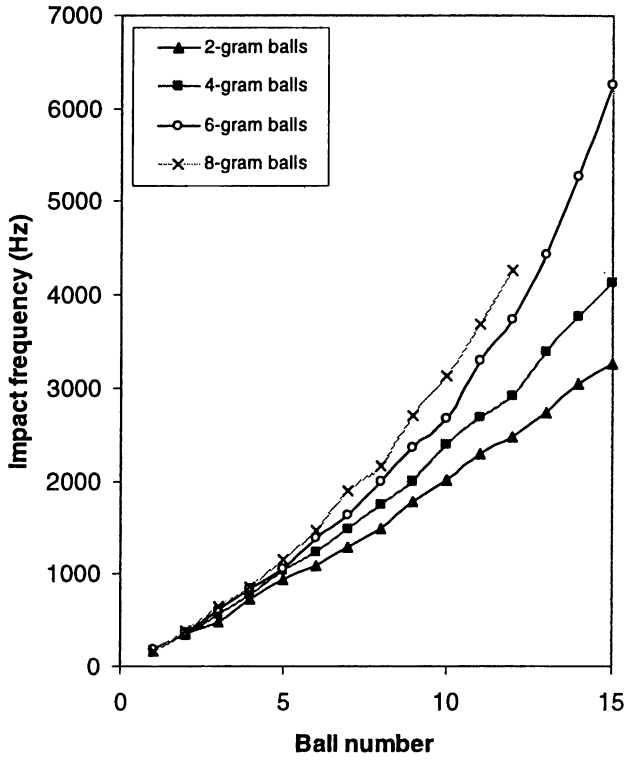

Figure 6-17. The frequency of impacts of ball-wall as functions of ball number for different size of balls

The relationship of the impact frequency and number of balls can be roughly understood based on geometrical analysis. For small balls such as balls with 5.68 mm and 6.26 mm in radii, the balls move in a normal manner and so the number of impacts on the wall is strictly proportional to the number of balls. For a small number of big balls with a mass with 4.96mm in radius, the balls could move freely and thus the results are as the above. However, when the number of balls is increased, the traffic is very heavy, and thus the number of impacts on the wall increases sharply. In

this case, most of balls are rolling or slipping on the wall. This motion is very ineffective from the point of view of high-energy ball milling.

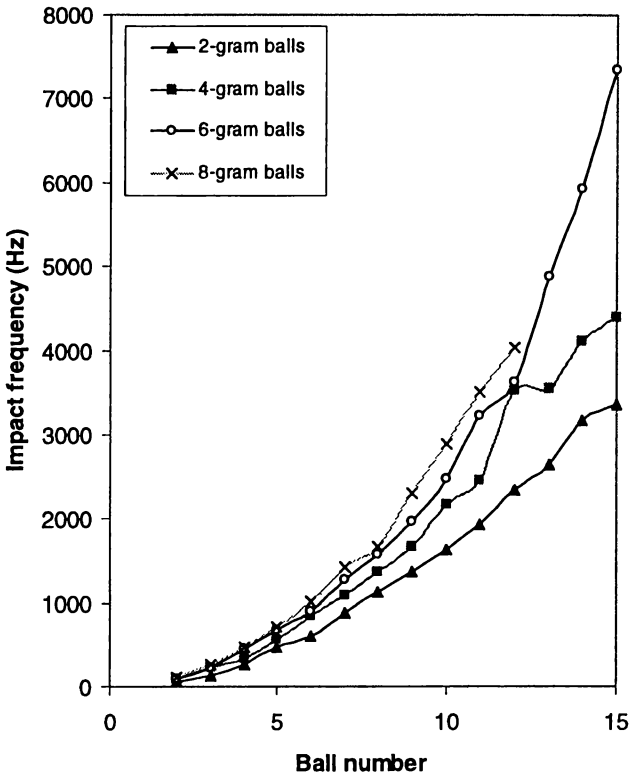

Figure 6-18. The frequency of impacts of ball-ball as functions of ball number for different size of balls

Figure 6-18 shows the frequency of ball-ball impacts as a function of the number of balls for different ball masses (refer to Appendix IV for detailed impact number and velocity distribution). The balls are stainless steel balls. For a given ball size, Figure 6-18 shows that the frequency of ball-ball impacts is roughly proportional to the square of the number of balls. For a given number of balls, the frequency of ball-ball impacts also increases with increasing size of the balls. These results disagree with that of Davis et al.'s simulation [5]. Having not known the detailed models used by Davies et al., it is difficult to comment why the results are different. However, a probabilistic method has been developed to support the simulation result.

Since a ball flies with a space of $\left(\pi r_b^2 v\Delta t + V_b\right)$ within a unit time Δt, the impact probability between one ball and others in a unit time is $\xi(n-1)\left(\pi r_b^2 v\Delta t + V_b\right)/V$, where ξ is used to adjust the probability so that the total value is 1. Then the total impact probability is $\xi\left(\pi r_b^2 v\Delta t + V_b\right)n(n-1)/2V$. Because the average velocity v

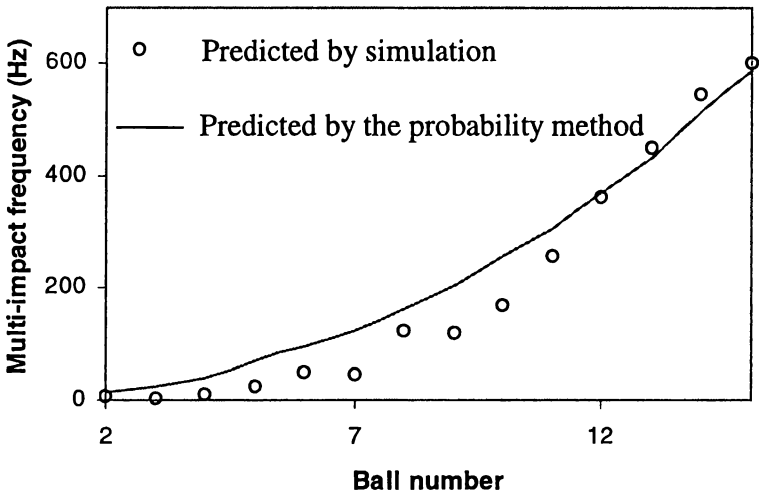

Figure 6-19. Multi-ball impact frequency for different ball numbers for balls with 3.94 mm in radius

does not change very much for SPEX mill and distance for a ball to travel in a unit time (1 second) is very large compare to ball dimension, the volume of ball, V_b, can be ignored. Then the frequency of impacts is proportional to $n(n-1)$, r_b^2 and v. This agrees with the results of prediction as shown in Figure 6-18.

Impacts also happen between more than two balls. These events have been defined as multi-ball impacts in Chapter 4. The simulation has proven that multi-ball impacts do occur during milling. In Figure 6-19, the small circles show multi-ball impact frequency for different number of balls. It can be seen that using a larger number of balls causes more multi-ball impacts. This can also be predicted by probabilistic method. By using the impact model in Chapter 3, it can be calculated that an impact roughly lasts for about 0.2 ms. Using the result of 10 balls as an example, there are 3140 impacts (including impacts of ball-wall and ball-ball) per second. These impacts will last 0.628 second in total. Then the two impacting balls will impact with the rest of the objects (balls or wall). The total impact frequency would be the number of impacts for 9 balls, and the number of multi-impact is one ninth of these impacts. Using this method, the predicted number of the multi-impact is around 190, which is higher than that predicted

by the simulation. However, with a larger number of balls, the agreement between the predictions made by the two methods agrees very well, as shown in Figure 6-19.

6.4.4 The Distribution of Impact Velocity

Figure 6-20 shows the mean impact velocity in $o'-x'y'z'$ system as a function of ball number for balls with 3.94 mm in radius. It can be seen that the mean impact velocity decreases as increasing ball number.

For a given size and number of balls, impact velocity is one of the most important factors in MA. From the simulation, we have calculated every impact during milling and thus can determine the distribution of the impact velocity. Figure 6-21 show the fraction of impacts as a function of impact velocity (The exact numbers of impacts are given in Appendix IV). It can be seen that a large part of the impacts occur at a velocity less than 4 m/s and only a very small fraction of the impacts occur at a velocity of over 6 m/s. The larger the number of balls, the more impacts occurred at low velocities. By comparing the three figures in Figure 6-21, we can also see that the larger balls cause lower impact velocity for the same number of balls. However, the above does not provide quantified understanding about the milling efficiency.

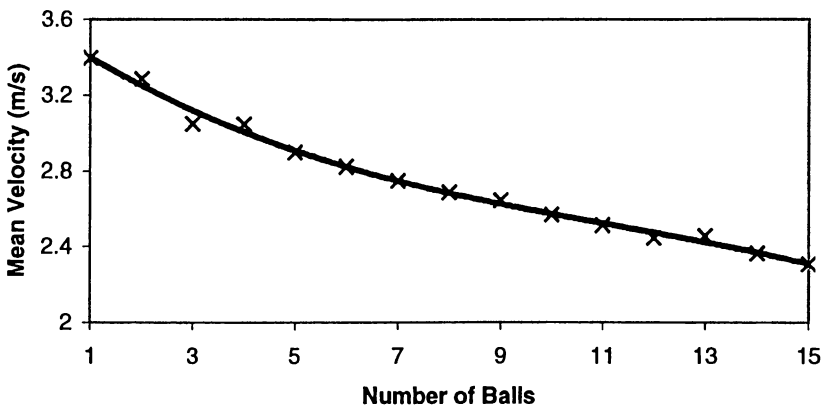

Figure 6-20. The mean impact velocity in $o'-x'y'z'$ system as a function of ball number for balls with 3.94 mm in radius

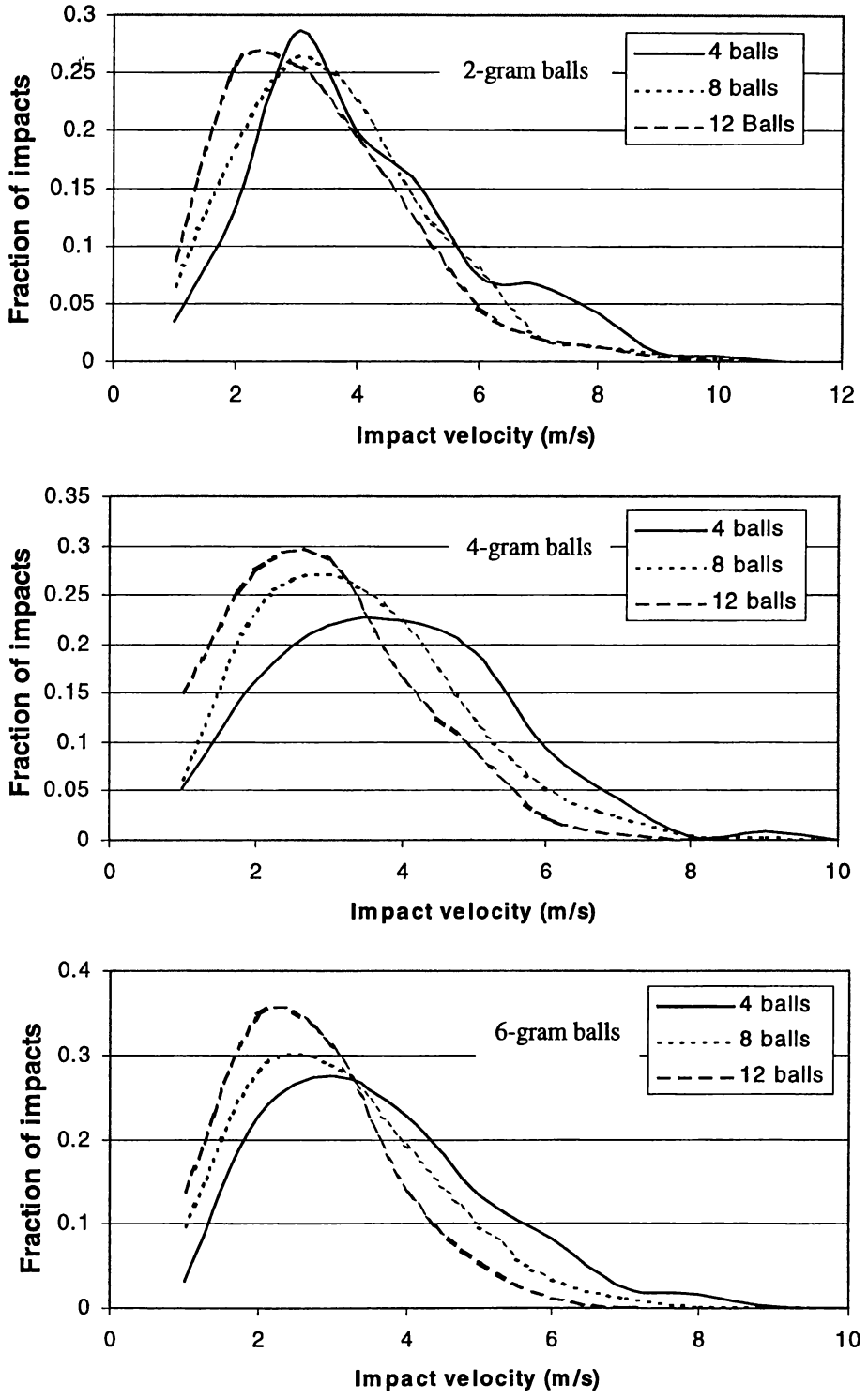

Figure 6-21. Fraction of impacts as a function of impact velocity for different numbers and size of balls

It has been well accepted that MA is distinguished from conventional ball milling by high milling energy [7,8]. Thus there should exist a critical velocity, below which the milling process is similar to a conventional ball milling and there is no mechanical alloying effect. Calka and Radlinski [6] showed that the impacts could be separated by energy level. They found that milling under different impact energy level generated different outputs and that it was difficult to mechanically alloy some powder at low energy level, even though the powder was milled for a very long time. The lowest energy level they used was 1.5 m/s for the steel balls of 33.48 mm in radius (calculated from their provided data) [6]. Thus it is assumed that 1.5 m/s is the critical impact velocity for 33.48 mm balls as a provisional option, although the real critical velocity might be lower. The critical impact velocities, which are needed to quantify in further work, for different size of balls are determined by using the single impact model deduced in Chapter 3 based on the following consideration.

As described in Chapter 3, the impact pressure can be separated into two components: the part that causes visco-plastic flow and that causes elastic deformation of powder. The first part contributes mostly to the strain rate hardening. It exists in dynamic pressing process. The last part supplies the strain hardening to the powder particles. This part parallels the pressing pressure in static pressing process and it can be imagined that only the last part, which inheres inside the powder particles, is the potential power for the powder deformation. Thus it was assumed that the critical velocity is achieved when only the maximum elastic pressure during impact reaches the value as that of the impact at 1.5 m/s for the two balls with a radius of 33.48 mm (as shown in Figure 6-22). The calculated critical impact velocity for different size of balls is shown in Figure 6-23.

By assuming the critical velocity for MA was as that shown in Figure 6-23, the frequency of effective impacts was determined for different ball sizes and numbers (Table 6-4). It can be seen that within one second there is only a small fraction of total impacts, which are effective for the purpose of MA, although the frequency of impacts is very high.

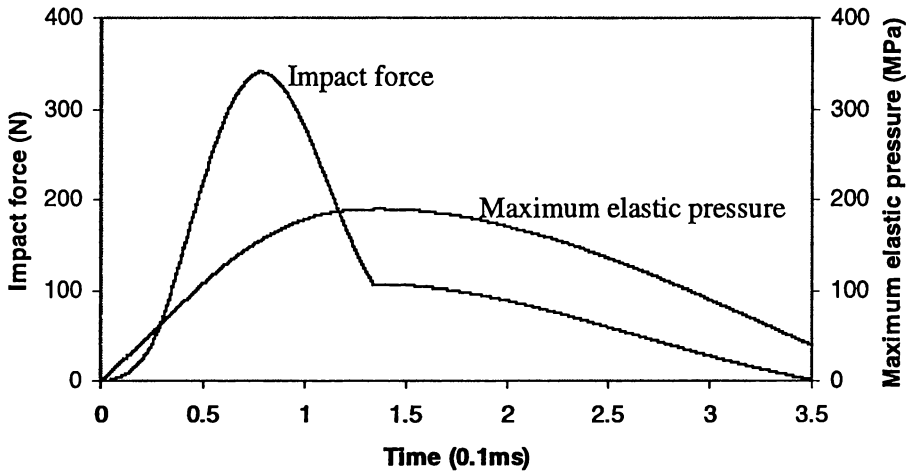

Figure 6-22. Impact force and maximum elastic pressure for impact at a velocity of 1.5 m/s between two balls with a radius of 33.48 mm

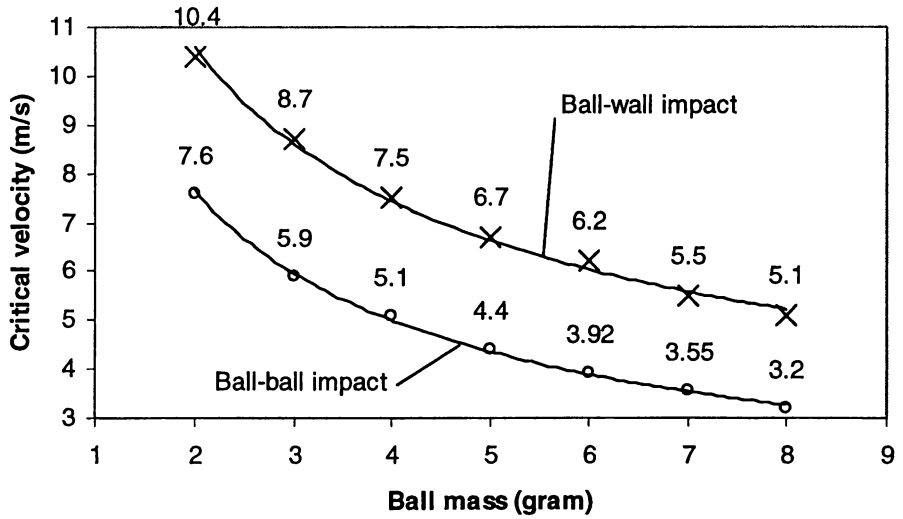

Figure 6-23. The calculated critical impact velocity for different size of balls between ball and ball and between ball and wall.

Table 6-4. Effective impact frequency/impact frequency for different conditions

Ball mass (g) / Ball number	2	3	4	5	6	7	8
1	0/165	0/147	1/165	1/187	2/175	5/189	9/167
2	3/400	5/397	25/443	32/470	34/464	67/494	72/500
3	6/608	14/699	27/776	52/775	73/832	114/821	152/900
4	3/985	30/1094	661119	92/1231	123/1290	160/1294	202/1318
5	14/1410	37/1484	82/1579	133/1661	141/1728	211/1821	258/1855
6	10/1688	46/1824	78/2077	141/2141	198/2282	242/2293	283/2476
7	12/2161	42/2373	87/2563	193/2807	203/2903	259/3040	324/3315
8	15/2609	53/2971	113/3119	181/3333	252/3560	308/3805	352/3821
9	15/3151	69/3366	108/3671	200/4206	258/4324	354/4655	356/5010
10	14/3650	68/4187	136/4573	197/5102	253/5150	323/5529	369/6010
11	19/4211	62/4619	100/5141	251/5703	265/6523	342/6520	355/7180
12	15/4810	65/5538	108/6438	188/6645	287/7350	391/7905	366/8299
13	21/5386	66/6162	91/6942	212/7817	258/9298	349/9883	
14	12/6212	73/7136	95/7876	217/9095	137/6182	304/11939	
15	11/6609	67/7720	98/8507	186/10099	240/13613		

Table 6-5. Powder volume per second could be mechanically milled (%)

Ball mass (g) / Ball number	2	3	4	5	6	7	8
1	0.000000	0.000000	0.001639	0.002050	0.006324	0.013501	0.030130
2	0.003338	0.018418	0.033331	0.041658	0.034332	0.085264	0.107092
3	0.009131	0.018138	0.050062	0.062573	0.051940	0.120920	0.177532
4	0.015271	0.036025	0.072843	0.091046	0.076020	0.160480	0.204921
5	0.022829	0.047243	0.112367	0.140423	0.094503	0.210381	0.159252
6	0.024223	0.044423	0.114077	0.142574	0.111795	0.203592	0.159919
7	0.025976	0.053281	0.147367	0.184166	0.105876	0.162268	0.151891
8	0.031245	0.066769	0.136554	0.170660	0.119400	0.153780	0.131840
9	0.038624	0.062424	0.139487	0.216949	0.117981	0.173551	0.110883
10	0.037569	0.079000	0.130338	0.174332	0.106967	0.140399	0.116122
11	0.039667	0.059325	0.173605	0.162894	0.103229	0.146693	0.071073
12	0.038445	0.056791	0.108272	0.135326	0.094265	0.130808	0.074196
13	0.039315	0.050187	0.129086	0.161326	0.084841	0.121522	
14	0.035286	0.048500	0.134885	0.168574	0.038558	0.097054	
15	0.032651	0.052291	0.109083	0.136334	0.080961		

6.4.5 Milling Time

The milling time is used to evaluate the milling efficiency by varying ball number and size. An assumption is taken that when the elastic pressure reaches the critical elastic pressure, the powder is mechanically milled. Thus the amount (in percentage) of powder mechanically milled at a specific velocity for different size of balls is determined by using the thickness of powder involved in an impact in Chapter 4 and the single impact model in Chapter 3. Supposing there is 6-gram stainless steel powder inside the vial and considering the effective impact frequency at different velocities as listed in Appendix IV, the powder volume per second, which could be mechanically milled, or milling speed is achieved in Table 6-5 and Figure 6-24. The milling time (as shown in Table 6-6) needed to mechanically mill 95% of the powder is solved according to the model introduced in Appendix V.

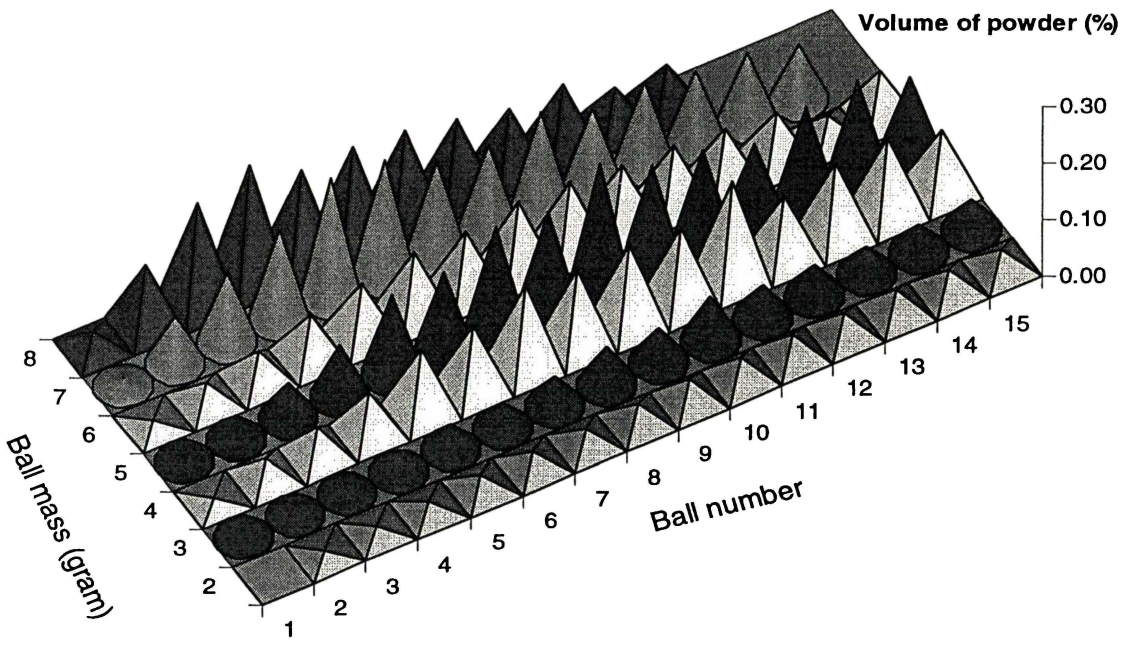

Figure 6-24. Powder volume mechanically milled (%) per second for different number and size of balls

Table 6-6. Time needed for milling 95% of the powder (min)

Ball mass (g) / Ball number	2	3	4	5	6	7	8
1	#	#	3046.039	2435.055	789.4825	369.8062	165.6857
2	1495.810	271.0648	149.7725	119.8302	145.4034	58.53270	46.59759
3	546.7554	275.2519	99.70922	79.76808	96.10396	41.26588	28.09883
4	326.9334	138.5699	68.51832	54.81414	65.65384	31.08732	24.33999
5	218.6872	105.6611	44.40891	35.53119	52.80805	23.70767	31.32721
6	206.0940	112.3684	43.74260	34.99457	44.63634	24.49906	31.19633
7	192.1888	93.68433	33.85577	27.08576	47.13303	30.74448	32.84665
8	159.7742	74.75342	36.53843	29.23137	41.79150	32.44276	37.84598
9	129.2447	79.95856	35.76973	22.98913	42.29429	28.74405	45.00365
10	132.8748	63.17614	38.28241	28.61519	46.65214	35.53722	42.97203
11	125.8454	84.13734	28.73516	30.62626	48.34200	34.01133	70.22557
12	129.8460	87.89143	46.08940	36.87018	52.94167	38.14451	67.26837
13	126.9713	99.46048	38.65386	30.92410	58.82479	41.06133	
14	141.4729	102.9205	36.99083	29.59342	129.4645	51.41933	
15	152.8899	95.45747	45.74671	36.59757	61.64531		

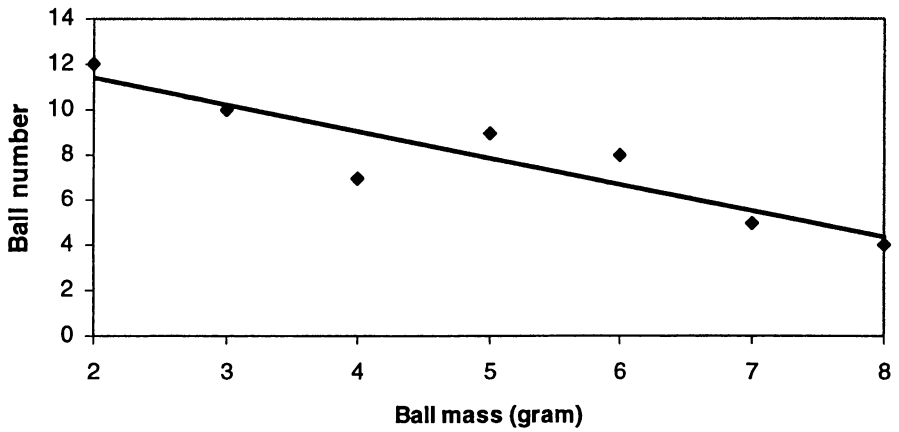

Figure 6-25. The number and size of milling balls that could reach the best milling efficiency

It can be seen that the milling time and milling speed changes while varying the number and size of milling balls. For one of balls with 3.94 mm and 4.96 mm in radii, the powder might never be mechanically milled. Even if a large ball is used, the milling still takes a very long time when one ball is used. When more than one ball are used, there exits an optimum number of balls for best efficiency for a given size of balls. Figure 6-25 shows the optimum number of balls as a function of ball mass. It appears there is a linear relationship between the number of balls and ball mass for best efficiency. Therefore, when larger balls are used, the number should be smaller.

6.5 Discussion

In this work a set of more comprehensive models have been developed to well predict all impact events during milling (global model) and to describe each impact process (local model). The head-on impact model, which is the basic part of the local model, has been deduced theoretically. Comparison of the calculated results with the experimental data from someone else in literature [9] has shown that it best simulates the impact process. Based on this model, other forms of impact have been considered and combined with the powder volume model which has been deduced to determine the volume of powder trapped during each impact. The combined model (local model) is able to describe any impact process during ball milling.

SPEX-8000 Mixer/Mills involve complex movement in 3 dimensions. This movement is determined by the structure of the machine. In this work, a 3-D global model has been developed based on the mechanism of the machine and combined with models for ball positions, velocities and impacts. Comparing with the former studies on this machine, the current global model better describes the mechanics of the SPEX machine.

Due to the complexity of the milling process and the difficulty of deriving analytical solutions of mathematical equations, numerical calculation was used to solve the

equations. This enables the simulation of a milling process to be more accurate at a cost of long computation time (in days) when personal computer is used to handle the calculation.

The above models have been employed to predict the trajectories of balls, the impact angle distribution, impact velocity distribution and impact pressures and forces. The results on milling process are quite different from those of previous studies. This is hardly surprising, as previous studies on milling process used heavily simplified models. Considering it is difficult to do experiments to validate the models on milling dynamics, probability analysis has been used as an option to validate the models. The comparison has shown good agreement between the results from simulation and the probability analysis, indicating that the models are reasonable.

The present work has demonstrated that the set of models can be used as a package which can be used to achieve the following:

- To visualize the motion of balls and the impacts during milling.
- To evaluate the milling efficiency under different milling conditions.
- To optimise the milling parameters such as the number and size of balls, vial size and shape.

At this point, the package is not able to adequately predict the milling time required to achieve a particular outcome such as formation of a composite microstructure with a certain degree of fineness. It is necessary to develop a micro-mechanics model which describes the elastic and plastic deformation, and fracturing and cold welding of each powder particles. This will be a challenging task. Undoubtingly the work presented in this thesis provides a good basis and staring point to complete this task.

6.6 Summary

The motion of the vial of SPEX 8000 Mixer/Mills has been simulated. It has been shown that the motion of vial involves a complex movement in 3 directions and this motion is affected by the springs, which balance the vial and the fulcrums. The milling dynamics of SPEX 8000 Mixer/Mills have been studied for the simulations when one ball or multi balls were put in the vial. The balls inside the vial have been shown to undergo a random movement, which can be separated into two stages. The early unstable stage lasts for less than 0.3 second. It involves mostly rolling and slipping of balls on the vial wall. The second stage is the stable stage, when the impact frequency, the mean impact velocity and mean spinning velocity of balls do not change significantly over time. The frequency of impacts in ball milling using multi balls is high. The majority of impacts happen at low velocities of less than 4 m/s and with angles in the range of 15~75°. A substantial fraction of impacts are multi-ball impacts. For different number of balls, the simulation results indicate that the frequency of impacts between balls and the vial wall is proportional to the number of balls and the number of impacts between balls is nearly proportional to the square of the number of balls and the square of radius of balls. By considering the powder compact deforms under a certain pressure, the critical velocities for mechanical milling for various sizes of balls have been determined. Based on these critical velocities, the effective impact frequency and the milling time for different number and the size of balls have been calculated. It has been shown that for a given radius of balls, there is an optimum number for the best milling efficiency.

6.7 References

1. Maurice, D.R., Courtney, T.H., "The physics of mechanical alloying: a first report", *Metallurgical Transactions A.*, **21A**, 1990, 289.

2. Maurice, D, Courtney, T. H., "Milling dynamics: part II, dynamics of a SPEX mill and a one-dimensional mill", *Metallurgical and materials Transactions A*, **27A**, 1996, 1973.
3. Maurice, David R., "The physics of mechanical alloying: a first report", *MSc Thesis*, University of Virginia, 1988.
4. Caravati, C., Delogu, F., Cocco, G. and Rustici, M., "Hyperchaotic qualities of the ball motion in a ball milling device", *Chaos*, **9**(1), 1999, 219-226.
5. Davis, R. M., McDermott, B. and Koch, C. C., "Mechanical alloying of brittle materials", *Metallurgical Transactions A*, 19A, 1988, 2867.
6. Calka, A., Radlinski, A. P., "Universal high performance ball-milling device and its application for mechanical alloying", *Materials Science and Engineering*, **A134**, 1991, 1350.
7. Benjamin, J.S., "Mechanical Alloying", *Scientific America*, **234**, 1976, 40.
8. Benjamin, J.S., "Dispersion strengthened superalloys by mechanical alloying", *Metallurgical Transactions*, **1**, 1970, 2943.
9 Huang, H., Dallimore, M.P., Pan, J., McCormick, P.G., "An investigation of the effect of powder on the impact characteristics between a ball and a plate using free falling experiments", *Materials Science and Engineering A*, **241**, 1998, 38.

Chapter Seven

Global Models for Planetary and Attritor Mills

7.1 Introduction

This chapter describes the 4 dimensional global models of a typical planetary mill and a typical attritor mill respectively. The models are then coupled with the local model described in Chapter 4 to numerically simulate the milling process.

7.2 Planetary Mills

7.2.1 The Model for the Motion of Vial

The motion of a planetary mill involves rotation of the vial about two separate parallel axes, analogous to the rotation of the earth about the sun. A diagram of the mill motion is given in Figure 7-1. The planetary arm rotates about point O, with an angular velocity ω_p. The vial is centered at point A, which is at a distant R_p from O. The vial rotates in the opposite direction to the planet arm with an angular velocity ω_v.

Here it is assumed that the side wall of the vial has a curvature of $\frac{1}{R}$ as shown in Figure 7-2. Two Cartesian coordinate systems were employed: one is $O-XYZ$ and

another one is $o-xyz$. OX was the central axis of the starting position of OA in Figure 7-1 and OZ was perpendicular to XOY plane passing point O. o was the central of the vial bottom, ox was the line parallel OX and oz was the line parallel OZ. If the mill is at the position of the solid lines as depicted in Figure 7-1 at the starting moment, then after it runs for a period of time, t, the mill's position will be at the dash lines in Figure 7-1. Then, the position of any point attached to the system $O-XYZ$, (X_b, Y_b, Z_b), was determined by

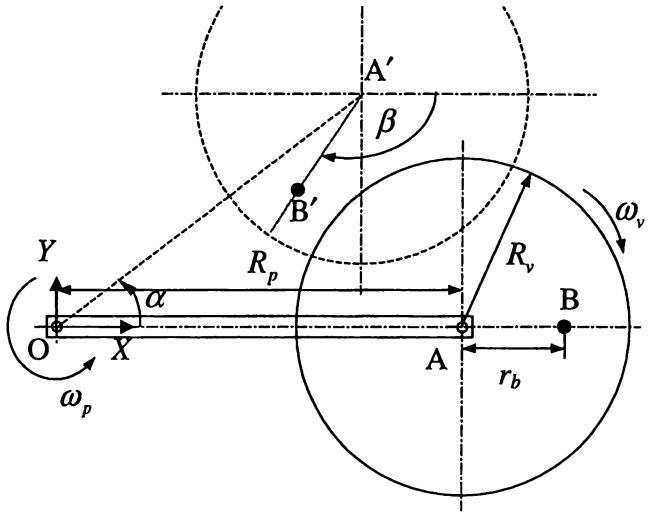

Figure 7-1. Schematic Representation of Planetary Mill Motion

$$X_b = R_p \cos\alpha - r\cos\beta \tag{7-1a}$$

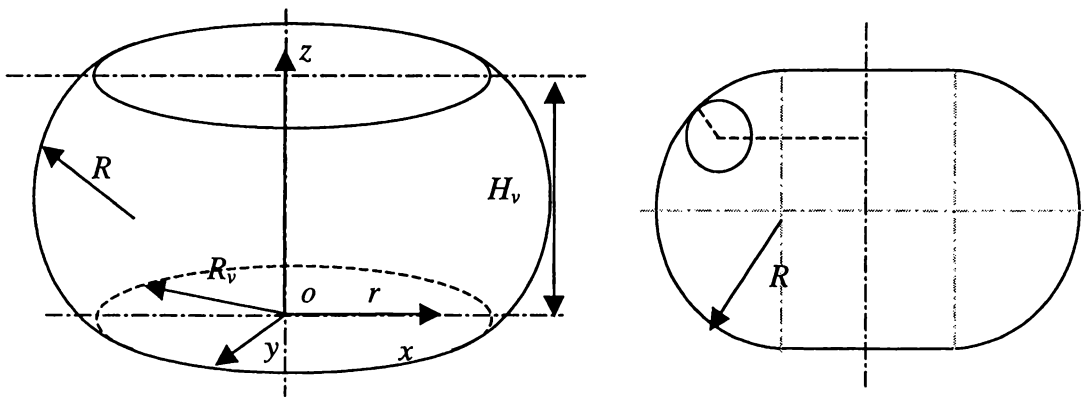

Figure 7-2. The geometry of the planetary vial

$$Y_b = R_p \sin\alpha - r\sin\beta \tag{7-1b}$$

$$Z_b = Z_b \tag{7-1c}$$

where r is the distance from point B to axis OX, α is the angle OA rotated about point O and β is the angle the vial rotated about point A during the period, t. α and β can be calculated by the following equations:

$$\alpha = \omega_p t \tag{7-2}$$

$$\beta = \omega_v t - \alpha = (\omega_v - \omega_p)t \tag{7-3}$$

then equation (7-1) can be expressed by

$$X_b = R_p \cos(\omega_p t) - r\cos[(\omega_v - \omega_p)t] \tag{7-4a}$$

$$Y_b = R_p \sin(\omega_p t) - r\sin[(\omega_v - \omega_p)t] \tag{7-4b}$$

$$Z_b = Z_b \tag{7-4c}$$

The velocity of point B was calculated by differentiating equations (7-4a~c) with respect of time t:

$$v_{bx} = -R_p\omega_p \sin(\omega_p t) + r(\omega_v - \omega_p)\sin[(\omega_v - \omega_p)t] \tag{7-5a}$$

$$v_{by} = R_p\omega_p \cos(\omega_p t) - r(\omega_v - \omega_p)\cos[(\omega_v - \omega_p)t] \tag{7-5b}$$

$$v_{bz} = 0 \tag{7-5c}$$

Then the position of any point (x, y, z) in the vial attached to $o-xyz$ was converted to a point relative in the earth attached to $O-XYZ$ by

$$X = (x + R_p)\cos\alpha - y\sin\alpha \tag{7-6a}$$

$$Y = (x + R_p)\sin\alpha + y\cos\alpha \tag{7-6b}$$

$$Z = z \tag{7-6c}$$

Any point (X,Y,Z) in the earth attached to $O-XYZ$ can be converted to a point relative in the vial attached to $o-xyz$ by

$$x = X\cos\alpha + Y\sin\alpha - R_p \tag{7-7a}$$

$$y = -X\sin\alpha + Y\cos\alpha \tag{7-7b}$$

$$z = Z \tag{7-7c}$$

The velocity of any point (X,Y,Z) attached to $O-XYZ$ is

$$v_x = -R_p\omega_p \sin(\omega_p t) + \sqrt{X^2+Y^2}(\omega_v - \omega_p)\sin\left[\tan^{-1}\left(\frac{Y}{X}\right) + \omega_p t\right] \tag{7-8a}$$

$$v_y = R_p\omega_p \cos(\omega_p t) - \sqrt{X^2+Y^2}(\omega_v - \omega_p)\cos\left[\tan^{-1}\left(\frac{Y}{X}\right) + \omega_p t\right] \tag{7-8b}$$

$$v_z = 0 \tag{7-8c}$$

7.2.2 Dynamics of Balls Inside the Vial

7.2.2.1 Impacts between Balls

Impacts between balls can be determined by using the same method as introduced in Section 5.3.3.

7.2.2.2 Impacts between Balls and Wall

The position of line A in the vial can be determined from equations (7-4a~c) by substituting r with zero:

$$X_a = R_p \cos(\omega_p t) \tag{7-9}$$

$$Y_a = R_p \sin(\omega_p t) \tag{7-9}$$

Then when a ball's position attached to the system $O-XYZ$ (Figure 7-1 and Figure 7-3) is (X,Y,Z), the ball is contacting or impacting with the curved wall of the vial if either of the following equations is satisfied.

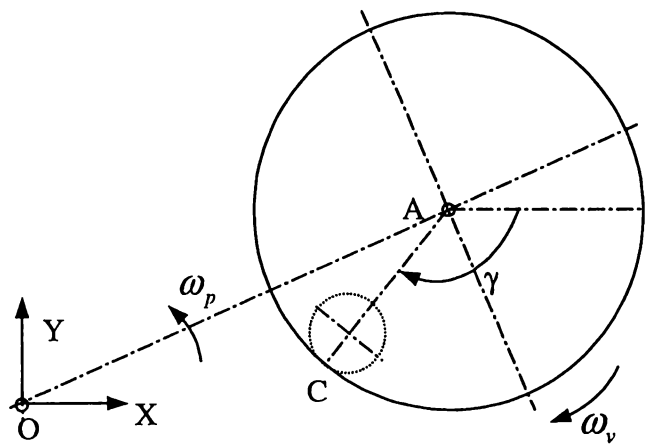

Figure 7-3. The location of a ball in the vial

$$d_1 = \sqrt{(X - X_a)^2 + (Y - Y_a)^2} > R_v \tag{7-10a}$$

$$d_2 = \sqrt{\left(X - \frac{X - X_a}{d_1} R_v - X_a\right)^2 + \left(Y - \frac{Y - Y_a}{d_1} R_v - Y_a\right)^2 + (Z - R_v)^2} \geq R - R_b \tag{7-10b}$$

The contact point C on the wall is:

$$X_c = X_a + \left(R_v + R\sqrt{1 - \left(\frac{Z - R}{d_2}\right)^2}\right)\frac{X - X_a}{d_1} \tag{7-11a}$$

$$Y_c = Y_a + \left(R_v + R\sqrt{1 - \left(\frac{Z - R}{d_2}\right)^2}\right)\frac{Y - Y_a}{d_1} \tag{7-11b}$$

$$Z_c = R + \frac{Z - R}{d_2} R \tag{7-11c}$$

Its velocity was determined by replacing (X, Y, Z) with (X_c, Y_c, Z_c) in equation (7-8).

It can also be determined that if any ball at position (X, Y, Z) is contacting or impacting with the bottom or the top of the vial if either of the following equations is satisfied:

$$Z \leq R_b \tag{7-12a}$$

$$Z \geq H_v - R_b \tag{7-12b}$$

The contact point E can be determined by

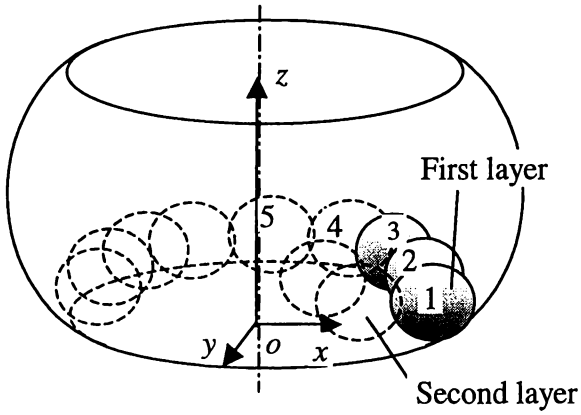

Figure 7-4. Ball original positions in planetary mill

$$X_e = X \tag{7-13a}$$

$$Y_e = Y \tag{7-13b}$$

$$Z_e = \begin{cases} 0 & when\ Z \le R_b \\ H_v & when\ Z \ge H_v - R_b \end{cases} \tag{7-13c}$$

Its velocity was determined by replacing (X, Y, Z) with (X_e, Y_e, Z_e) in equation (7-8).

7.2.2.3 Free Movement of Balls

Free movement of balls was calculated by using the same method as described in Section 5.3.2.

7.2.2.4 The Initial Positions and Velocities of Balls

The first ball was put in the bottom of the vial close to the cylindrical wall as shown in Figure 7-4. The rest of balls were lined along the same layer close to the cylindrical wall. If they formed a circle, then started a new layer.

Similar to those in SPEX 8000 Mixer/Mill, the initial velocities of balls in planetary mill were assumed to be the same as those of the vial at the points where the balls and vial are in contact. This can be calculated by differentiating equations (7-8a~c) and setting $t = 0$.

7.3 Attritor Mills

As introduced in Section 2.3.2, an attritor mill functions by agitating the milling balls and powders by its impellers, which rotate at a certain speed. The model introduced here was developed for vertical attritors. While, for horizontal attritors, typically Zoz mills, the model can be slightly modified by changing the gravitational acceleration from vertical to horizontal.

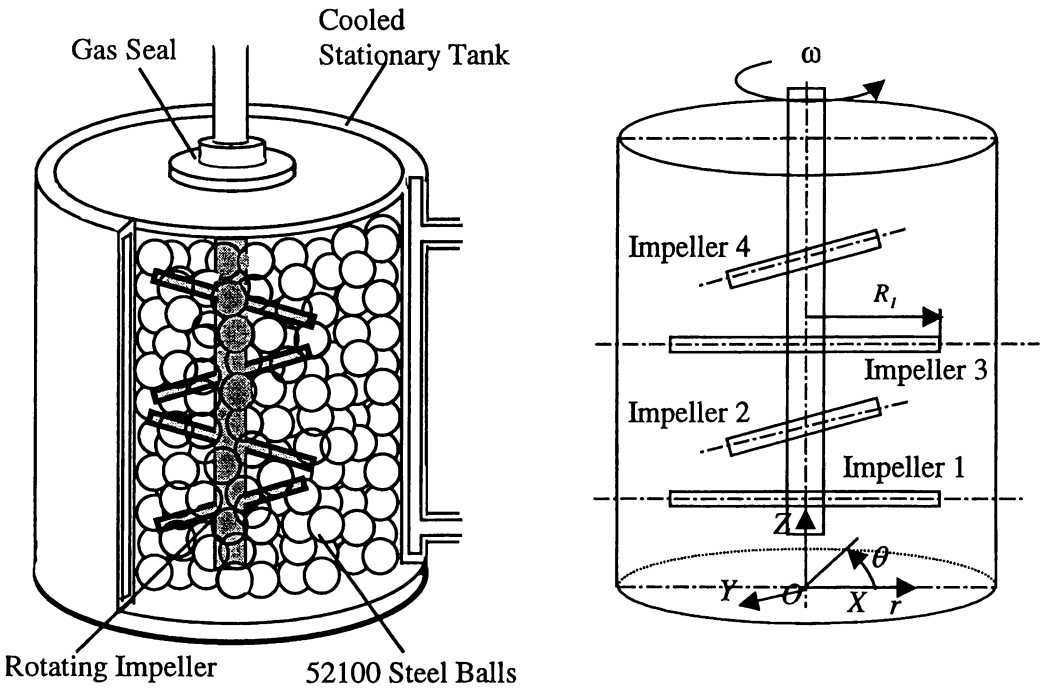

Figure 7-5. Schematic representation of an Attritor mill

7.3.1 The Model for the Motion of the Impellers of the Container

A Cartesian coordinate system, $O-XYZ$, and a cylindrical coordinate system, $O-r\theta Z$, were employed as shown in Figure 7-5. OX was the central axis of the starting position of first impeller and OZ was the central line of the container.

If the distance between the impellers is d, the impeller 1's position is $Z=d_0$ and $\theta=0$, then at any moment the position of any point in impeller i can be determined by

$$Z_i = d_0 + d(i-1) \tag{7-14a}$$

$$\theta_i = \omega t + \frac{\pi}{2}k, \quad \begin{cases} k=1, & i \ \ is \ \ odd \\ k=0, & i \ \ is \ \ even \end{cases} \tag{7-14b}$$

$$R_{di} < r \le R_i \tag{7-14c}$$

where R_{di} is the radius of the center shaft, whose rotating velocity is ω.

The position of any point in impeller i contacted to $O-XYZ$ can be written by

$$X_i = r\cos\theta, \quad (R_d < r \le R_i) \tag{7-15a}$$

$$Y_i = r\sin\theta, \quad (R_d < r \le R_i) \tag{7-15b}$$

$$Z_i = d_0 + d(i-1) \tag{7-15c}$$

Then the velocity of the point can be calculated by differentiating equation (7-15) by time t:

$$v_{xi} = -r\omega\sin\theta \tag{7-16a}$$

$$v_{yi} = r\omega\cos\theta \tag{7-16b}$$

$$v_{zi} = 0 \tag{7-16c}$$

7.3.1.1 Impacts between Balls

Impacts between balls was determined by using the same method as introduced in Section 5.3.3.

7.3.1.2 Impacts between Balls and Wall, Impeller or Shaft

The condition for an impact to happen between a ball and the all of the container, the impellers or the shaft, the position and the velocity on the wall, the impellers or the shaft at the contact point are determined by the following considerations:

- Impact on the cylinder wall of the container

If the following equation is satisfied, an impact happens between a ball and the wall of the container.

$$\sqrt{X^2 + Y^2} + R_b \geq R_m \tag{7-17}$$

where R_m is the radius of the container of the attritor mill.

The position on the wall of the container at the contact point, (X_c, Y_c, Z_c), was determined by

$$X_c = \frac{R_m X}{\sqrt{X^2 + Y^2}} \tag{7-18a}$$

$$Y_c = \frac{R_m Y}{\sqrt{X^2 + Y^2}} \tag{7-18b}$$

$$Z_c = Z \tag{7-18c}$$

Since the container does not move, the velocity at the contact point was set to be zero.

- Impact on the shaft

If the following equation is satisfied, an impact happens between a ball and the shaft.

$$\sqrt{X^2 + Y^2} - R_b \le R_d \tag{7-19}$$

where R_d is the radius of the central axis.

The position on the shaft at the contact point, (X_c, Y_c, Z_c), was determined by

$$X_c = \frac{R_d X}{\sqrt{X^2 + Y^2}} \tag{7-20a}$$

$$Y_c = \frac{R_d Y}{\sqrt{X^2 + Y^2}} \tag{7-20b}$$

$$Z_c = Z \tag{7-20c}$$

The velocity of the shaft at the contact point, (v_{xc}, v_{yc}, v_{zc}), was determined by

$$v_{xc} = -\frac{\omega R_d Y}{\sqrt{X^2 + Y^2}} \tag{7-21a}$$

$$v_{yc} = \frac{\omega R_d X}{\sqrt{X^2 + Y^2}} \tag{7-21b}$$

$$v_{zc} = 0 \tag{7-21c}$$

- Impact on the bottom of the container

If the following equation is satisfied, an impact happens between a ball and the bottom of the container.

$$Z \le R_d \tag{7-22}$$

The position at the contact point, (X_c, Y_c, Z_c), was determined by

$$X_c = X \tag{7-23a}$$

$$Y_c = Y \tag{7-23b}$$

$$Z_c = 0 \tag{7-23c}$$

The velocity at this point was also set to be zero considering the container is stationary.

- Impact on the impellers

If the following condition is satisfied, the ball impacts on the cylindrical surface of impeller *i*.

$$\begin{cases} \min\left\{(X - r\cos\theta)^2 + (Y - r\sin\theta)^2 + [d_0 + d(i-1) - Z]^2\right\} \le (R_b + r_i)^2 \\ \sqrt{X^2 + Y^2} \le R_I \end{cases} \tag{7-24}$$

The position of the contact point, (r_c, θ_c, Z_c), was determined by:.

$$\theta_c = \tan^{-1}\left(\frac{Y}{X}\right) + \tan^{-1}\sqrt{\frac{r_i^2 - Z_c^2}{X^2 + Y^2 + [d_0 + d(i-1) - Z]^2 - \zeta^2}} \tag{7-25a}$$

$$r_c = \sqrt{X^2 + Y^2 + [d_0 + d(i-1) - z]^2 - \zeta^2 + r_i^2} \tag{7-25b}$$

$$Z_c = d_0 + d(i-1) - \frac{r_i}{\zeta}[d_0 + d(i-1) - Z] \tag{7-25c}$$

where, $\zeta = \sqrt{\min\left\{(X - r\cos\theta)^2 + (Y - r\sin\theta)^2 + [d_0 + d(i-1) - Z]^2\right\}}$

Written in position contacted to $O - XYZ$ coordinate system, we have

$$X_c = r_c \cos\theta_c \tag{7-26a}$$

$$Y_c = r_c \sin\theta_c \tag{7-26b}$$

$$Z_c = d_0 + d(i-1) - \frac{r_i}{\zeta}[d_0 + d(i-1) - Z] \tag{7-26c}$$

If the following condition is satisfied, the ball impacts on the end of impeller *i*.

$$\begin{cases} (X - R_i\cos\theta)^2 + (Y - R_i\sin\theta)^2 + [d_0 + d(i-1) - Z]^2 \le (R_b + r_i)^2 \\ \sqrt{X^2 + Y^2 + [d_0 + d(i-1) - Z]^2} > R_i \end{cases} \tag{7-27}$$

The position of the contact point, (X_c, Y_c, Z_c), was determined by

$$X_c = R_i \cos\theta + \frac{r_i}{\zeta}(X - R_i \cos\theta) \tag{7-28a}$$

$$Y_c = R_i \sin\theta + \frac{r_i}{\zeta}(Y - R_i \sin\theta) \tag{7-28b}$$

$$Z_c = d_0 + d(i-1) - \frac{r_I}{\zeta}[d_0 + d(i-1) - Z] \tag{7-28c}$$

where, $\zeta = \sqrt{(X - R_i \cos\theta)^2 + (Y - R_i \sin\theta)^2 + [d_0 + d(i-1) - Z]^2}$

Written in (r_c, θ_c, Z_c), we have

$$\theta_c = tg^{-1}\left(\frac{Y_c}{X_c}\right) \tag{7-29a}$$

$$r_c = \sqrt{X_c^{\,2} + Y_c^{\,2}} \tag{7-29b}$$

$$Z_c = d_0 + d(i-1) - \frac{r_I}{\zeta}[d_0 + d(i-1) - Z] \tag{7-29c}$$

The velocity on the impeller at the contact point is

$$v_{xc} = -r_c \omega \sin\theta_c \tag{7-30a}$$

$$v_{yc} = r_c \omega \cos\theta_c \tag{7-30b}$$

$$v_{zc} = 0 \tag{7-30c}$$

7.3.1.3 Free Movement of Balls

Free movement of balls was calculated by using the same method as described in Section 5.3.2.

7.3.1.4 The Initial Positions and Velocities of Balls

The balls were assumed to pack in the container, where the balls could not reach the shaft axis and the impellers.

The initial velocities of balls in an attritor mill were considered to be the same as those of the positions of balls rotating about the central shaft at the spinning velocity of ω.

7.4 Methodology of Computation

The methodology of computation used in simulating of planetary mill and attritor mill milling was the same as that of SPEX 8000 Mixer/Mills.

7.5 Preliminary Results on Modeling of Planetary Mill

7.5.1 One Ball in the Vial

A preliminary simulation was performed by using the global model for planetary mills combined with the local model in Chapter 4. The vial was supposed to be a cylinder and the mass of the stainless steel ball was 6.26 mm in radius. The calculated trajectories under different rotating speed of the vial are displayed in Figure 7-6.

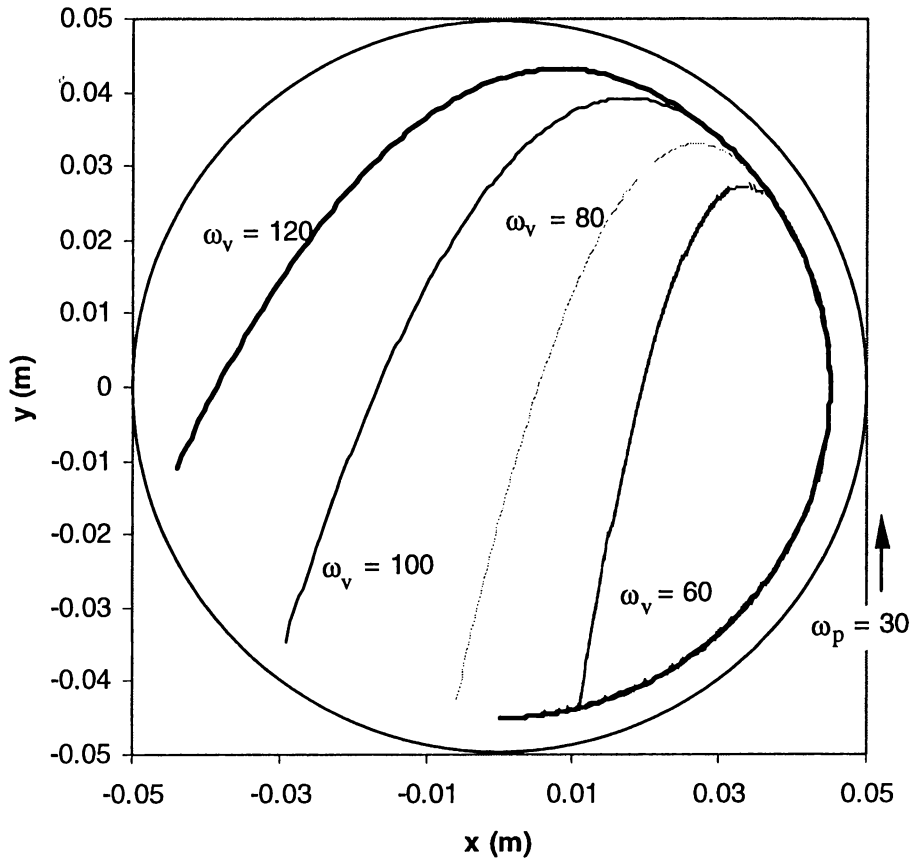

Figure 7-6. Calculated trajectory of a ball with 3.94 mm in radius corresponding to different rotation speed of the vial (rpm) for a cylindrical vial

It can be seen that the trajectory of the ball depends on the rotation speed of the vial, ω_v, when the rotation speed of the planetary arm, ω_p, is constant. There is a range of ω_v (i.e. 40 rpm $< \omega_v <$ 140 rpm), under which the ball would gain enough speed to take off from the cylindrical wall of the vial and drop down to the bottom of the cylindrical wall. If ω_v was very small, the ball would slip on the cylindrical wall of the vial, while it could not gain enough speed so as to take off from the cylindrical wall of the vial. If ω_v was very high, the ball would also slip on and run with the cylindrical wall of the vial without getting off from the cylindrical wall of the vial.

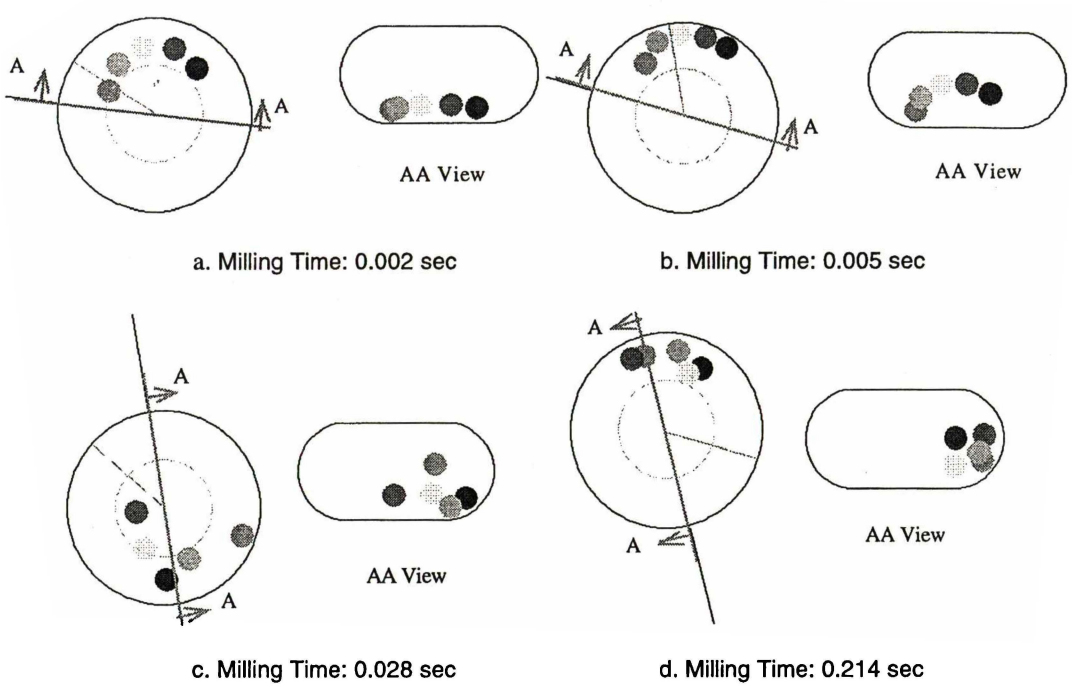

Figure 7-7. Example images showing the positions of the vial and balls at different times after milling starts for five balls in the planetary mill

7.5.2 Five Balls in the Vial

Another simulation was performed on the condition whose parameters are shown in Table 7-1. Figure 7-7 shows the positions of balls and vial at different times recorded from a simulation where 5 stainless steel balls with 4.51 mm and 5.26 mm in radii of 304 stainless steel powder were placed in the vial. A visualized demonstration program, developed by the author, in this condition is available from "http://www.geocities.com/www67/MA-Demo.zip"

Table 7-1. Parameters for the planetary mill

ω_p	300 rpm
ω_v	600 rpm
R_v	50 mm
R_p	100 mm
R	25 mm

7.6 Preliminary Results on Modeling of Attritor Mill

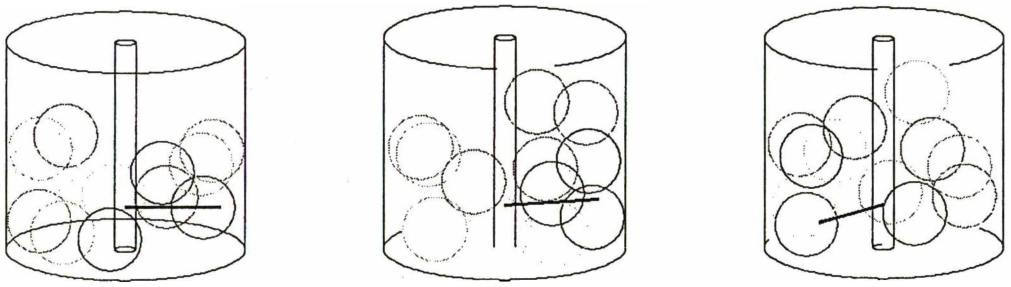

a. Milling Time: 0.000 sec b. Milling Time: 0.310 sec c. Milling Time: 0.336 sec

Figure 7-8. Example images showing the positions of the impeller and balls at different times after milling starts for twelve balls in the Attritor mill

A preliminary simulation has been performed on the attritor mill, where there was only one impeller in the container and where the container was 46 mm in diameter and 40 mm in length. The impeller was assumed to rotate at a velocity of 100 rpm. Figure 7-8 shows the positions of balls and the impeller at different times recorded from a simulation where 12 stainless steel balls with 6.26 in radii were placed in the container. A visualized demonstration program, developed by the author, in this condition is available from "http://www.geocities.com/www67/MA-Demo.zip".

7.7 Summary

3 dimensional global models for planetary mills and attritor mills have been deduced. Preliminary simulations have been done with these models coupled with the local model described in Chapter 4. More simulation is needed to understand the dynamics of the milling process.

Chapter Eight

Conclusions and Recommendations

8.1 Conclusions

- A 3-dimensional model has been developed to simulate the head-on impact process between two balls or between a ball and the vial wall with powder in between. The comparison between an experimental result in the literature and the simulation by using this model shows that this model can simulate the head-on impact process, which involves powder.

- Application of the head-on impact model in high-energy ball milling shows that the ball-ball and ball-wall impacts do have some difference. It was also observed that the ball size, impact velocity and powder thickness all affect the impact pressure, and that the deformation of the balls is substantial compared to the powder thickness involved in an impact.

- 3-dimensional models have also been developed to simulate the movement of balls considering the effects of spinning and oblique impact of balls and multi-ball impacts when there is powder between them.

- A model was also developed to estimate the volume of the powder involved in an impact. The prediction of the weight of powder involved in each impact made based on this model was in good agreement with the observation reported.

- A 3-dimensional global model has been developed for SPEX-8000 Mixer/Mills based on the mechanics of the machine.

- The simulation results of the vial motion show that the vibration of the vial is substantial in any of the 3 directions, the vibratory motion of fulcrums is needed to consider and the condition of the springs, which balance the vial and the fulcrums, affects the vial motion.

- The global model was coupled with the models for the impacts in order to predict the dynamics of milling process.

- The simulation results revealed that the movement of balls after milling starts can be separated into two stages. The first stage is the unstable stage, which lasts for less than 0.3 second and involves mostly rolling and slipping of balls on the vial wall. The second stage is the stable stage, when the impact frequency, the mean impact velocity and mean spinning velocity of balls do not change significantly over time.

- The impacts happened in ball milling on a SPEX 8000 Mixer/Mill have very high frequency and the majority of these impacts happen at low velocities of less than 4 m/s. For different number of balls, the simulation results indicate that the frequency of impacts between balls and the vial wall is proportional to the number of balls and the number of impacts between balls is nearly proportional to the square of the number of balls and the square of radius of balls.

- For given number of balls, the prediction shows the majority of the impacts occur at angles in the range of 15~75°.

- Simulation shows that multi-ball impacts occupy a substantial fraction among the impacts.

- A reasonable model has been developed for the first time to calculate the time needed for ball milling given the effective impact frequency and the fraction of powder effectively mechanically milled are known.

- The milling time is a function of the number and the size of balls. For a given radius of balls, there is an optimum number for the best milling efficiency.

- Global models for planetary mills and attritor mills have been developed. Preliminary simulations have been performed.

8.2 Recommendations for Future Work

- Investigate the milling dynamics under the condition of different shape of vial so that the shape can be optimized for SPEX 8000 Mixer/Mills.

- Quantify the critical impact velocity using experimental methods so that the size and the number of balls can be optimized for best milling efficiency by calculating the milling time required to achieve a particular microstructure.

- Investigate the cold welding and fracture events and develop corresponding models so that the prediction of particle size and the thickness of multi-layer could be possible by combining it with current models.

- Relate the simulation result to the theory of phase formation and thus the prediction of different phase formation could be possible.

- Apply the models for planetary mill and attritor mill in different conditions.

Appendix I

Equation (3-21)

Supposing the two balls, whose radii are R_1 and R_2, compress together with a thickness of powder compact in between (Figure AI-1). The minimum distance between the two balls is h. If a point M_1 on the surface of ball 1 is r distant way from the axistyle O_1O_2, a corresponding point on that of the other ball is M_2. Then we have $(R_1 - z_1)^2 + r^2 = R_1^2$ and $(R_2 - z_2)^2 + r^2 = R_2^2$. From the these equations, we have $z_1 = \dfrac{r^2}{2R_1 - z_1}$ and $z_2 = \dfrac{r^2}{2R_2 - z_2}$. In ball milling, powder thickness involved in an impact is very small, thus it is reasonable to assume $z_1 << 2R_1$ and $z_2 << 2R_2$. Then we have $z_1 = r^2/(2R_1)$ and $z_2 = r^2/(2R_2)$.

The distance between M_1 and M_2 is $\left(\dfrac{r^2}{2R_1} + \dfrac{r^2}{2R_2} + h\right)$.

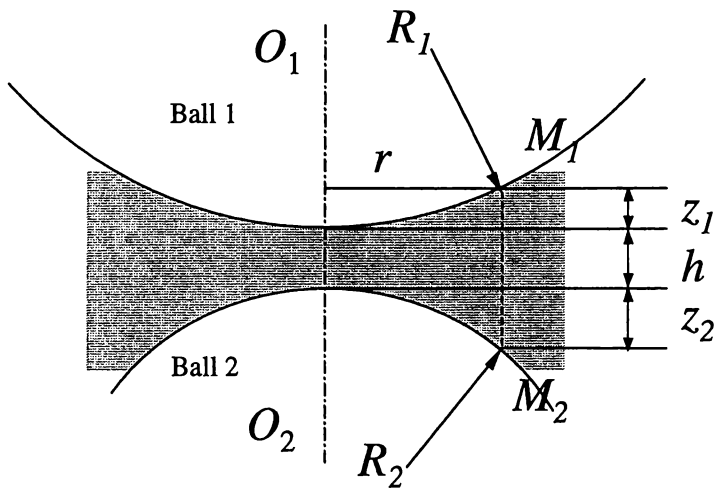

Figure AI-1. Two different size balls compressed together with a thickness of powder in between

Assuming R_e is the effective radius, then the distance between M_1 and M_2 is $\left(\frac{r^2}{R_e}+h\right)$. Then we have the following relation:

$$\frac{r^2}{2R_1}+\frac{r^2}{2R_2}+h=\frac{r^2}{R_e}+h$$

Then we have

$$\frac{2}{R_e}=\frac{1}{R_1}+\frac{1}{R_2}$$

This is the same as equation (3-21).

Appendix II

Equation (4-16)

In Figure 4-6, the shape of powder pile coated on the surface of a ball was assumed to be a cone sitting on the surface of the ball.

If the cone is sitting on a plane surface, its bottom radius is $R\sin\psi_{pb}$ and its height is $R\tan\theta_p$, then its volume is $\frac{1}{3}\pi R^3 \sin^3\psi_{pb}\tan\theta_p$.

If the cone is sitting on the surface of the ball, its volume is the above volume deducted by the volume of the spherical sector, whose radius is R and height is $R(1-\cos\psi_{pb})$. The volume of this spherical sector is $\frac{1}{3}\pi R^3(1-\cos\psi_{pb})^2(2+\cos\psi_{pb})$ [1].

As the volume of the powder is equal to the difference between the two volumes, we have

$$V_{\max} = \frac{1}{3}\pi R^3\left[\sin^3\psi_{pb}\tan\theta_p - (1-\cos\psi_{pb})^2(2+\cos\psi_{pb})\right]$$

This is the maximum volume of powder and it is the same as equation (4-16).

Reference:

[1] Tuma, Jan J. and Walsh, Ronald A., *Engineering Mathematics Handbook, Fourth Edition*, McGraw-Hill, New York, 1997, 34

Appendix III

Geometrical Analysis on Impact Angle Probability

It is assumed that balls can be anywhere in the vial. If ball A is in the central area of the vial as shown in Figure A3-1, the center of ball C must run in the shadow area when it impacts with ball A. The radius of the shadow area is twice of the ball radius. If the impact angle is ψ, the center of ball C must be in the line of thick circle, which has a radius of $2r_b \sin\psi$. The probability for an impact happening at angle between 0 to ψ is the ratio between the area of the thick circle and the area of the shadow circle. When ball A at a such a position that it is able to impact ball C at angle ψ from all different directions (That is, $R_v - r - r_b > 2r_b$, or $\psi < arcsin\frac{R_v - r - r_b}{2r_b}$ when $R_v - r - r_b \le 2r_b$, where R_v is the radius of the vial, r is the distance from the center of ball A to the center the vial and r_b is the radius of balls), the probability for an impact happening at angle in the range of ψ to $\psi + d\psi$ is:

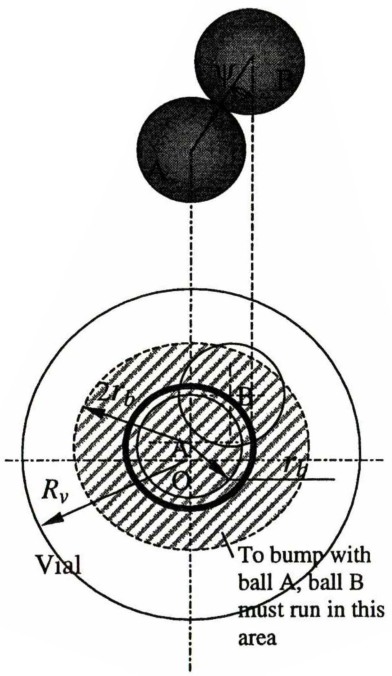

Figure A3-1. Schematic diagram showing the probable positions of balls during impact

$$p(\psi)=\xi\frac{2\pi\cdot 2r_b\sin\psi}{\pi(2r_b)^2}\cdot 2r_b\cos\psi d\psi=\xi\sin(2\psi)d\psi \qquad \text{(A3-1)}$$

where ξ is used to adjust the probability so that the total value is 1.

Based on similar consideration, if $R_v-r-r_b\le 2r_b$ when $\psi\ge arcsin\frac{R_v-r-r_b}{2r_b}$, the probability for an impact to occur at an angle in the range of ψ to $\psi+d\psi$ is:

$$p(\psi)=\xi\frac{4\alpha a_b\sin\psi}{4\alpha r_b^{\,2}+\beta(R_v-r_b)^2}\cdot 2r_b\cos\psi d\psi=\xi\frac{4\alpha a_b^{\,2}\sin 2\psi}{4\alpha r_b^{\,2}+\beta(R_v-r_b)^2}d\psi \qquad \text{(A3-2)}$$

where, $\cos\alpha=\frac{(2r_b\sin\psi)^2+r^2-(R_v-r_b)^2}{4rr_b\sin\psi}$, $\cos\beta=\frac{r^2+(R_v-r_b)^2-(2r_b\sin\psi)^2}{2r(R_v-r_b)}$ and

Thus the probability for an impact to occur at an angle between ψ_1 and ψ_2 is

$$p(\psi_1\sim\psi_2)=\xi\int_{\psi_1}^{\psi_2}p(\psi)d\psi \qquad \text{(A3-3)}$$

Since balls can be anywhere in the vial, the above equation need to be modified in the following:

$$P(\psi_1\sim\psi_2)=\xi 2\pi\int_0^{R_v-r_b}\int_{\psi_1}^{\psi_2}p(\psi)d\psi dr \qquad \text{(A3-4)}$$

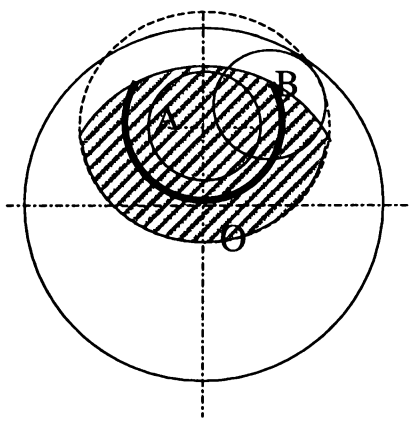

Figure A3-2. The probable positions of balls A and B during impact when one ball is too close to the cylindrical wall

Appendix IV

Experimental Results of the Impact Number and Velocity Distribution

In this appendix, the number of impacts at different velocities and different angles are listed for different number of balls and different sizes of stainless steel balls. The effective impacts are listed by using the bold fonts. The unit used for the angle is degree (°) and the unit for the impact velocity is m/s.

8 gram balls

Ball-ball impact

Angle	5	15	25	35	45	55	65	75	85	Total
1										
2	3	5	23	11	19	11	11	18	16	117
3	3	17	27	31	39	38	46	30	31	262
4	27	38	47	78	74	57	59	51	37	468
5	29	59	81	112	101	112	73	69	69	705
6	39	87	153	195	131	112	107	94	92	1010
7	65	167	251	235	168	153	144	123	115	1421
8	68	203	281	280	225	180	143	135	151	1666
9	121	310	425	357	273	253	201	159	210	2309
10	215	479	522	388	301	265	295	221	194	2880
11	243	657	636	472	360	289	329	279	230	3495
12	258	671	820	584	423	348	286	314	327	4031

Velocity	0-1	1-2	2-3	3-4		4-5	5-6	6-7	7-8	8-9	9-10	10-11
1												
2	15	18	21	5	**21**	**9**	**16**	**11**	**1**			
3	17	37	61	12	**47**	**40**	**33**	**9**	**5**	**1**		
4	34	110	127	19	**78**	**55**	**25**	**15**	**5**			
5	56	187	184	34	**137**	**77**	**20**	**7**	**3**			
6	99	280	317	39	**158**	**80**	**21**	**12**	**4**			
7	196	405	453	46	**185**	**98**	**31**	**5**	**2**			
8	208	544	505	58	**233**	**82**	**26**	**9**	**1**			
9	320	815	755	63	**250**	**79**	**21**	**3**	**3**			
10	501	1105	846	61	**245**	**105**	**15**	**2**				
11	620	1557	895	68	**273**	**73**	**9**					
12	597	1734	1263	71	**285**	**69**	**10**	**2**				

Ball-wall impact

Angle	5	15	25	35	45	55	65	75	85	Total
1	3	13	35	57	19	11	8	6	15	167
2	16	29	69	78	59	39	27	38	28	383
3	8	49	127	129	79	55	73	62	56	638
4	41	125	154	171	83	73	74	73	56	850
5	48	213	200	160	165	99	93	91	81	1150
6	68	280	303	216	161	125	127	105	81	1466
7	138	323	448	264	193	151	141	111	125	1894
8	152	473	453	260	247	138	142	133	157	2155
9	245	649	581	365	243	177	156	143	142	2701
10	311	743	649	389	321	216	233	147	121	3130
11	438	953	787	411	308	214	214	197	163	3685
12	487	1126	853	533	352	267	222	191	237	4268

Velocity	0-1	1-2	2-3	3-4	4-5	5-6		6-7	7-8	8-9	9-10	10-11
1	0	20	73	39	25	1	**6**	**3**				
2	6	103	139	85	35	1	**10**	**4**				
3	31	174	227	125	63	2	**14**	**3**				
4	60	292	287	140	44	3	**24**					
5	88	440	397	158	52	2	**14**					
6	145	666	429	165	52	1	**8**					
7	282	879	508	186	36		**3**					
8	289	1048	628	156	33		**1**					
9	468	1389	681	148	15							
10	618	1717	665	114	14		**2**					
11	882	2027	692	80	4							
12	832	2407	907	115	7							

7 gram balls

Ball-ball impact

Angle	5	15	25	35	45	55	65	75	85	Total
1										
2		10	15	13	16	11	21	9	8	103
3	3	12	29	25	41	17	37	41	18	223
4	11	43	66	47	85	43	38	55	50	438
5	14	81	88	92	115	81	73	75	63	682
6	26	110	143	112	129	109	83	113	75	900
7	41	154	204	205	193	147	149	115	121	1329
8	79	198	293	242	252	197	151	181	153	1746
9	75	241	337	375	273	207	190	217	193	2108
10	144	383	457	375	327	300	252	180	210	2628
11	175	506	590	480	381	303	277	271	245	3228
12	266	619	662	533	453	360	373	315	375	3956
13	385	913	898	760	503	434	394	335	405	5027
14	510	1193	1202	908	695	517	400	436	374	6236

Velocity	0-1	1-2	2-3	3-4		4-5	5-6	6-7	7-8	8-9	9-10	10-11	11
1													
2	4	17	15	14	**11**	**25**	**14**	**1**	**2**				
3	0	35	54	34	**27**	**41**	**25**	**4**	**3**				
4	28	102	115	47	**39**	**64**	**27**	**13**	**3**				
5	51	160	187	79	**65**	**88**	**27**	**18**	**6**	**1**			
6	102	251	216	101	**82**	**87**	**38**	**16**	**5**	**2**			
7	138	389	420	129	**106**	**100**	**38**	**7**	**2**				
8	176	570	523	171	**140**	**127**	**32**	**7**	**1**				
9	250	645	681	179	**146**	**141**	**47**	**14**	**5**				
10	376	885	833	213	**175**	**109**	**29**	**6**	**2**				
11	493	1181	993	221	**181**	**121**	**33**	**5**					
12	592	1450	1229	294	**241**	**118**	**27**	**5**					
13	1018	2081	1327	256	**209**	**117**	**17**	**2**					
14	1268	2806	1628	230	**189**	**97**	**14**	**2**					

Ball-wall impact

Angle	5	15	25	35	45	55	65	75	85	Total
1	3	25	23	41	31	17	12	16	21	189
2	5	35	87	65	61	41	43	30	24	391
3	9	57	117	119	73	66	60	54	43	598
4	30	105	158	154	133	101	69	57	49	856
5	37	193	236	197	134	133	67	67	75	1139
6	47	229	301	233	138	139	100	108	98	1393
7	79	339	342	241	194	139	141	107	129	1711
8	106	401	462	295	211	191	123	144	126	2059
9	155	511	541	357	236	237	192	153	165	2547
10	249	597	642	403	289	221	181	169	150	2901
11	258	773	699	449	308	295	184	160	166	3292
12	328	968	902	517	374	289	226	197	148	3949
13	566	1322	918	590	453	337	242	207	221	4856
14	780	1590	1061	695	421	353	306	259	238	5703

Velocity	0-1	1-2	2-3	3-4	4-5	5-6		6-7	7-8	8-9	9-10	10-11
1		40	68	43	29	4	**5**					
2	10	86	129	98	45	9	**11**	**3**				
3	33	149	227	127	39	9	**11**	**3**				
4	58	293	281	157	45	8	**9**	**5**				
5	85	427	369	174	73	5	**6**					
6	106	529	507	164	67	8	**9**	**3**				
7	192	747	535	180	49	2	**3**	**3**				
8	203	973	657	186	38	1	**1**					
9	384	1145	761	209	47		**1**					
10	450	1438	778	209	23	1	**2**					
11	494	1689	914	176	15	2	**2**					
12	747	1993	1000	193	16							
13	1093	2719	853	179	6	2	**3**	**1**				
14	1543	3124	923	103	6	2	**2**					

6 gram balls

Ball-ball impact

Angle	5	15	25	35	45	55	65	75	85	Total
1										
2	1	11	11	15	17	7	7	20	8	97
3	5	21	21	35	39	28	26	32	19	226
4	12	33	54	66	69	73	61	43	43	454
5	11	79	90	115	90	81	75	53	83	677
6	25	95	131	130	131	112	110	98	73	905
7	47	122	173	198	171	141	165	135	118	1270
8	66	153	264	212	233	177	163	163	143	1574
9	67	213	315	286	275	212	221	187	193	1969
10	117	348	435	413	259	239	225	214	232	2482
11	157	469	543	476	373	308	312	296	287	3221
12	219	456	657	572	443	338	309	328	297	3619
13	337	721	968	737	539	493	349	363	359	4866
14	415	977	1227	867	657	543	432	401	395	5914
15	528	1309	1363	1063	822	607	551	618	487	7348

Velocity	0-1	1-2	2-3	3-4	4-5	5-6	6-7	7-8	8-9	9-10	10-11
1											
2	7	16	33	12	**1**	**15**	**6**	**7**			
3	14	33	63	45	**4**	**33**	**18**	**15**	**1**		
4	14	101	123	93	**8**	**59**	**37**	**11**	**7**	**1**	
5	35	177	183	143	**12**	**66**	**27**	**29**	**3**	**2**	
6	77	221	257	154	**13**	**124**	**27**	**21**	**7**	**4**	**1**
7	99	335	385	248	**22**	**103**	**62**	**5**	**6**	**3**	**2**
8	151	441	455	275	**24**	**150**	**52**	**19**	**4**	**3**	
9	188	647	581	297	**26**	**157**	**55**	**9**	**9**		
10	284	846	720	379	**33**	**157**	**37**	**15**	**11**		
11	531	1134	957	335	**29**	**173**	**48**	**12**	**2**		
12	496	1260	1118	458	**40**	**194**	**41**	**10**	**2**		
13	868	1817	1390	535	**46**	**159**	**45**	**3**	**3**		
14	1217	2503	1635	423	**26**	**91**	**16**	**3**			
15	1359	3123	2043	495	**43**	**151**	**30**	**13**	**1**		

Ball-wall impact

Angle	5	15	25	35	45	55	65	75	85	Total
1	7	19	27	25	27	17	28	12	13	175
2	16	29	61	60	57	55	37	28	24	367
3	8	63	103	119	87	63	47	54	62	606
4	31	96	169	141	103	84	85	72	55	836
5	39	142	200	181	129	115	99	89	57	1051
6	75	216	275	209	153	139	99	114	97	1377
7	84	237	327	241	205	155	117	115	152	1633
8	123	354	415	287	205	175	152	134	141	1986
9	143	415	545	335	224	193	161	157	182	2355
10	201	589	517	366	242	218	180	160	195	2668
11	268	692	713	433	359	269	229	159	180	3302
12	279	822	857	491	301	295	240	229	217	3731
13	454	1092	903	559	379	281	259	262	243	4432
14	652	1235	1090	657	430	319	281	343	271	5278
15	775	1646	1163	760	481	398	318	393	331	6265

Velocity	0-1	1-2	2-3	3-4	4-5	5-6	6-7		7-8	8-9	9-10	10-11
1	1	51	60	22	27	11	1	2				
2	20	77	127	81	43	13	1	5				
3	25	171	203	128	59	17	1	2				
4	63	256	280	155	52	30						
5	92	348	318	198	75	18		2				
6	128	528	455	192	54	19		1				
7	146	666	503	237	60	21						
8	201	881	617	222	57	8						
9	293	1087	670	220	79	3	1	2				
10	383	1248	755	233	43	6						
11	597	1629	825	215	28	7		1				
12	634	1777	1014	262	39	5						
13	930	2289	958	220	31	2		2				
14	1213	2825	1011	208	20			1				
15	1568	3338	1144	192	17	3	1	2				

5 gram balls

Ball-ball impact

Angle	5	15	25	35	45	55	65	75	85	Total
1										
2	1	5	5	15	15	17	13	8	12	91
3	5	17	25	47	40	34	24	21	17	230
4	4	45	53	73	82	37	56	47	49	446
5	10	51	104	51	83	83	63	64	75	584
6	23	75	115	137	151	114	93	104	63	875
7	35	150	153	177	203	151	122	113	127	1231
8	63	159	199	233	154	182	161	163	136	1450
9	70	199	320	311	301	207	197	187	165	1957
10	115	312	344	384	284	274	221	253	232	2419
11	109	349	437	411	357	317	284	267	264	2795
12	165	457	611	554	383	283	312	309	253	3327
13	259	627	673	655	480	385	349	341	305	4074
14	253	697	793	771	614	463	451	359	333	4734
15	334	909	1023	785	664	474	413	394	345	5341

Velocity	0-1	1-2	2-3	3-4	4-5		5-6	6-7	7-8	8-9	9-10	10-11
1												
2	8	11	22	15	7	**11**	**5**	**8**	**3**	**1**		
3	8	29	85	49	10	**16**	**17**	**11**	**3**	**2**		
4	21	101	109	97	28	**43**	**31**	**7**	**4**	**5**		
5	37	116	137	130	34	**52**	**46**	**18**	**10**	**4**		
6	59	218	247	169	42	**63**	**45**	**16**	**11**	**5**		
7	76	312	337	258	56	**83**	**75**	**22**	**9**	**3**		
8	143	415	373	283	56	**85**	**63**	**19**	**9**	**4**		
9	214	557	577	343	66	**100**	**70**	**25**	**5**			
10	250	752	702	446	72	**107**	**67**	**20**	**3**			
11	328	845	858	431	84	**125**	**93**	**27**	**4**			
12	437	1155	986	474	87	**130**	**44**	**14**				
13	718	1469	1083	507	85	**127**	**73**	**11**	**1**			
14	704	1721	1365	641	87	**130**	**71**	**12**	**3**			
15	841	2151	1540	540	84	**127**	**47**	**7**	**4**			

Ball-wall impact

Angle	5	15	25	35	45	55	65	75	85	Total
1	9	27	33	27	23	21	18	18	11	187
2	6	25	77	68	61	41	27	36	38	379
3	19	59	87	97	75	57	54	54	43	545
4	26	78	139	139	117	95	69	51	71	785
5	32	121	197	205	131	119	89	99	84	1077
6	42	195	248	184	172	117	135	90	83	1266
7	67	265	307	253	131	145	114	152	142	1576
8	90	297	407	301	215	153	156	114	150	1883
9	145	374	483	307	273	190	187	153	137	2249
10	169	493	517	347	228	226	213	199	201	2593
11	210	565	566	424	286	241	221	206	189	2908
12	251	740	709	404	285	272	243	198	216	3318
13	349	787	797	489	343	307	233	240	198	3743
14	395	1027	810	575	423	305	283	279	264	4361
15	446	1189	911	623	387	376	272	287	267	4758

Velocity	0-1	1-2	2-3	3-4	4-5	5-6	6-7		7-8	8-9	9-10	10-11
1	1	45	76	34	17	11	2	1				
2	12	88	113	103	39	17	4	2	2			
3	14	119	192	137	59	21			3			
4	29	212	267	182	72	17	4	2				
5	63	377	337	209	61	21	6	3				
6	72	429	450	212	79	20	3	1				
7	109	606	493	270	75	21	1	1				
8	198	733	605	239	83	23	1	1				
9	313	917	676	247	77	19						
10	314	1117	797	271	78	16						
11	354	1282	887	316	49	17	1	1	1			
12	557	1513	906	275	57	9	1					
13	576	1943	937	217	60	10						
14	742	2170	1116	265	55	11	1	1				
15	979	2472	1017	237	40	11	1	1				

4 gram balls

Ball-ball impact

Angle	5	15	25	35	45	55	65	75	85	Total
1										
2		9	19	13	13	9	9	12	10	94
3	3	23	15	37	43	34	20	22	25	222
4	5	26	33	45	39	48	47	44	51	338
5	14	66	49	97	77	77	57	61	57	555
6	23	66	105	156	140	80	89	95	80	834
7	45	94	169	171	135	149	108	111	105	1087
8	30	123	231	237	187	165	124	158	122	1377
9	71	184	251	303	221	176	193	127	149	1675
10	86	276	342	352	281	289	190	197	167	2180
11	122	302	379	385	302	281	241	226	225	2463
12	120	361	597	480	783	353	266	286	269	3515
13	167	462	595	565	483	351	337	263	320	3543
14	199	621	671	599	475	430	354	346	409	4104
15	216	673	752	665	511	415	404	392	351	4379

Velocity	0-1	1-2	2-3	3-4	4-5	5-6		6-7	7-8	8-9	9-10	10-11
1												
2	6	20	19	10	13	1	**7**	**10**	**7**		**1**	
3	9	57	39	46	43	1	**12**	**7**	**7**	**1**		
4	18	55	74	76	65	5	**47**	**14**	**1**	**3**		
5	31	115	129	113	79	6	**53**	**18**	**6**	**5**		
6	47	194	221	185	103	6	**51**	**18**	**5**	**3**	**1**	
7	74	260	289	242	129	6	**55**	**16**	**8**	**5**	**3**	
8	84	324	373	307	169	7	**66**	**33**	**8**	**5**	**1**	
9	176	468	461	289	165	8	**75**	**16**	**9**	**6**	**2**	
10	225	608	629	394	179	10	**86**	**33**	**10**	**4**	**3**	
11	258	767	727	407	197	7	**63**	**22**	**9**	**3**	**3**	
12	526	967	1009	579	317	9	**77**	**24**	**5**	**2**		
13	376	1156	1039	579	295	7	**60**	**21**	**9**	**1**		
14	556	1364	1179	639	263	8	**74**	**15**	**4**	**1**	**1**	
15	649	1526	1218	627	253	8	**69**	**21**	**6**	**2**		

Ball-wall impact

Angle	5	15	25	35	45	55	65	75	85	Total
1	5	15	27	39	23	15	18	8	15	165
2	8	25	55	64	67	39	39	30	22	349
3	4	47	109	89	77	53	65	64	46	554
4	11	82	124	147	109	91	67	83	67	781
5	42	141	208	161	127	91	95	84	93	1042
6	49	149	225	205	153	114	133	94	121	1243
7	53	187	251	253	211	127	138	122	134	1476
8	79	245	321	294	198	133	179	148	145	1742
9	95	292	435	333	195	193	161	159	133	1996
10	107	377	502	404	251	219	199	160	174	2393
11	137	509	510	407	262	248	205	192	208	2678
12	172	511	604	415	274	262	224	238	223	2923
13	213	649	737	493	290	242	253	278	244	3399
14	256	783	737	571	355	305	237	287	241	3772
15	304	834	793	547	462	399	289	253	247	4128

Velocity	0-1	1-2	2-3	3-4	4-5	5-6	6-7	7-8	8-9	9-10	10-11
1	2	14	59	51	28	5	6				
2	6	77	109	85	53	19					
3	28	118	185	139	59	21	4				
4	26	235	231	171	85	27	5	1			
5	90	328	309	218	60	32	5				
6	75	399	412	224	81	46	6				
7	84	519	512	239	90	25	7				
8	122	650	583	263	97	27					
9	179	791	623	281	86	27	9				
10	255	1019	697	293	93	28	8				
11	357	1073	820	319	88	19	2				
12	399	1271	837	295	103	18					
13	428	1603	909	373	75	11					
14	536	1763	1051	295	113	12	2				
15	650	2007	1077	316	61	15	2				

3 gram balls

Ball-ball impact

Angle	5	15	25	35	45	55	65	75	85	Total
1										
2		7	9	17	9	3	1	16	6	68
3	3	4	21	23	23	35	13	23	24	169
4	3	17	62	47	79	35	36	33	36	348
5	5	45	70	63	76	71	81	47	59	517
6	19	41	87	98	91	100	90	74	79	679
7	28	85	135	111	131	127	113	107	98	935
8	20	83	143	177	167	158	158	171	133	1210
9	56	183	206	241	213	171	169	147	141	1527
10	64	222	306	292	286	237	237	188	169	2001
11	64	262	334	339	297	288	279	239	194	2296
12	102	311	416	451	408	243	292	236	252	2711
13	141	394	485	441	391	343	321	325	270	3111
14	162	419	601	551	503	397	381	387	297	3698
15	206	568	653	614	483	469	385	340	340	4058

Velocity	0-1	1-2	2-3	3-4	4-5	5-6		6-7	7-8	8-9	9-10	10-11
1												
2	7	13	15	17	7	4		5				
3	1	21	42	43	33	15	2	9	3			
4	16	59	115	65	39	24	3	13	11	3		
5	27	125	101	107	78	42	5	27	3	2		
6	21	138	167	146	110	51	6	29	8	3		
7	60	207	244	191	117	74	8	19	6	8	1	
8	66	219	331	261	193	87	10	29	6	8		
9	91	387	455	287	175	63	7	36	19	7		
10	191	507	578	365	207	86	10	34	15	6	3	
11	194	585	730	459	204	62	7	34	10	8	3	
12	249	726	757	561	247	106	12	34	5	11	1	2
13	343	881	873	595	257	96	11	41	9	5		
14	429	1091	1063	615	298	129	14	41	13	5		
15	548	1285	1110	665	293	90	10	40	14	3		

Ball-wall impact

Angle	5	15	25	35	45	55	65	75	85	Total
1	5	5	29	29	23	13	10	14	19	147
2	18	31	71	48	45	29	29	28	30	329
3	11	41	95	85	73	70	66	38	51	530
4	6	79	142	126	91	103	71	71	57	746
5	21	106	162	165	143	103	103	85	79	967
6	39	132	197	199	145	125	99	114	95	1145
7	52	159	274	255	209	117	155	116	101	1438
8	50	198	331	277	199	177	189	152	134	1707
9	59	252	365	263	191	198	155	187	169	1839
10	89	319	403	352	264	243	191	155	170	2186
11	119	365	423	354	271	212	210	179	190	2323
12	129	448	555	459	334	221	255	206	220	2827
13	127	551	565	455	352	242	245	270	244	3051
14	165	559	705	521	378	354	278	255	223	3438
15	211	696	690	533	391	338	269	255	279	3662

Velocity	0-1	1-2	2-3	3-4	4-5	5-6	6-7	7-8	8-9	9-10	10-11
1	1	12	37	53	32	9	3				
2	10	60	95	96	43	12	13				
3	13	105	149	127	91	32	13				
4	18	180	248	169	86	30	15				
5	34	246	322	208	111	30	16				
6	63	335	349	247	101	44	5	1			
7	110	427	478	271	103	40	9				
8	107	577	579	277	117	43	6	1			
9	162	647	563	298	127	35	7				
10	243	785	663	349	108	34	4				
11	204	851	751	347	122	41	7				
12	302	1151	809	399	117	46	3				
13	400	1253	874	363	123	35	3				
14	425	1481	987	407	92	40	6				
15	522	1562	1030	389	123	29	7				

2 gram balls

Ball-ball impact

Angle	5	15	25	35	45	55	65	75	85	Total
1										
2	1	7	5	7	7	11	11	6	2	57
3	1	5	15	19	17	18	12	10	29	126
4	8	15	23	37	42	39	26	31	35	256
5	13	34	55	77	79	43	44	65	57	467
6	17	47	79	53	86	95	92	73	65	607
7	9	59	135	131	135	108	106	98	103	884
8	25	71	174	174	163	153	138	129	102	1129
9	45	131	180	183	185	183	175	147	143	1372
10	36	125	247	258	231	235	181	168	158	1639
11	49	168	285	295	300	233	204	207	185	1926
12	86	247	357	320	346	279	238	238	227	2338
13	73	237	374	363	393	365	339	285	219	2648
14	113	339	455	503	413	358	335	301	343	3160
15	141	345	491	536	450	401	341	344	297	3346

Velocity	0-1	1-2	2-3	3-4	4-5	5-6	6-7	7-8		8-9	9-10	10-11
1												
2	8	8	15	10	11	4		4	3			
3	2	15	15	37	22	19	11	4	3	1	2	
4	9	34	73	51	39	19	17	1		2	1	
5	30	67	102	111	68	34	24	4	2	12		
6	34	101	133	134	104	45	32	3	2	8		
7	36	157	223	220	103	88	29	5	3	7	2	
8	73	211	298	253	151	91	25	5	3	9	3	
9	86	296	346	292	192	77	47	5	4	11		
10	76	343	456	358	232	89	50	6	4	10		
11	155	379	493	382	305	125	53	5	4	13	2	
12	205	601	603	449	275	110	49	3	2	9	3	1
13	214	637	671	553	297	155	87	5	4	14	2	1
14	300	873	864	539	349	138	60	2	2	10		
15	310	892	937	611	312	189	69	4	2	9		

Ball-wall impact

Angle	5	15	25	35	45	55	65	75	85	Total
1	3	17	19	39	31	15	16	12	13	165
2	14	21	51	70	49	45	35	34	24	343
3	20	37	65	79	73	51	57	50	50	482
4	18	76	101	125	103	91	77	71	67	729
5	29	101	127	143	141	121	101	100	80	943
6	35	136	186	184	155	95	106	87	97	1081
7	31	131	239	217	158	161	111	131	98	1277
8	49	185	229	271	178	174	128	137	129	1480
9	43	199	299	289	279	177	166	170	157	1779
10	68	243	363	321	246	214	176	181	199	2011
11	83	306	402	427	298	210	216	169	174	2285
12	65	316	462	360	328	279	273	182	207	2472
13	117	392	530	433	307	281	267	215	196	2738
14	85	461	649	446	368	270	247	263	263	3052
15	170	509	606	469	393	351	293	262	210	3263

Velocity	0-1	1-2	2-3	3-4	4-5	5-6	6-7	7-8	8-9	9-10	10-11
1	1	13	49	57	28	14	3				
2	13	49	99	95	53	23	8	3			
3	11	99	124	127	75	41	5				
4	21	184	206	171	92	40	13	2			
5	31	266	295	191	115	31	13	1			
6	52	260	321	268	109	55	13	3			
7	48	339	398	288	141	40	23				
8	87	373	512	309	136	37	25	1			
9	96	574	527	367	141	63	9	2			
10	135	602	691	359	145	67	7	5			
11	200	752	721	400	141	58	11	2			
12	250	806	768	403	157	63	19	6			
13	202	944	908	440	159	57	25	3			
14	276	1150	963	433	149	60	19	2			
15	377	1296	899	433	182	50	23	3			

Appendix V

The Model for Milling Time

Ball milling is a statistical process in nature, and all powder particles have the same opportunity to be subjected to an impact during this process. After milling for some time, some of the powder might have subjected many impacts while some might have never been touched. Based on this consideration, a model has been deduced in the following to calculate the time needed to determine how much of the powder has been impacted.

If assuming that x fraction of the powder is involved in every impact, there would be $(1-x)^i$ of powder experiences the impacts after i^{th} impact. Then the number of impacts needed for y fraction of the powder to experience impacts is:

$$n = \frac{\ln y}{\ln(1-x)} \qquad \text{(A5-1)}$$

From this point of view, MA is a very "inefficient process", where there is always some powder left un-impacted no matter how long it has been milled.

In practice, every impact happens at different velocity. The powder fraction involved in every impact is different, so is the amount of powder, which is mechanically milled. If in a time unit, there is n impacts at different velocities: v_1, v_2, ..., v_n, and the amount (in percentage) of powder mechanically milled at different velocities are: x_1, x_2, ..., x_n, then the fraction of powder mechanically milled in a time unit is:

$$X = 1 - \prod_{i=1}^{n}(1 - x_i) \tag{A5-2}$$

If a time unit is viewed as a 'big impact', which generates X amount of powder mechanically milled, the total milling time needed for y fraction of powder to be mechanically milled can be calculated by

$$t = \frac{\ln y}{\ln(1 - X)} \tag{A5-3}$$